University of Stavanger

ARTEM KORNIIENKO
SUPERVISORS: NESTOR CARDOZO, LOTHAR SCHULTE, GEOFF MINIELLY

Sand injectites characterisation around the Martin Linge area using integrated seismic analysis and advanced geophysical techniques

Master thesis, 2024

Energy, Reservoir and Earth Sciences programme

Faculty of Science and Technology

Department of Energy Resources

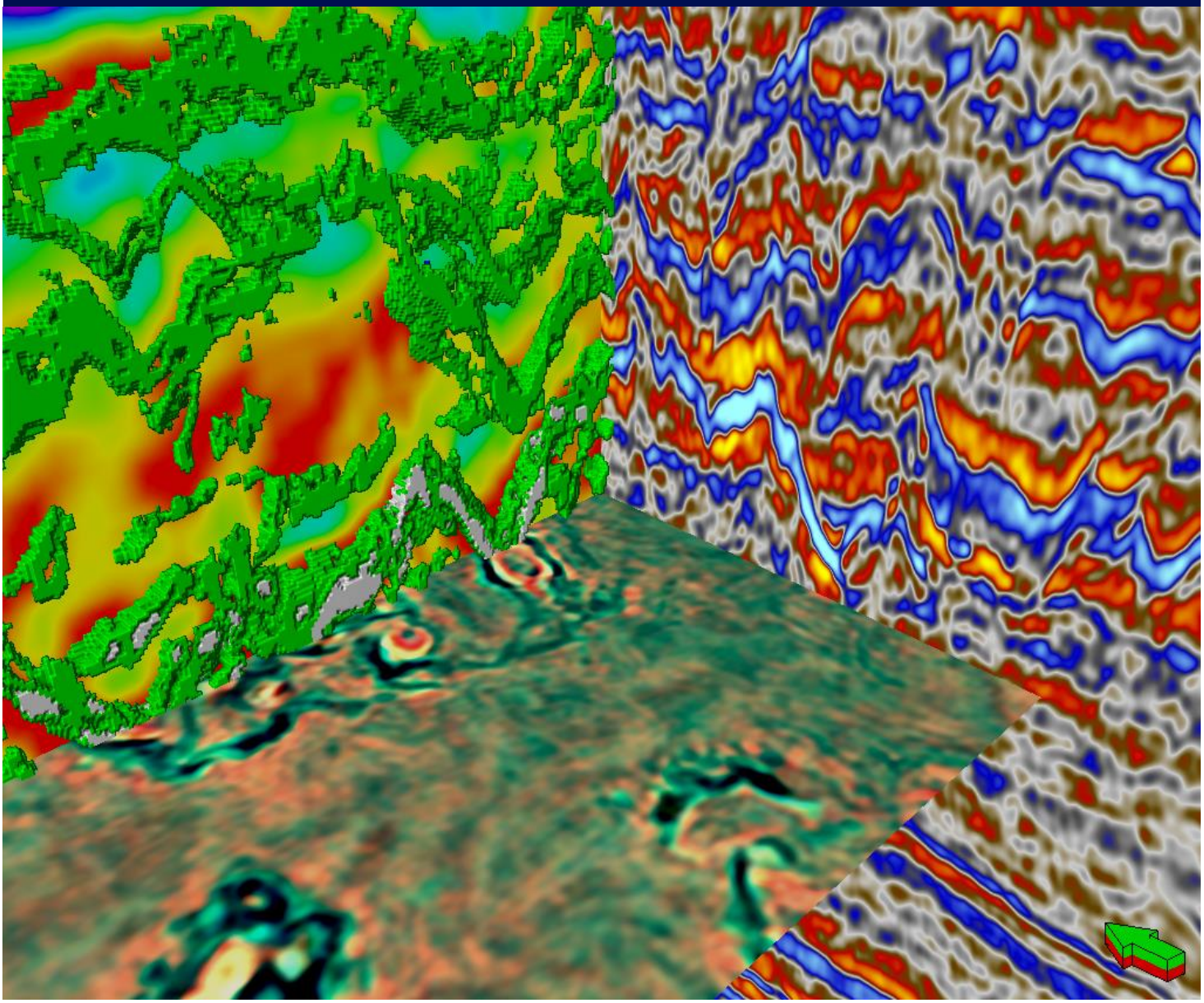

Acknowledgements

This thesis has been submitted for the fulfilment of the MSc degree in Energy, Reservoir, and Earth Sciences at the University of Stavanger.

I extend my sincere gratitude to my academic supervisors, Nestor Cardozo and Lothar Schulte, for their exceptional mentoring, encompassing both the technical and theoretical aspects and for their insightful feedback critical to the success of this thesis. Furthermore, my gratitude extends to my external supervisors from the Martin Linge area RIM team at Equinor AS — Geoff Minielly, John Williams, and Adam McCarthy — for their outstanding guidance, educational interactions, and valuable recommendations, which significantly contributed to the successful completion of this project. I also acknowledge Equinor ASA for granting access to the dataset and software that was utilized in this thesis.

My heartfelt thanks go to my girlfriend, Elizabet, for her unwavering support throughout this research. Lastly, I am deeply appreciative of my family, most notably my father, Viktor, who serves in my homeland's armed forces. His dedication provides a profound source of inspiration and motivation.

INJECTITE CHARACTERISATION AROUND THE MARTIN LINGE AREA USING INTEGRATED SEISMIC ANALYSIS AND ADVANCED GEOPHYSICAL TECHNIQUES

Artem Korniienko

The University of Stavanger, 2024

Supervisors: Nestor Cardozo, Lothar Schulte, Geoff Minielly

Abstract

Although sand injectites have superior permeability and are promising targets for hydrocarbons and subsurface storage, they are relatively underexplored elements within the energy sector. There is a significant gap in understanding their origin, shape, and anisotropic properties. The uncertainty in sand injectite geometry can be mitigated through the application of sophisticated geophysical methods, which may offset the risks associated with exploring such formations.

This thesis delves into the detailed seismic analysis of sand injectites within Paleogene strata in the area around the Martin Linge field. Techniques such as spectral decomposition, amplitude versus offset (AVO), and extended elastic impedance (EEI) are used to analyse these bodies. The study area encompasses a km-scale mass transport complex situated between the Martin Linge and Oseberg fields, along the western and eastern margins of the Central Viking Graben in the northern North Sea.

The objective is to apply the techniques above for imaging sand injectites to determine their effectiveness and limitations. I also look at various challenges such as differences in sand injectite thickness and the presence of uncemented sands.

The thesis begins with spectral decomposition using various frequency bands to determine the tuning thickness of cemented and uncemented sand injectites. Next, AVO modelling is performed to create AVO class volumes defining the characteristics and fluid content of the sand injectites. Then, EEI is utilized to construct models of lithology and fluid volumes, integrating different chi angles to accentuate changes in lithology and fluids within the sand injectites and host claystone.

The results of the thesis demonstrate that while spectral decomposition marginally enhances the visualization of cemented sand features, it fails in detecting thinner sand injectites. Contradictions arise in AVO modelling as models based on well log data predict AVO Class II or III for studied injectites, but AVO analysis from seismic data leans towards a less certain Class I, although it still proficiently differentiates between shale and sandstone. Extended Elastic Impedance (EEI) analysis effectively discriminates between shale and sand, distinctly revealing uncemented top sands obscured in other seismic cubes. EEI at -45º angle proves to be the most effective method, sharpening the definition of sand injectites' boundaries and facilitating precise geobody extraction.

This approach improves the mapping, reservoir characterization, and resource estimation of sand injectites, and the understanding of the analysed injection complex. The study highlights the advantages of employing the selected geophysical techniques and provides valuable insights for hydrocarbon exploration and production in the Martin Linge area and similar settings.

Contents

List of Tables

List of Figures

1. Introduction

Sand injectites, also known as remobilized sands, were relatively unknown until the early 1990s when they began to be recognized by geoscientists as prospective hydrocarbon reservoirs. The ongoing energy transition has induced the search for better solutions and the exploitation of available resources. Exploration and production from sand injectites over the past few decades have demonstrated their significant potential for both oil and gas (O&G) and geological storage. Nonetheless, sand injectites pose numerous challenges due to their intricate geometry, anisotropic properties, and complex origin. Yet, there is a noticeable lack of knowledge about these features. However, with the advent of new methodologies and the utilization of big data, it is possible to overcome some of these obstacles and address uncertainties.

This thesis aims to shed light on some of the questions concerning the geometry of sand injectites and their imaging and interpretation across different seismic volumes. Spectral decomposition, amplitude versus offset (AVO), and extended elastic impedance (EEI) are applied to sand injectites, and the effectiveness, limitations, and accuracy of these techniques in imaging remobilized sands are evaluated.

The Norwegian continental shelf (NCS) is an area of long geological history and economic importance, especially due to its abundant oil and gas reserves. Among the various fields in the region, the Martin Linge field, previously referred to as Hild, is notable for its strategic position and intricate geological features. Discovered in 1978, this offshore oil and gas field is in the northern North Sea, and it is distinguished by its geologically complex, high-pressure gas/condensate reservoirs. This distinctive geological configuration presents a mix of prospects and challenges for hydrocarbon exploration and production.

This thesis explores the characterization of sand injectites in the area surrounding the Martin Linge field. By concentrating on the Martin Linge field, this study aims to enhance the knowledge of injectite systems and their impact on hydrocarbon exploration in this area. The research utilizes cutting-edge geophysical methods and integrates diverse data sets to offer an in-depth examination of the injectite features, potentially facilitating more efficient exploration and production in the future.

1.1 Objectives and motivation

The main objective of this research is to address the challenges in delineating and characterizing sand injectites in the vicinity of the Martin Linge field by employing a suite of integrated geophysical methods. The study aims to pinpoint the seismic signatures of these injectites, including those that are below the resolution of seismic imaging and those involved in complex interactions with surrounding strata. By combining seismic attributes with well log data and utilizing sophisticated techniques such as spectral decomposition, amplitude variation with offset (AVO), and extended elastic impedance (EEI), the research intends to deepen our knowledge of the properties and dynamics of sand intrusions. This can improve the approaches used in exploring and developing hydrocarbons and in geological storage in these sand bodies.

This thesis will address the following questions by integrating geophysical and geological data:

- How can spectral decomposition be used to detect thin sand injectite bodies that are not visible on the reflection seismic?
- What kind of AVO anomalies do injectites exhibit, and how can these assist in mapping their geometry? Additionally, how do these anomalies manifest in AVO volumes derived from well logs and seismic data?
- In what ways can EEI help to overcome the challenges related to the geometry of injectites? Which chi angles are most effective for analysing sand intrusions?
- What are the optimal methods for mapping the top of uncemented sand layers?
- The process of identifying leads that could be developed into prospects for exploration.

1.2 Description of study area

The study area encompasses the Paleogene interval surrounding the Martin Linge field, a producing field situated close to the UK sector boundary in the northern North Sea, 42 km west of the Oseberg field. The water depth at this location is 115 m. Martin Linge was discovered in 1978 and its development and operation plan (PDO) was approved in 2012. The field primarily extracts gas and condensate from a Middle Jurassic sandstone formation within the Brent Group. The reservoirs are known for their structural complexity and are classified as high pressure and high temperature (HPHT), with depths ranging from 3700 to 4400 m. Additionally, oil is extracted from the Eocene Frigg Formation at a depth of 1750 m (Norwegian Offshore Directorate, 2024). Production commenced in 2021 (Norwegian Offshore Directorate, 2024). The area under study includes a km-scale sand injectite complex located between the Martin Linge and Oseberg fields (Figure 1).

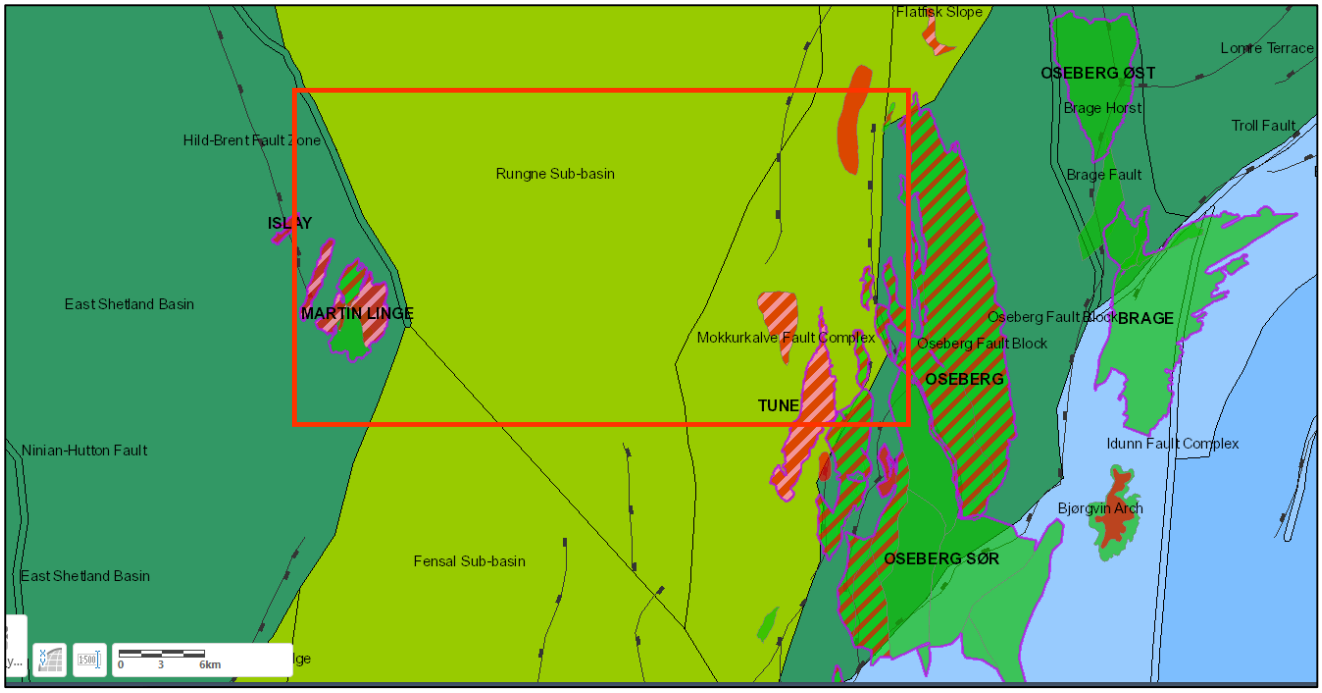

Figure 1: Location of the study area (red rectangle), structural elements (faults and basins), and nearby fields (gas – red, oil - green). From NOD Factpages (2024)

1.3 Previous work

Various studies have been carried out by geoscientists with objectives that align closely with the ones of this thesis, yet they exhibit certain differences.

The AVO characteristics of top sand injectites within different types of host rock claystone were examined by Øygarden et al. (2014). Their modelling involved the use of both measured and calculated shear velocities, as well as fluid substitutions. The scope of their research was confined to well log data and did not include AVO modelling using seismic data.

The behaviour of sand injectites on the NCS in response to spectral decomposition was explored by Kouidri et al. (2017). Their study examined a large regional injection complex spanning 10 km and devoted less attention to smaller-scale injections and their signatures in spectral decomposition.

Lastly, the application of extended elastic impedance in the mapping of sand injectites has been a subject of active research by PGS. Pernin et al. (2022) focused on investigating the V_p/V_s ratios of sand injectites from the Paleocene North Sea.

1.4 Thesis structure

The organization of the thesis is as follows:

Chapter 1 introduces the central theme of the research and outlines its primary goals.

Chapter 2 describes the geology around the Martin Linge field area, with details about the sand injectites.

Chapter 3 describes the seismic and well data that were utilized in this analysis.

Chapter 4 deals with sand injectites, explaining their formation processes, types of structures, geometry, and detectability.

Chapter 5 sets forth the theory for the seismic modelling techniques employed in the thesis.

Chapter 6 describes the methodologies applied in the thesis, covering the procedures used to construct models as well as the parameters implemented for seismic modelling and sensitivity analysis.

Chapter 7 describes the results from Chapter 6 in relation to the objectives of the research.

Chapter 8 analyses the key results and suggests directions for future research.

2. Regional geology

This chapter discusses the geological setting of the study area. Section 2.1 summarizes the main tectonic events with associated lithostratigraphy. Section 2.2 discusses the depositional environments.

2.1 Structural and Stratigraphic evolution

The Viking Graben basin is a rift basin in the Northern North Sea continental shelf, which stretches from the East Shetland Platform to the Øygard Fault Complex (Glennie & Underhill, 2009). The Northern part of this rift basin formed across the Lower Paleozoic Caledonian orogenic belt. During the Mesozoic, this area went through two episodes of rifting – in the Permian-Early Triassic and in the Middle Jurassic – Early Cretaceous. After that, the Northern North Sea went through periods of post-rift thermal cooling.

The first episode of rifting in the Permian-Early Triassic initiated major half grabens. The Central Viking Graben system in the North Sea was likely established during the Triassic, but the graben had a different structural configuration than the present (Ziegler, 1990). The middle Jurassic sediments were deposited in an intraplate tectonic setting, during an intra-rift period of thermal doming (Glennie & Underhill, 2009; Ziegler, 1990). The North Sea Central Graben system was established during the second phase of rifting. During the Paleocene, the uplift of the basin margins and rapid subsidence of the graben accompanied the last episode of the Greenland-Sea rifting (Ziegler, 1990). Exceptionally rapid post-rift subsidence during the Palaeogene era, triggered by the thermal uplift of the Shetland platform, facilitated the deposition of extensive Paleocene-Eocene sediments, featuring crucial reservoir and seal intervals.

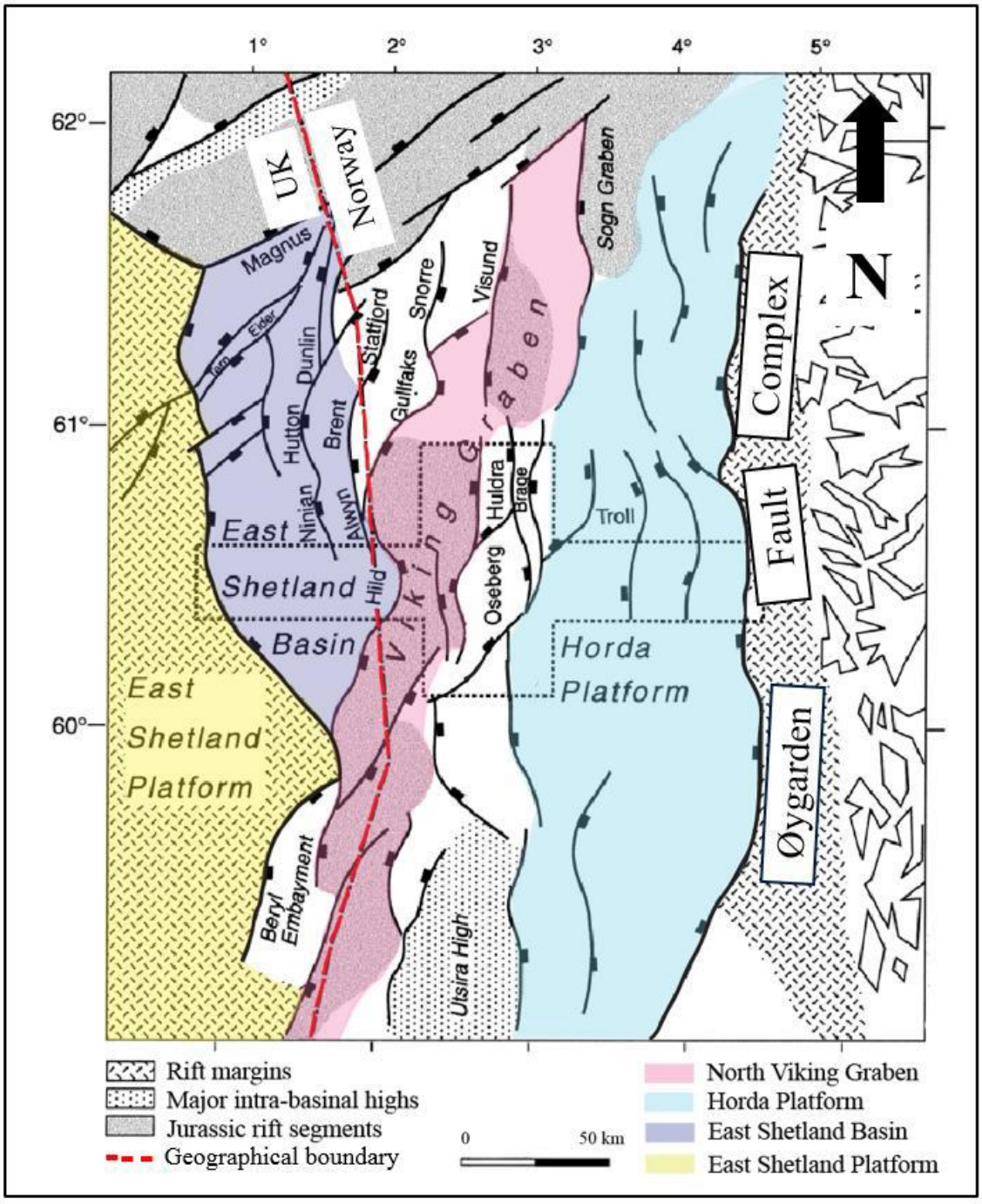

Figure 2: Main structural elements of the northern North Sea, Viking Graben and its surrounding. Martin Linge field is shown as the former Hild field. From Kausar (2018)

2.1.1 Paleogene

The Paleogene was marked by a dynamic phase of compression, which was influenced by the opening of the North Atlantic and the Alpine orogeny (Ravnås et al., 2000). Sedimentation in the vicinity of the Martin Linge area during the Paleogene was linked to various events (Figure 3):

- The Paleocene is distinguished by the beginning of thermal uplift along the margins of the basin, resulting in 2-3 km elevation in Scotland and the initiation of the North

Atlantic Igneous Province, as well as the formation of the Thulean Plateau due to the Iceland Plume volcanic activity.

- In the Early Eocene (54 Ma) volcanic events led to the deposition of the Balder tuff through ash deposition, and by the Late Eocene, the basin reverted to a state of passive thermal subsidence and experienced a widespread drop in sea level (Ravnås et al., 2000).

- The Early Oligocene (34 Ma) commenced with the beginning of glaciation in Antarctica, which brought global sea level fluctuations (Ziegler, 1990).

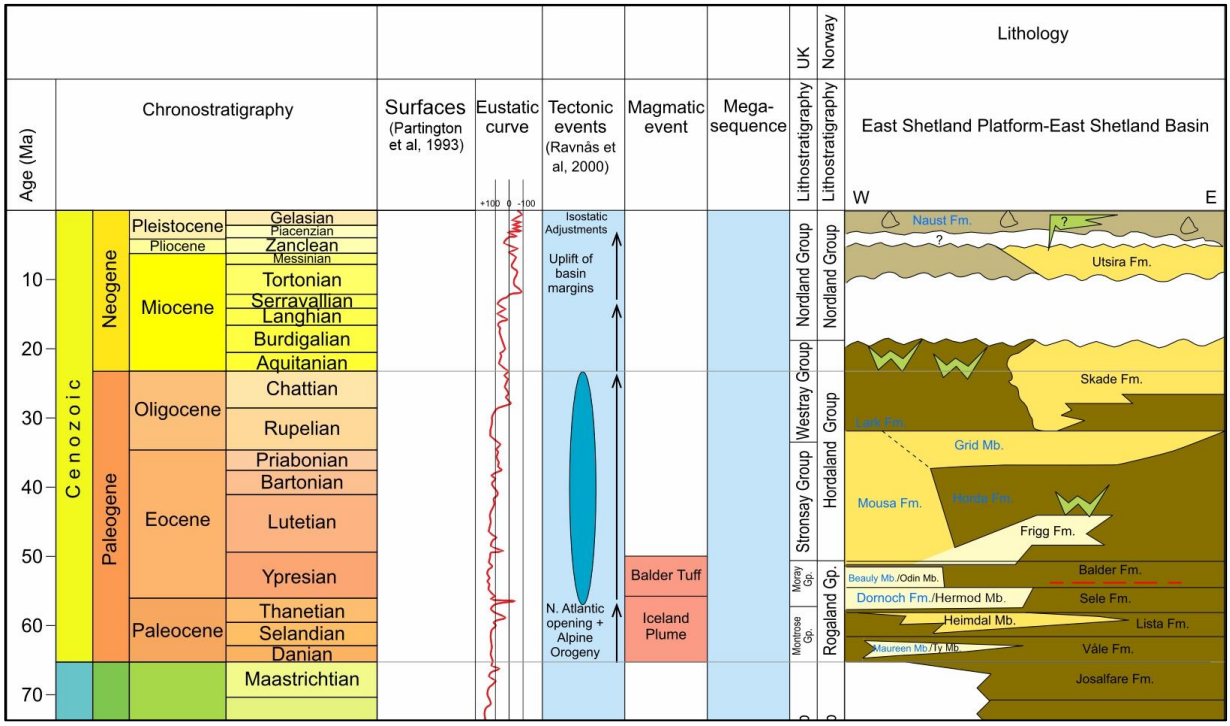

Figure 3: Generalized lithostratigraphic column of the studied Cenozoic interval. From Equinor UK 33rd Licence Round Martin Linge Area Application (2022)

In the East Shetland Basin, Paleogene subsidence was largely independent of fault movement. However, the transition from platform to basin, which was controlled by large pre-Tertiary half-grabens, continued to exert an influence on sedimentation (Lee & Hwang, 1993). Consequently, Paleocene and Eocene sediments, sourced from the west and represented by the Frigg Formation, spilled over the platform into the basin-forming delta and submarine fan deposits (Figures 4a and b). Deltaic progradation in the East Shetland Basin took place during the mid-to-late Paleocene when the N-S-elongated Dornoch delta was deposited. The delta complex was confined to areas to the south of the Tern-Eider Ridge, which suggests a broad tectonic control on its distribution. The locations of the thickest sand trends also appear to be coincident with the underlying Mesozoic half-grabens, e.g. Brent and Hutton areas, which indicate brief rejuvenation of the major boundary faults (Figure 4b). Subtle structural control is also seen in the distribution of the Lower Eocene submarine fan sandstones and the position of the shelf break (Lee & Hwang, 1993). Both were strongly influenced by the presence of underlying Mesozoic half-grabens and their bounding faults (Figure 4a).

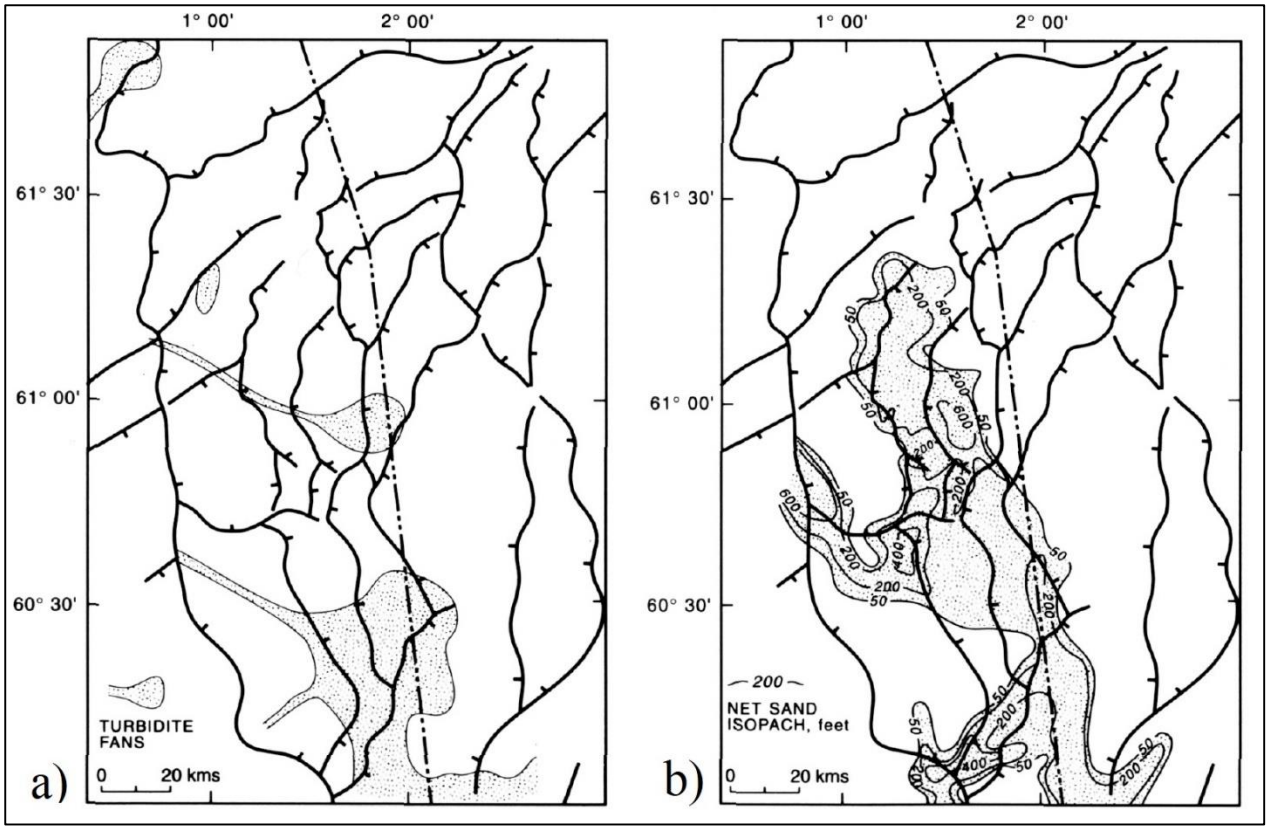

Figure 4: Regional isopach and sandstone distribution maps of the East Shetland Basin. (a) Distribution of the Paleocene delta system. (b) Distribution of the lower Eocene turbidite fans. Modified after Lee & Hwang (1993)

2.1.2 Neogene-Present day

During the Miocene era, a deltaic system emerged from the Shetland Platform, extending towards the Norwegian sector of the North Sea. This system is characterized by the Skade and Utsira Formations. Significant uplift and Quaternary glacial erosion of the Norwegian mainland resulted in the deposition of substantial sedimentary sequences into the North Sea during the Neogene period (Lepercq & Gaulier, 1996). Consequently, Jurassic source rocks were buried to depths conductive to hydrocarbon generation, while the seals became effective.

2.2 Depositional environments of the Hordaland Group.

The presence of injected sands in the vicinity of the Hordaland Group and the depositional environments of this group plays a pivotal role in the genesis of sand injectites and their potential sources—the Frigg, Grid, and Skade Formations (Løseth H et al., 2003). These formations are intersected by sand injectites, and there has been discussion about them being the probable source of the remobilized sands (Pernin N et al., 2019). Nonetheless, the thickness of each of these formations varies throughout the area of study, while the remobilized sands are consistently present across the entire area under investigation.

Frigg Formation: The Frigg Formation (Lower Eocene) comprises sandstones that were deposited as submarine fans through gravity flows sourced from the East Shetland Platform (Figure 5), west of the East Shetland Basin (Isaksen & Tonstad, 1989). The gravity-driven deposition resulted in a formation that exhibits variable thicknesses across short distances, ranging from 140 to 300 m. The formation is composed of sandstones interspersed with lenses

and layers of silty claystone (Anell et al., 2011). The sandstones are loosely cemented, varying in colour from light brown to yellowish-beige, and contain micaceous and carbonaceous materials. Grain size varies from very fine to medium, with some layers even being coarse-grained. Noteworthy is the presence of calcareous cement within some layers—a feature also observed in remobilized sands.

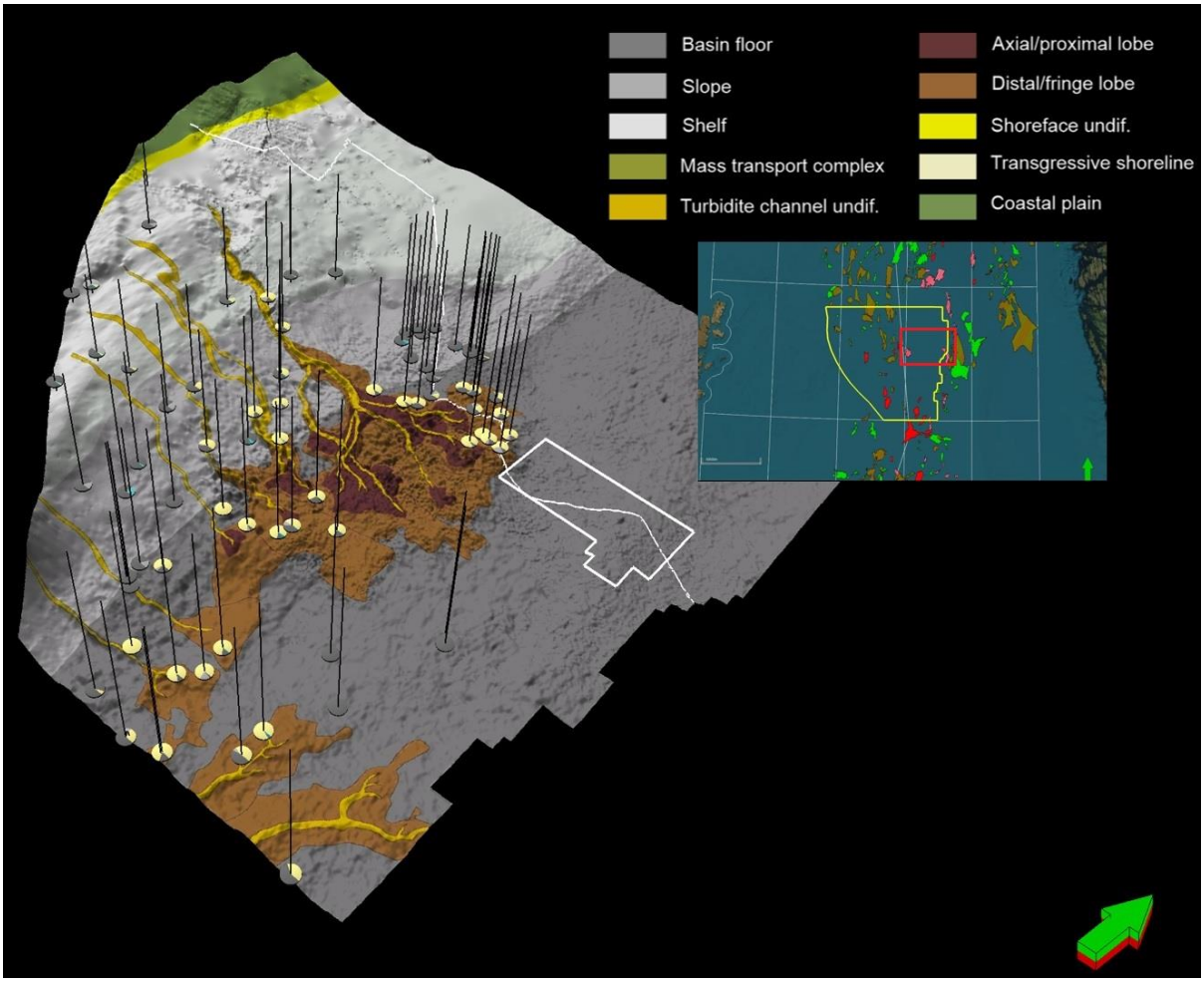

Figure 5: The conceptual model of the Frigg Formation within the area marked by the yellow rectangle on the inset map. The study area is the red rectangle on the inset map. Modified from Equinor (2023)

Grid Formation: The Grid Formation spans the Middle to Upper Eocene and consists of sand deposits likely originating from the East Shetland Platform. The Grid Formation thins towards the east and is believed to have been deposited in an open marine setting during a regression (Isaksen & Tonstad, 1989). This is supported by evidence of Late Eocene sea-level fall (Haq et al., 1987). The formation contains sandstones interspersed with claystone and siltstone layers. Sandstone beds commonly appear massive and "blocky" with an absence of significant fining-upward or coarsening-upward sequencing – similar trends observed in cross-cutting injected sands. The sand grain sizes predominantly range from very fine to fine, though occasionally they may be medium to coarse (Isaksen & Tonstad, 1989).

Skade Formation: The Skade Formation is Lower Miocene and is composed of marine sandstones, mostly turbidites, that spread over a vast area of the Viking Graben (Isaksen & Tonstad, 1989). Its thickness can exceed 300 m whilst rapidly decreasing toward the east of the Viking Graben, transitioning into shale. The coloration of the sandstones varies from clear

to light grey, and they are fine to medium size, but they can be occasionally coarse (Anell et al., 2011). The grains tend to be subrounded to rounded and are moderate to well sorted. Embedded within the sands are traces of fossils, shell fragments, mica, and abundant glauconite (Isaksen & Tonstad, 1989).

3. Data

In this thesis, seismic and well data from the Martin Linge field have been employed. The dataset was supplied by Equinor ASA and will be described in the next sections.

3.1. Seismic dataset

The seismic data used in this thesis consists of 3D angle stacks: near-stack (5-15º), middle-stack (13-23º), far-stack (21-31º), and ultra far-stack (29-39º). These data encompass an extensive area, but for this thesis, the volume has been cropped to approximately 175 km^2 (Figure 6). Inlines and crosslines are aligned in the north-south and west-east directions, respectively. Furthermore, the dataset includes information up to about 2500 milliseconds (ms) of two-way travel time (TWT). The interval of focus for the study lies between approximately 1000-2000 ms TWT. The seismic data are pre-stack depth migrated (PreSDM), zero-phase, and follows reverse polarity, where a negative through shown as a red reflection indicates a decrease in acoustic impedance (AI), and a positive peak depicted as a blue reflection suggests a rise in AI (Figure 9).

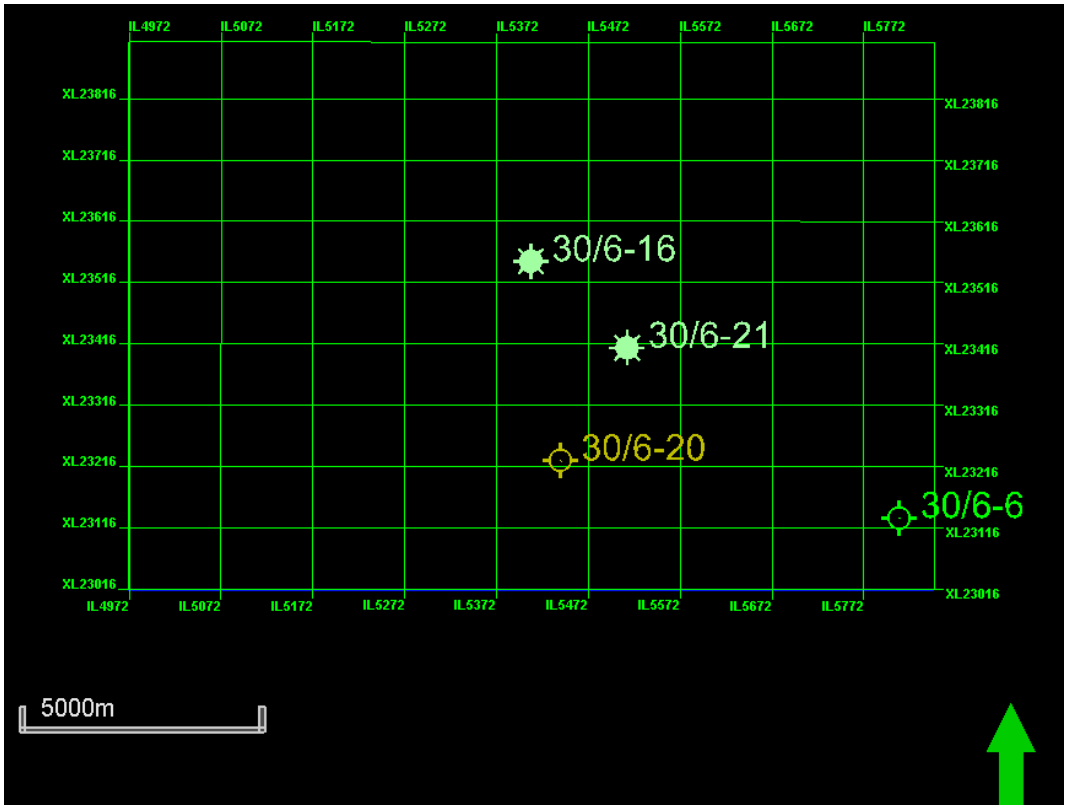

Figure 6: Outline of the seismic data boundaries and the locations of the wells.

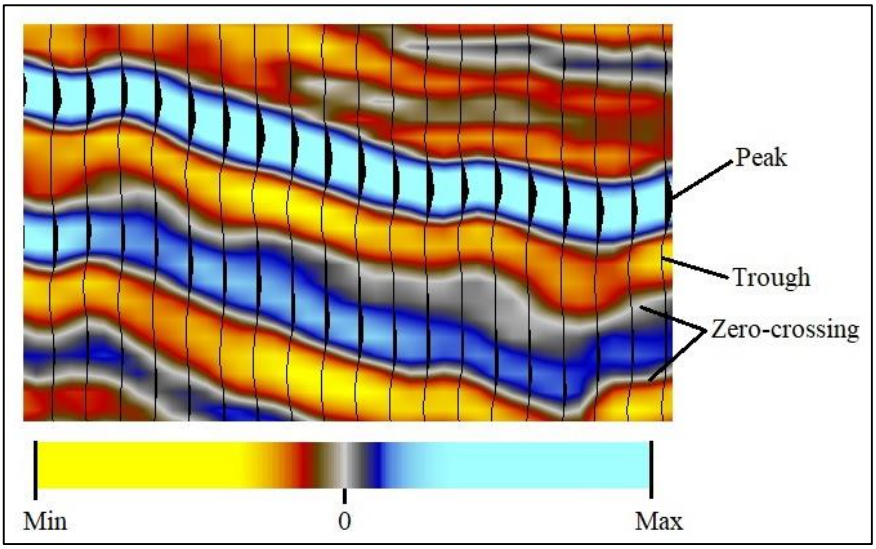

Figure 7: Vertical section through the seismic cube with a wiggle trace visualization to highlight the polarity characteristics of the data.

3.2. Well data

Within the study area, although multiple wells are accessible, well 30/6-20 has been utilized for its comprehensive suite of logs—including gamma-ray (GR), density (RHO), and sonic (DT and DTS)—and because it penetrates the remobilized sands (Figure 8). The sonic logs from well 30/6-20 were utilized for determining the compression wave (V_p) and shear wave (V_s) velocities in the sand injectites. A summary of the well can be found in Table 1.

Table 1: General information about the wells used in the study. Information from NOD Factpages (2024)

Well name	30/6-20
NS degrees	60° 37' 20.52" N
EW degrees	2° 42' 18.52" E
Completion date	13.04.1986
Status	Plug and abandoned
Type	Exploration
Content	Shows
Total depth (MD)	3046.0

Well tops were available for key stratigraphic levels: the top of the Frigg Formation, the Sele top, the base and top of the Grid Formation, and the top of the Shetland Group. Moreover, checkshot surveys were also available, enabling the creation of time-depth curves along the well. This allowed representing the well data in both time and depth domain. Well 30/6-20 was utilized for seismic to well tie, aid in the interpretation of seismic data, and to attribute petrophysical properties to the injectites.

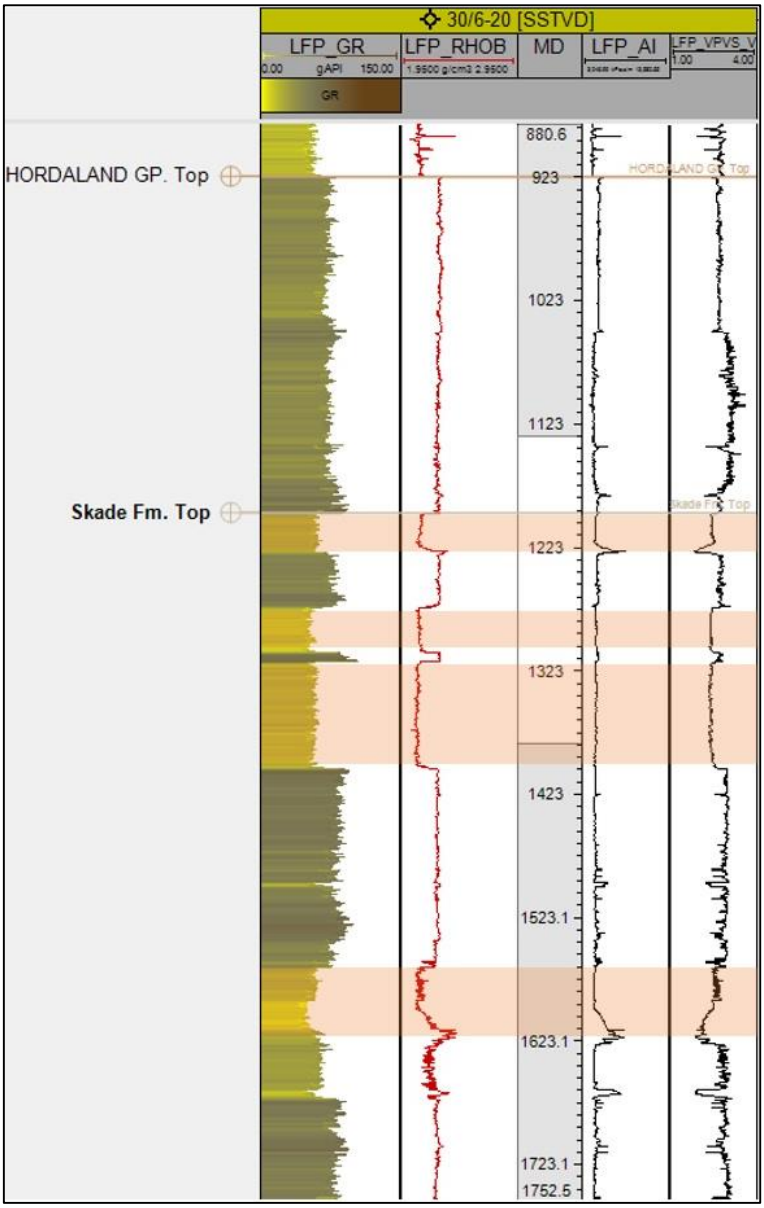

Figure 8: Logs from well 30/6-20 at the interval of study. Sand injectites are highlighted in orange.

4. Sand injectites

This chapter examines both the worldwide and regional presence of sand injectites (section 4.1), the conditions and processes for their formation (sections 4.2 and 4.3), as well as their geometry and chances to identify them using seismic techniques (sections 4.4 and 4.5).

4.1 What is a sand injectite?

In this thesis, the collective term "sandstone intrusion complexes" is used to refer to all instances of remobilized and injected sandstones. The term post-depositional sand remobilization describes the movement of a body of sand away from its initial deposition site after deposition has occurred, resulting in the sand being in a loose or unconsolidated state. Sand injectites are geological structures created through this process, developing intrusive formations that bear a resemblance to igneous intrusions in both their appearance and relationship to surrounding rock layers (Figure 12).

Interest in injectites within Paleogene sandstones in the North Sea has surged due to successful hydrocarbon production from these bodies in major fields such as Alba, Balder, Grane, Leadon, Volund, and Chestnut (Lonergan et al., 2000; Huuse et al., 2004; Hurst & Cartwright 2007).

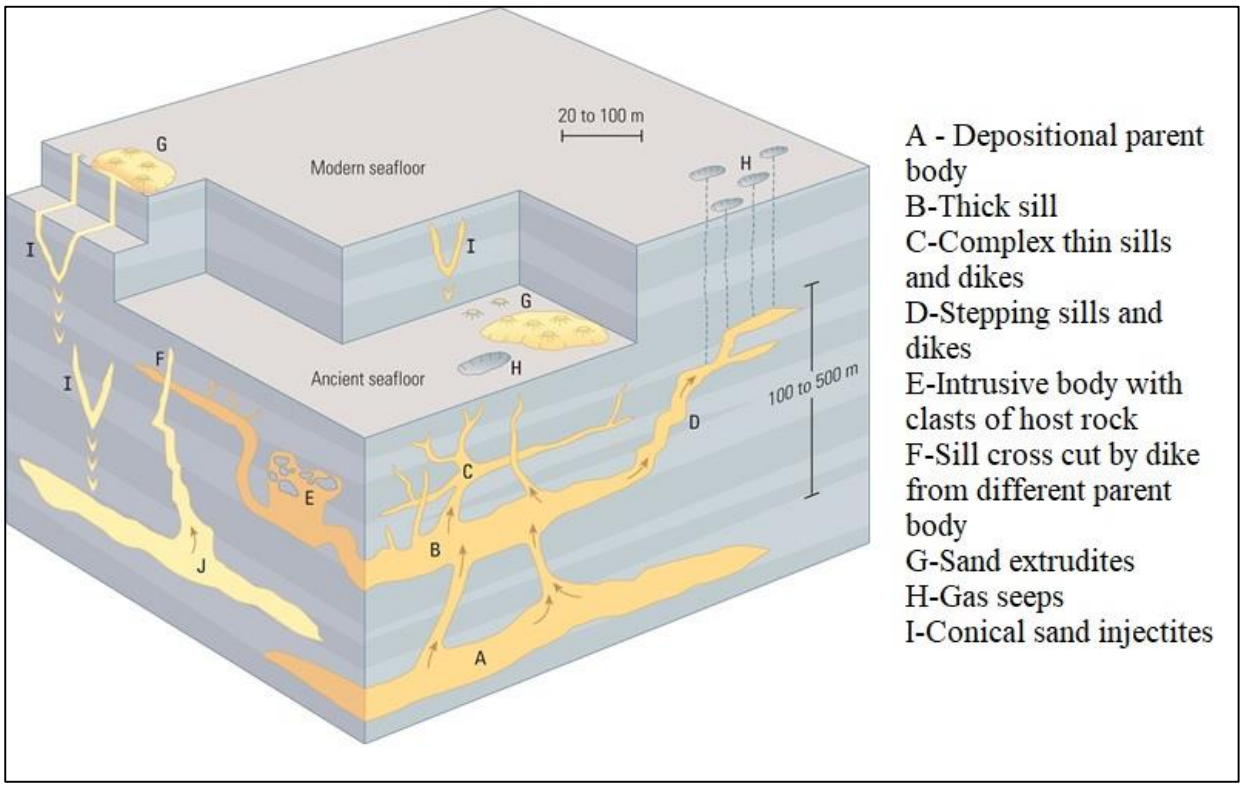

Figure 9: 3D schematic illustrating typical features of sandstone intrusions. From Braccini et al. (2008)

The North Sea Intrusion Province (NSIP) is recognized as the largest sandstone intrusion province globally, spanning an area of approximately 40,000 km^2 along the central axis of the basin. It extends from the North Viking Graben to the Central Graben and encompasses regions of the Outer Moray Firth and the Norwegian-Danish Basin (Cartwright, 2010). The NSIP is characterized by a variety of structures, from the frequently observed conical sills to large

dome-shaped mounds (Huuse et al., 2005), with sizes that vary from the scale of core samples to entire reservoirs.

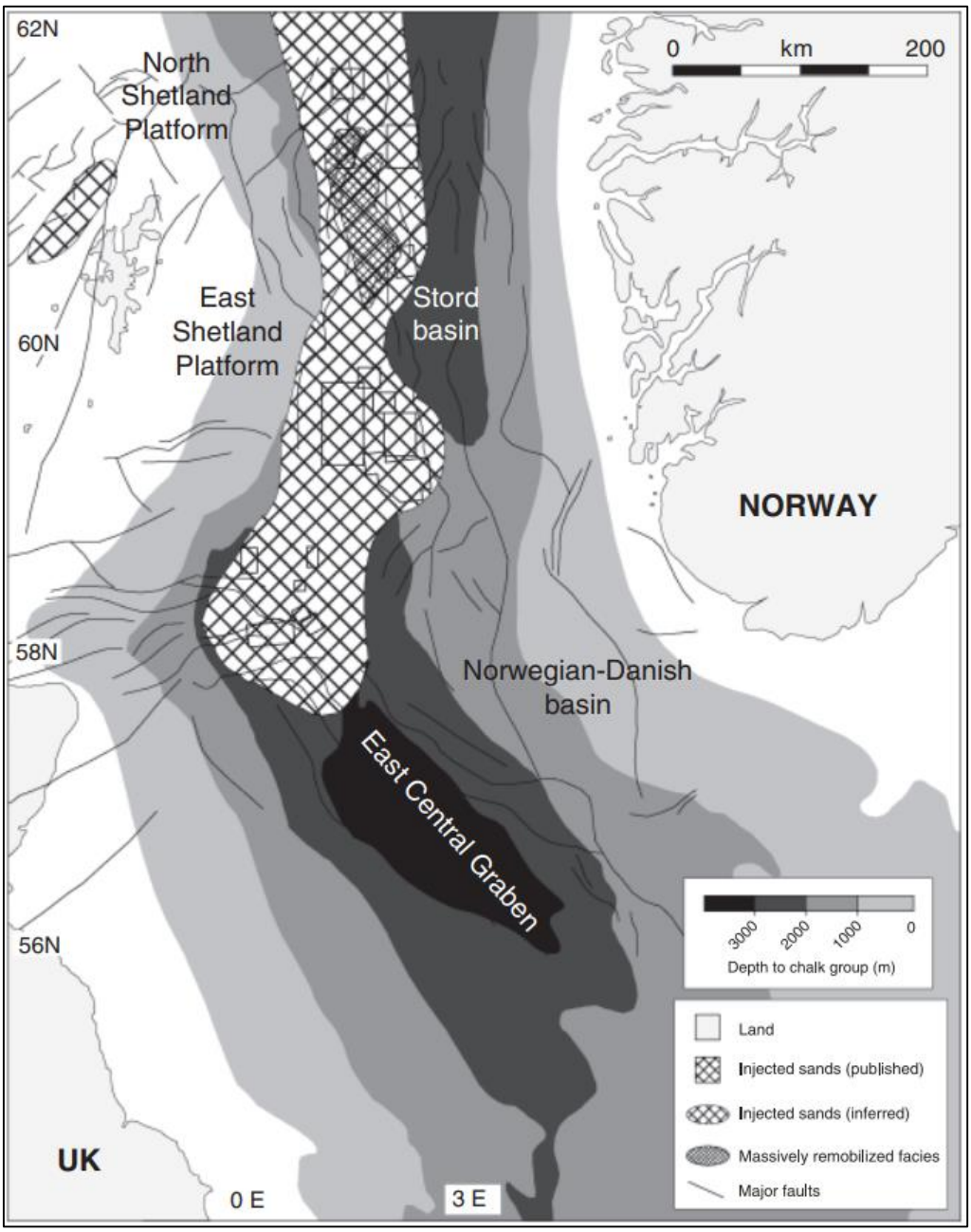

Figure 10: A map displaying the estimated area of sand remobilization and intrusion within the Lower Tertiary claystones of the North Sea Basin, covering approximately 40,000 km². For reference, the map also indicates the depth to the top of the Chalk Group. From Cartwright (2010)

4.2 How do sand injectites form?

The formation of sand injectites requires the following precursors (Figure 14):

1. Accumulation of overpressure
2. Breach of a sealing layer
3. Fluidization and subsequent injection into adjacent geological layers

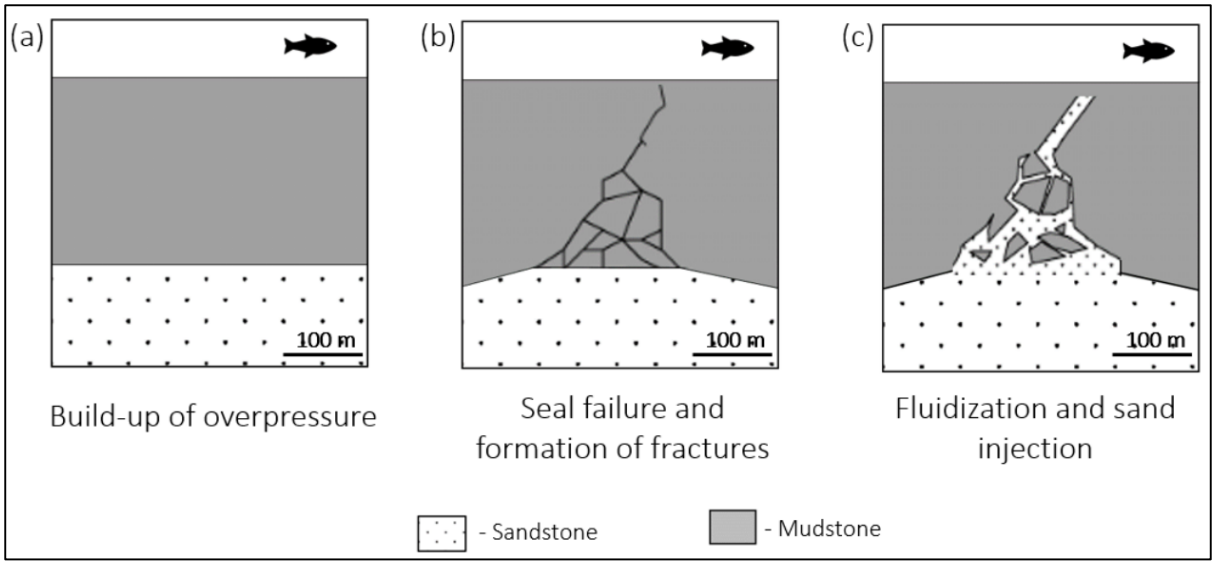

Figure 11: The development of sand injectites. a) The original sand, known as parent sand, is overlain by mudstone layers. The mudstone acts as a barrier, inhibiting the release of fluids from the sand beneath it, which results in the accumulation of overpressure. b) Cracks form in the mudstone cap once the overpressure within the sand surpasses the pressure at which the mudstone fractures. Sand overpressure may be triggered by various processes such as uneven compaction, seismic activity, or the influx of fluids from external sources. c) Once fractures form in the mudstone, the sand becomes fluidized and is then propelled into the fractures, forming sand injectites. From Bradaric (2020).

4.2.1 Overpressure

Excess fluid pressure, or overpressure, occurs when the pressure of pore fluids within a sealed system surpasses the hydrostatic pressure at a particular depth (Swarbrick & Osborne, 1998). Overpressure, as defined by Swarbrick and Osborne (1998), is any pore fluid pressure that is greater than the hydrostatic pressure, which is equivalent to the weight of a column of water at the same depth. This scenario suggests that the lithostatic pressure, the cumulative weight of the sediment column and its entrained fluids, is disproportionately supported by the pore fluids. The creation of overpressure necessitates the presence of parent sand—also known as source sand—which is an uncompacted sand body feeding material into the sand injectites. It is often challenging to pinpoint the parent sand. Nonetheless, research has demonstrated a preference for sand to be propelled upwards during injection, implying that the parent sand is likely to be below the sand injectites from a stratigraphic standpoint, although this isn't invariably the case (Cobain et al., 2017; Parize et al., 2007). A seal lithology is also essential for the build-up of overpressure within the parent sand. To effectively create such pressure, the seal must be cohesive and impermeable, often comprising materials like mudstone, and it must encapsulate the parent sand, barring the release of pore fluid, and allowing the overpressure to be sustained (Hurst et al., 2011). In the context of the Grane field, for instance, the smectite-rich Lista shale acts as the surrounding seal for the Heimdal sand and is known for its lower permeability compared to shales that contain minerals like illite and kaolinite, thus providing an effective seal (Mondol et al., 2008). Initially, when the parent sand is buried but not yet sealed, pore pressure aligns with the hydrostatic gradient (Figure 15). However, as the sand is further buried and becomes encapsulated by the seal, pore pressure starts to increase, gradually moving away from the hydrostatic pressure gradient. Continuing burial results in increasing pressure, which, if it reaches the fracture gradient of the seal—the pore pressure that the rock can take before

fracturing—will lead to hydraulic fracturing within or near the boundary of the seal and parent sand (Hurst et al., 2011). Although disequilibrium compaction, where sediments are unable to expel their pore fluids in response to sediment loading, is one mechanism that could theoretically drive pore pressure all the way to the fracture gradient and instigate hydraulic fracturing, there are other mechanisms believed to lead to the overpressure necessary to trigger sand injectites. These alternative triggers for sand injectites are discussed further in section 4.3.

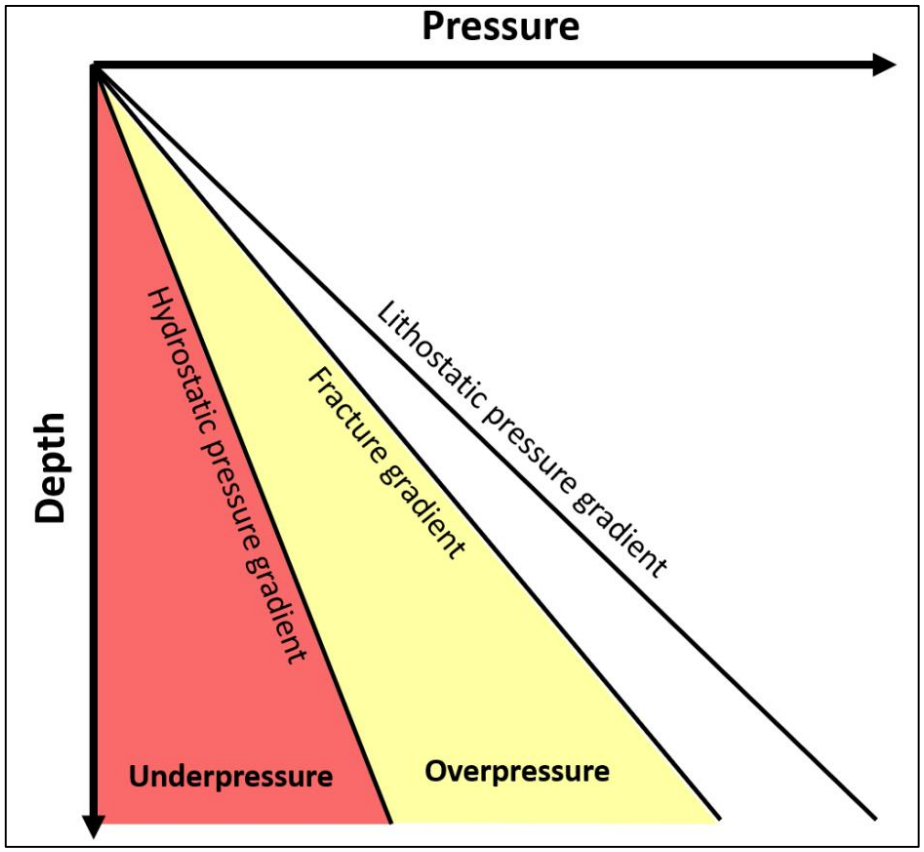

Figure 12: Illustration of fluid pressure in relation to depth under the assumption of increasing density with depth. This graph depicts the increase of hydrostatic, lithostatic, and fracture gradients in response to increasing depth. When the pore fluid pressure within a rock goes beyond the hydrostatic pressure, the rock is said to be in a state of overpressure. The lithostatic pressure is proportional to the cumulative weight exerted by the overlying layers, including the sediments and the fluids they contain. From Bradaric (2020)

4.2.2 Seal failure

Rocks subjected to stress respond variably based on their composition, the magnitude of stress, and the direction of the stress. As previously described, a sandstone dike can be thought of as a natural hydraulic fracture that grows and is later filled with sand (Jolly & Lonergan, 2002). For host rocks to fracture, they must possess a certain degree of cohesiveness, and any applied stress must be sufficient to exceed the tensile strength (T) of the rock. Deeper rocks tend to become more cohesive due to the increased compaction and reduced porosity that come with deeper burial. Host rocks for the parent materials of sandstone intrusions, as well as the intrusions themselves, are typically fine-grained sediments—often mudstones—with very low permeability. They have usually been buried deeply enough to accrue overpressure that can cause fracturing in the sedimentary layers, creating networks of fractures that can be filled by

the unconsolidated sands (Figure 16) (Hurst et al., 2011; Jolly & Lonergan, 2002). The existence of sandstone intrusions and other indicators of fluid movement like pockmarks and pipes are evidence of failure in the sealing system (Cartwright, 2010).

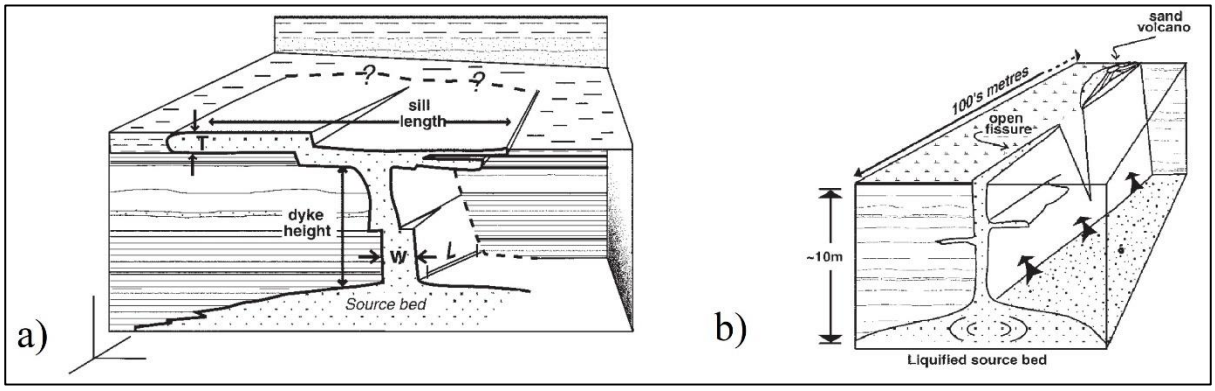

Figure 13: Illustrative diagrams of (a) intrusion of dikes and sills, and (b) the surface outflow resulting in an extrudite or sand volcano. The symbols W and L denote the width and length of a dike, correspondingly, while T denotes the thickness of a sill. Modified after Jolly & Lonegran (2002)

4.2.3 Fluidization

The last stage in the sequence of events leading to sandstone intrusions involves the transformation of sand into a fluid-like state within the networks of open fractures. This process, known as fluidization, occurs when sediment particles are lifted and suspended by the drag forces generated by the upward movement of fluids (Hurst et al., 2011). Fluidization enables the transport of non-cohesive sediment particles, allowing them to move from their original location or source sand body into the fractures (Figure 17) (Duranti & Hurst, 2004). Sandstone intrusions are crucial for the movement of hydrocarbons in the North Sea, with many fields showing that the remobilized and injected sands often serve as conduits for fluid flow, a finding supported by seismic and stable isotope analyses of carbon and oxygen from certain North Sea fields (Hurst et al., 2003). The onset of fluidization is marked by the pore fluid velocity surpassing a critical threshold, known as the minimum fluidization velocity (Hurst et al., 2011). Factors influencing this process include the size of the sediment grains, the degree of cementation, the density relative to the fluid, and the fluid's velocity and viscosity (Huuse et al., 2010). It is generally accepted that sandstones with fine to medium grains are more prone to fluidization due to their lower threshold velocities. However, even coarser-grained sandstones can be mobilized into a mixed state of smaller grains and fluid (Di Felice, 2010). Fluidization necessitates a substantial volume of fluid, which can originate from within the sediment pore spaces or from an external source (Huuse et al., 2010). This is particularly true in extensive sandstone intrusion regions like the North Sea, Faroe-Shetland, and San Joaquin basins, where additional fluids migrating from deeper areas within the basin to the parent body can significantly contribute to the mobilization and injection of sand (Huuse et al., 2010; Wild & Briedis, 2010). To put it simply, for grains to be mobilized, a pressure differential must be established across the sediment layer, ensuring that the drag force acting on the grains exceeds their weight (Jolly & Lonergan, 2002). This mobilization can be initiated by either internal or external factors.

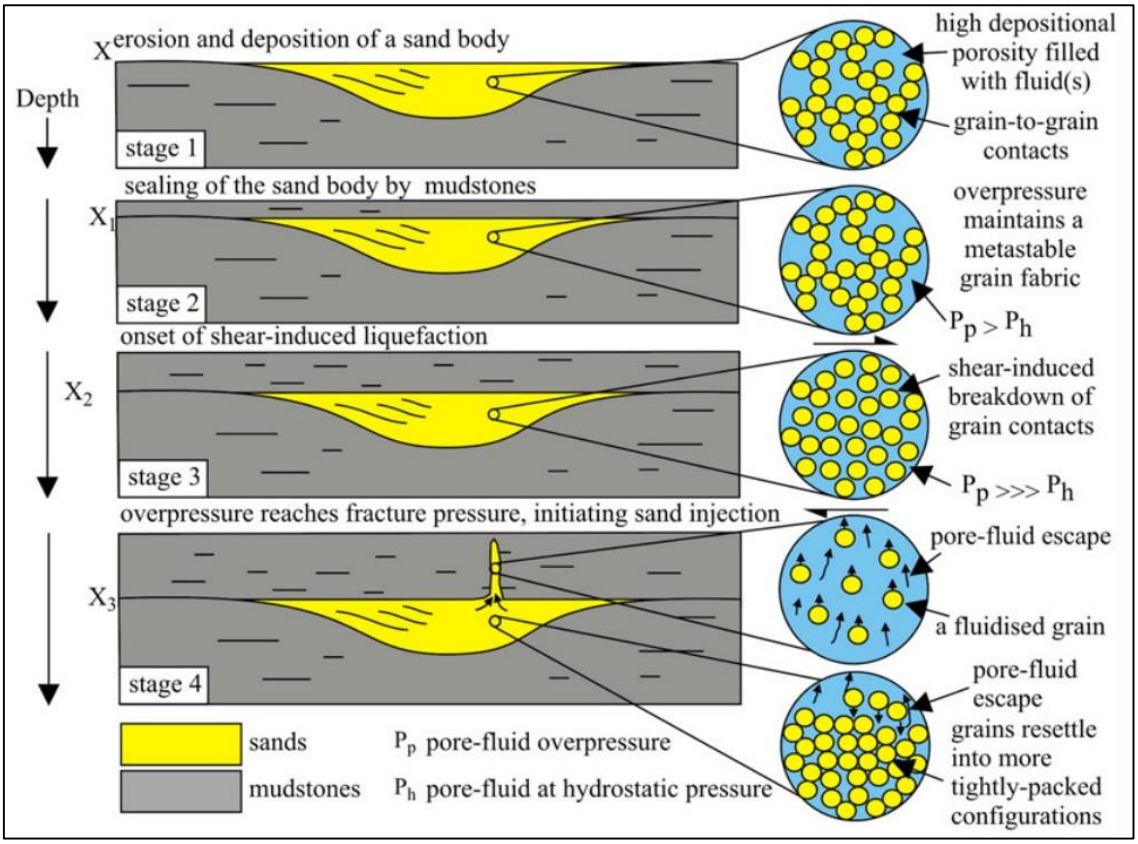

Figure 14: Diagrams depicting the impact of sand liquefaction and fluidization from the original depositional parent sand body throughout the burial process. From Hurst et al. (2011)

4.3 Trigger mechanisms

Sand remobilization and the subsequent injection can be kickstarted by a variety of trigger mechanisms, with some being more frequently observed than others. The precise process that triggers sand remobilization and subsequent injection, however, remains largely conjectural (Davies et al., 2006). This difficulty arises from the fact that the exact timing of the remobilization is usually not known, and pinpointing the source of sand is difficult. These triggering mechanisms may originate from internal or external sources, and the following primary factors: seismic shocks from high-magnitude earthquakes (Cartwright, 2010; Hermanrud et al., 2019), transfer of lateral pressure from post-depositional tilt and migration of water and/or hydrocarbons into encapsulated sand formations (Cartwright, 2010), disparity in compaction levels (Jackson, 2007), impacts by celestial bodies like asteroids (Cartwright 2010), flow of fluids from deeper sections in the basin, geological stressors such as tectonic movements (Huuse et al., 2010), and silica diagenetic transformation (Davies et al., 2006). However, large-scale, deep injectites are often associated with disequilibrium compaction combined with the movement of fluids into the parent sand (Hurst et al., 2011). The migration of hydrocarbons (oil and gas) has been mentioned in many instances as a contributing factor to injections (Jonk et al., 2005; Monnier et al., 2014). The influx of migrating fluids can increase the pore fluid pressure within a confined unit, leading to the breaking of the seal, fluidization, and subsequent injection. Despite extensive research, significant uncertainty remains. However, studies confirm that no single trigger mechanism can account for the formation of sand injectites globally. While one mechanism might predominate in one area, other triggers could also play significant roles within the same region (Hermanrud et al., 2019).

4.4 Sand injectite structures

Sand injectites can vary greatly in size, ranging from mm to several km, and they have been documented through core samples, surface outcrops, and seismic data (Hurst et al., 2011). These structures are known for their intricate shapes, creating steep formations that intersect, diverge, and suddenly end. Their resemblance to volcanic intrusions has led to the adoption of terms from igneous geology to describe them. The principal structural elements include:

- Sills - Borrowing from volcanic terminology, sills are intrusive formations parallel to the layers of rock (Figure 18). Sand injectite sills can vary in thickness and may appear as standalone features, extend into different layers within the host rock or branch off into distinct intrusions (e.g., Hurst et al., 2011).

- Dykes or wings - In line with terms used for igneous rocks, dykes are intrusive formations that slice through the bedding of the host rock (Figure 18). Sand injectite dykes may be straight and flat or notably uneven and bent (Parize et al., 2007). Wing-like sand injectites are steep dykes that project upward from the edges of sand bodies (Huuse et al., 2007).

- Conical sand injectites - These are discordant sand formations that appear as V-shaped profiles in cross-section and as bowl-like shapes in three dimensions. They often show up as strong amplitude anomalies in seismic data due to carbonate cementation (Cartwright et al., 2008). In the North Sea, large conical injectites are commonly found within the Paleogene layers (Cartwright et al., 2008; Løseth et al., 2013). Their dimensions range from 100-2000 m in diameter, 50–300 m in height, and 1–80 m in thickness, with an inclination of 20-50º (Cartwright et al., 2008).

- Irregular sand injectites - Some sand injectites display an irregular form that does not fit the typical categories of sills or dykes (Figure 18). These are marked by uneven boundaries and variations in thickness (Hurst et al., 2011).

- Sand injectite clusters - While sand injectites can occur in isolation, they are more frequently found in complex groupings (Hurst et al., 2011). In this context, the term “sand injectite clusters” refers to zones where multiple sand injectites come together to create an intricate web of interconnected structures that divide, merge, and intersect one another.

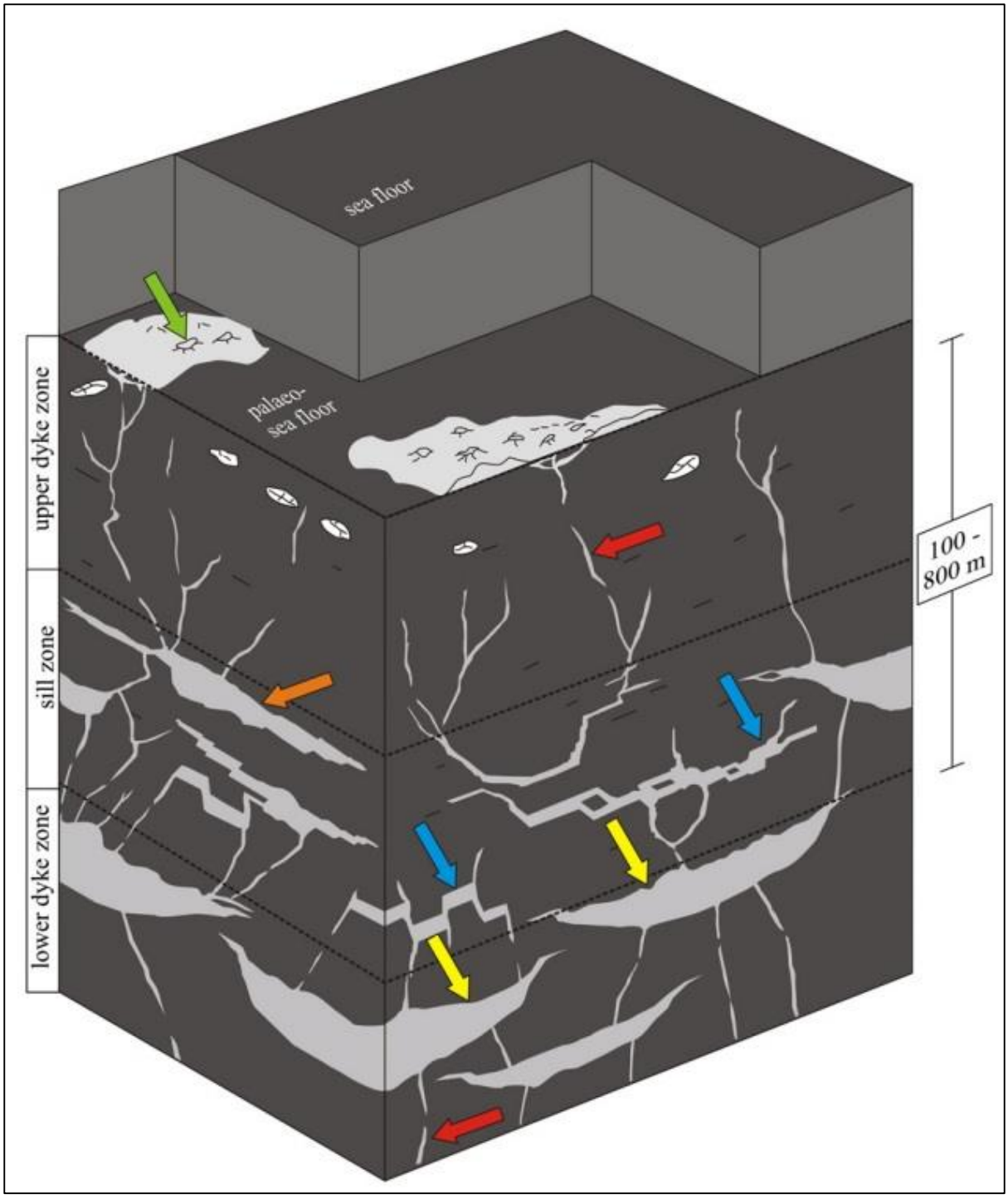

Figure 15: Sand injectite complex exhibiting a three-part structure as observed in outcrop and subsurface studies (revised from Hurst and Cartwright, 2007). The host rock is illustrated in dark grey. The diagram includes the remobilized source sandstone units (yellow arrows), vertical sandstone dikes (red arrows), horizontal sandstone sills (blue arrows), non-uniform sandstone intrusions (orange arrow), and sandstone extrusions (green arrow). From Hurst et al. (2011)

4.5 Seismic expression of sandstone intrusions

To grasp the challenges associated with the seismic imaging of sand injectites, it is essential to consider the seismic resolution and the concept of tuning thickness. These topics will be explored in a chapter devoted to the theoretical background. This chapter will focus on the visual seismic indicators of remobilized sands.

Sand injectites frequently create intricate and striking formations that are clearly visible on 3D seismic images (Løseth et al., 2003). One example is conical sandstone intrusions (Figure 16), which have been recognized more recently. Due to their size and context, they are particularly well-suited for imaging with 3D seismic. Typically, these intrusions are bowl- or cone-shaped, spanning 500 to 1500 m in diameter, and exhibit a circular to subcircular planform with a highly curved shape. When confirmed by drilling data, their thickness varies from 5 to 35 m. In the North Sea, these structures are often found in conjunction with polygonal faults within the Tertiary layers (Cartwright, 1994).

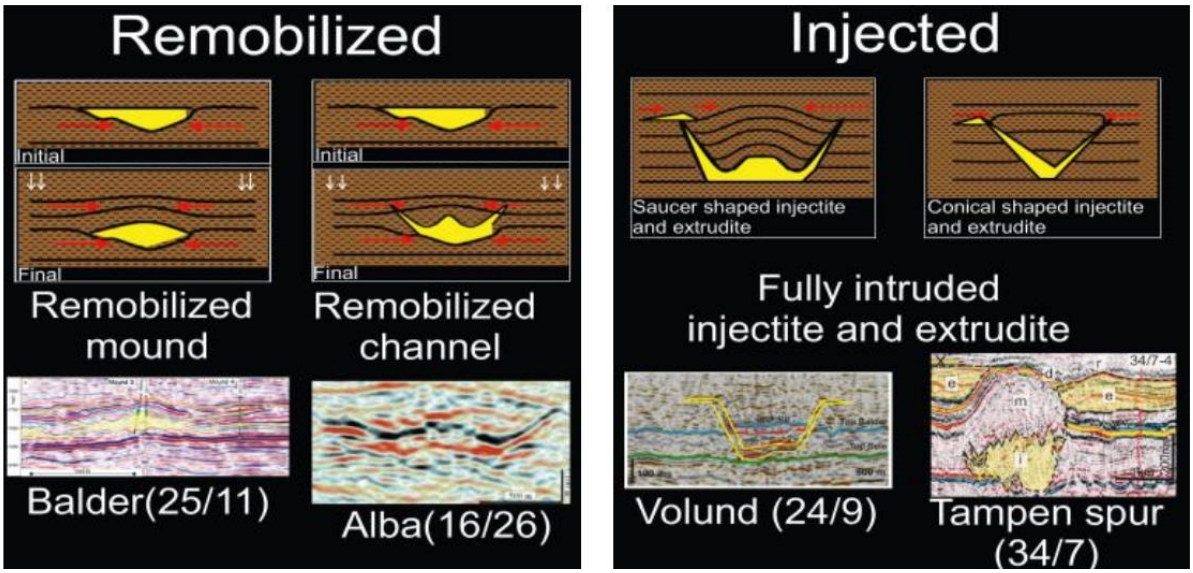

Figure 16: Remobilized and injected sandstones and their seismic signatures in the North Sea. From Huuse et al. (2009)

As depicted in Figure 17, the "hard" seismic reflections are generated by the presence of V-shaped sandstone that is partially cemented with carbonate. The sandstone cone sheet displays a notable asymmetry, suggesting either a less continuous sand presence on the western side or perhaps a lower degree of carbonate cementation (Figure 17). Above the sandstone cone sheet, there is a layer of chaotic seismic reflections, which are interpreted as disturbed sedimentary layers (Løseth et al., 2003). The cloudy appearance within the strata above the cone sheet is thought to indicate low levels of hydrocarbon gas, a feature commonly observed in seismic data within oil-rich basins and often associated with shale or salt diapirs.

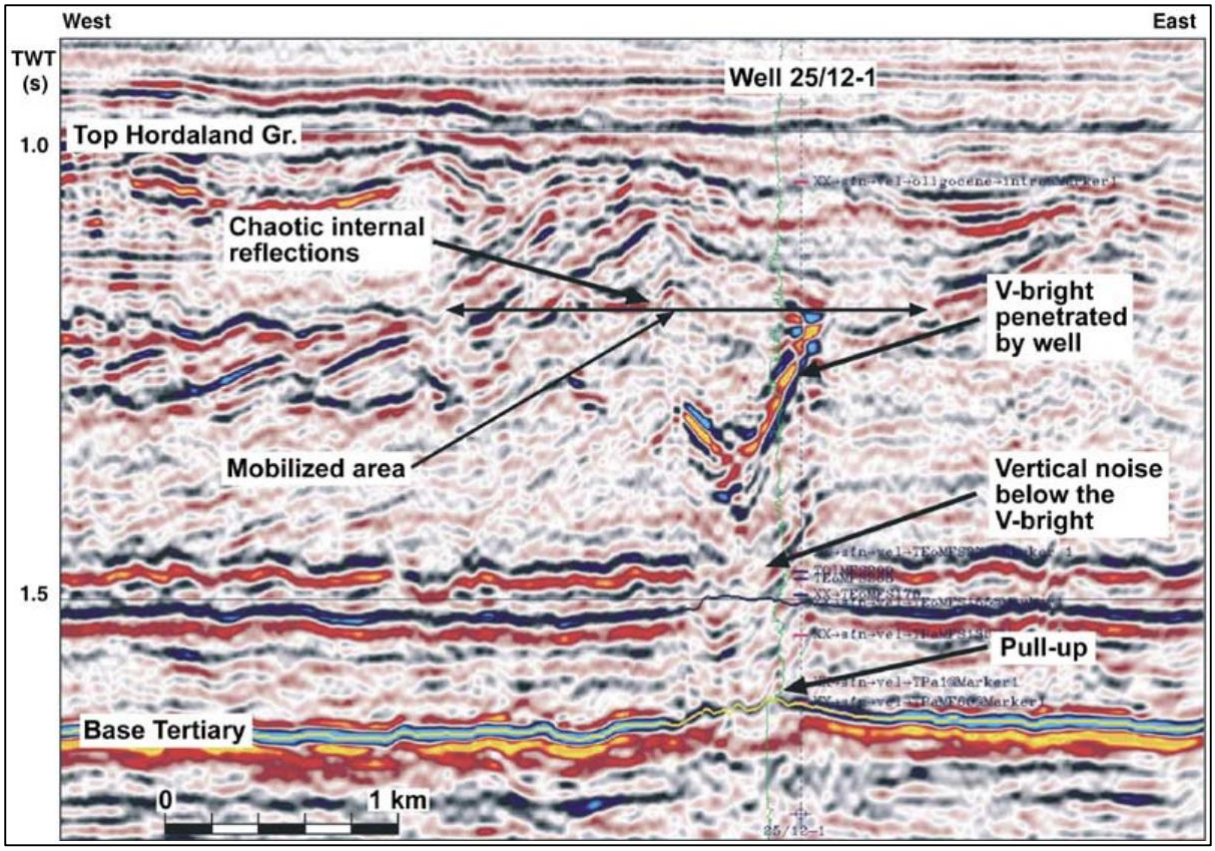

Figure 17: Seismic section of a conical sandstone intrusion within the Hordaland Group (Eocene), intersected by a well confirming the existence of a sandstone layer approximately 40 m thick, with 20 m of it being cemented by carbonate. From Hurst et al. (2003)

5. Theoretical background

This chapter offers a concise overview of the theoretical framework and key concepts employed in this thesis. Section 5.1 delves into the fundamentals of seismic reflectivity and amplitude behaviour. Section 5.2 discusses the amplitude versus offset (AVO) technique, outlining its principles and the classification of anomalies, which are instrumental in inferring lithology and fluid content. Section 5.3 introduces the basics of seismic inversion, highlighting the specific inversion approach utilized in this thesis. Section 5.4 presents the theory of extended elastic impedance, detailing its application in predicting lithology and fluid properties through rock physics. Finally, Sections 5.5 and 5.6 explain the concept of spectral decomposition and tuning thickness and its role in examining thin rock intervals.

5.1 Distribution of seismic energy

In the process of seismic exploration, various seismic wave types travel through the Earth's subsurface and are reflected back toward receivers on the surface. When downward-traveling P-waves are reflected upwards, they emerge both as P- and S-waves at their deepest point of penetration (Stewart et al., 2003). The behaviour of P- and S-waves, as they propagate, is governed by two fundamental principles:

1) the non-symmetrical ray path as dictated by Snell's Law (Figure 18)

2) the sinusoidal variation in amplitude as a function of distance from the source, or offset, which is expressed by the Zoeppritz equations (for details see section 5.1.2. on Zoeppritz approximations) (Zoeppritz, 1919).

Snell's law provides the relationship between the angles of incidence, refraction (transmission), and reflection when waves strike a boundary between two distinct isotropic media:

$$\frac{sin\,\theta_1}{\alpha_1} = \frac{sin\,\emptyset_1}{\beta_1} = \frac{\sin\theta_2}{\alpha_2} = \frac{sin\,\emptyset_2}{\beta_2} \qquad (1)$$

where, θ_1, θ_2 =Angles of reflection and transmission for the P-wave, respectively,

$\emptyset_1$, $\emptyset_2$ = Angles of reflection and transmission for the S-wave, respectively,

α_1 and β_1 = Velocities of the P-wave and S-wave in the first medium, respectively,

α_2 and β_2 = Velocities of the P-wave and S-wave in the second medium, respectively.

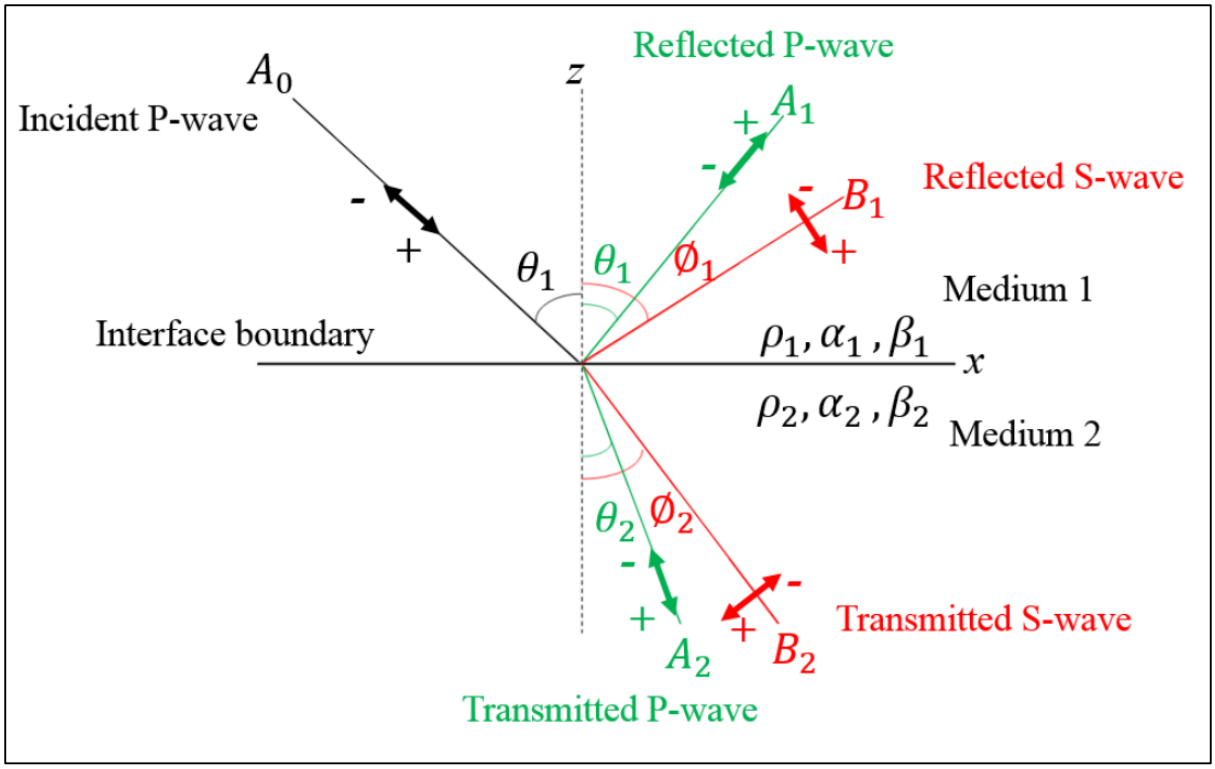

Figure 18: Diagram depicting the partitioning of seismic wave energy. An incident P-wave moves through a first medium with density (ρ1), P-wave velocity (α1), and S-wave velocity (β1). It encounters a second medium characterized by density (ρ2), P-wave velocity (α_2), and S-wave velocity (β_2). The angles θ_1 and θ_2 represent the reflected and transmitted angles for the P-wave, while $\emptyset_1$ and $\emptyset_2$ denote the reflected and transmitted angles for the S-wave, respectively. A_1 and A_2 indicate the amplitude magnitudes for the P-wave, and B_1 and B_2 are the amplitude magnitudes for the S-wave, concerning the reflected and transmitted energy. The negative and positive signs indicate the displacement directions. From Kausar (2018)

5.1.1 Seismic Amplitude Analysis

The basic interpretation of a seismic section, which is comprised of various reflections, is rooted in the differing densities and velocities of the rock layers. Understanding the reflection coefficient is foundational for various amplitude analysis methods such as inversion and AVO (Schroeder, 2017). With normal incidence and angle, the reflection coefficient can be described by the difference in acoustic impedance between two rock layers:

$$R_{(t)} = \frac{AI_{(t+1)} - AI_{(t)}}{AI_{(t+1)} + AI_{(t)}} \quad (2)$$

where, $AI_{(t)}$ and $AI_{(t+1)}$ represent the acoustic impedance of two rock layers. Consequently, the reflection coefficient is influenced by variations in acoustic impedance. This relationship is valid only for the zero-offset scenario (Figure 19). For cases where the offset is non-zero, the amplitude of the reflected wave depends on the angle of incidence (θ), density, and velocities (Schroeder, 2017).

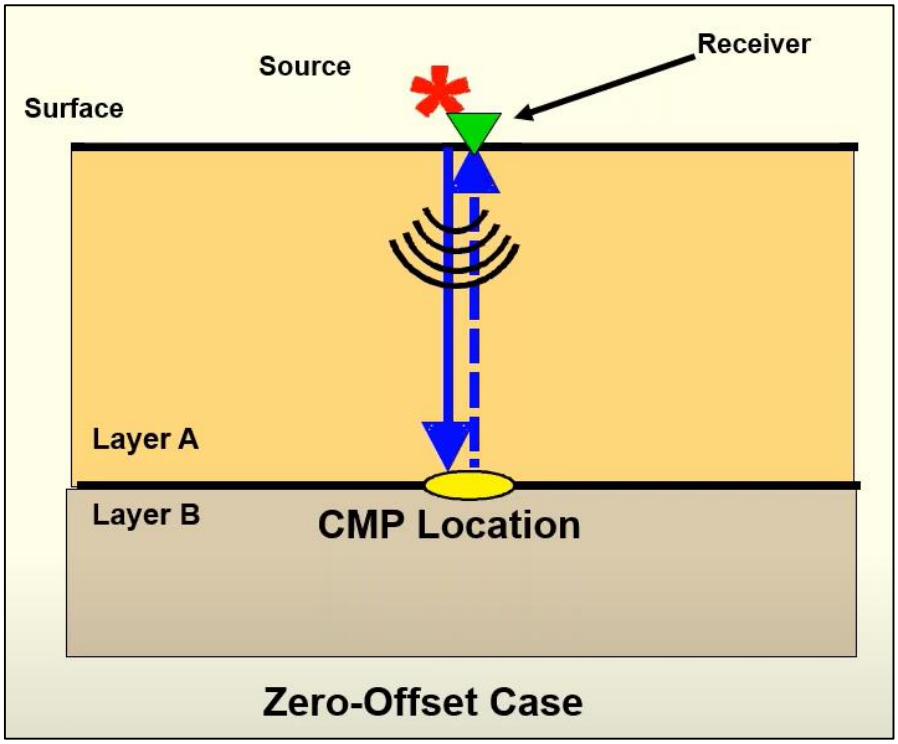

Figure 19: Reflectivity behaviour in the Zero-Offset scenario, with CMP denoting Common Mid-Point. From Schroeder (2017)

Taking a scenario where the distance between the source and receiver is greater than zero, the wave energy travels down to the boundary between two horizontal rock layers, A and B. According to Snell's Law (Slawinski et al., 2000), the angle of incidence will be equivalent to the angle of reflection (Figure 20). The reflectivity in this case will be governed by the Zoeppritz equations.

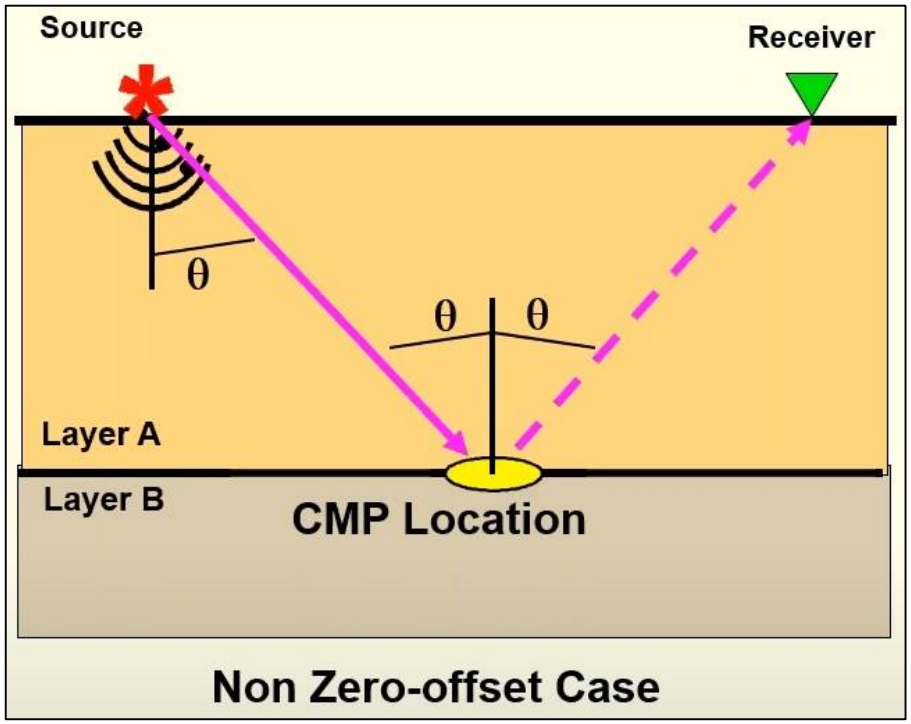

Figure 20: Reflectivity characteristics when encountering the Non Zero-Offset condition, with θ representing the angle of incidence. From Schroeder (2017)

5.1.2 Zoeppritz approximations

The Zoeppritz equations are a widely known set of formulas that describe the distribution of seismic energy at the interface between two rock layers. These equations establish a relationship between the amplitude of incident plane waves at a planar boundary separating two isotropic media and the amplitude of the resulting reflected and refracted P- and S-waves based on the angle of incidence (Sheriff & Geldart, 1995). They serve as a critical basis for evaluating how the amplitude of a seismic wave returning to the surface is affected by changes in the angle of incidence. This is the essence of the amplitude versus offset (AVO) analysis, a valuable method for identifying potential petroleum reservoirs.

However, the Zoeppritz equations are computationally complex and do not offer a straightforward understanding of how changes in rock properties affect reflection amplitudes (Resnick et al., 1986). Consequently, various authors have developed linear approximations that simplify this analysis (Figure 21).

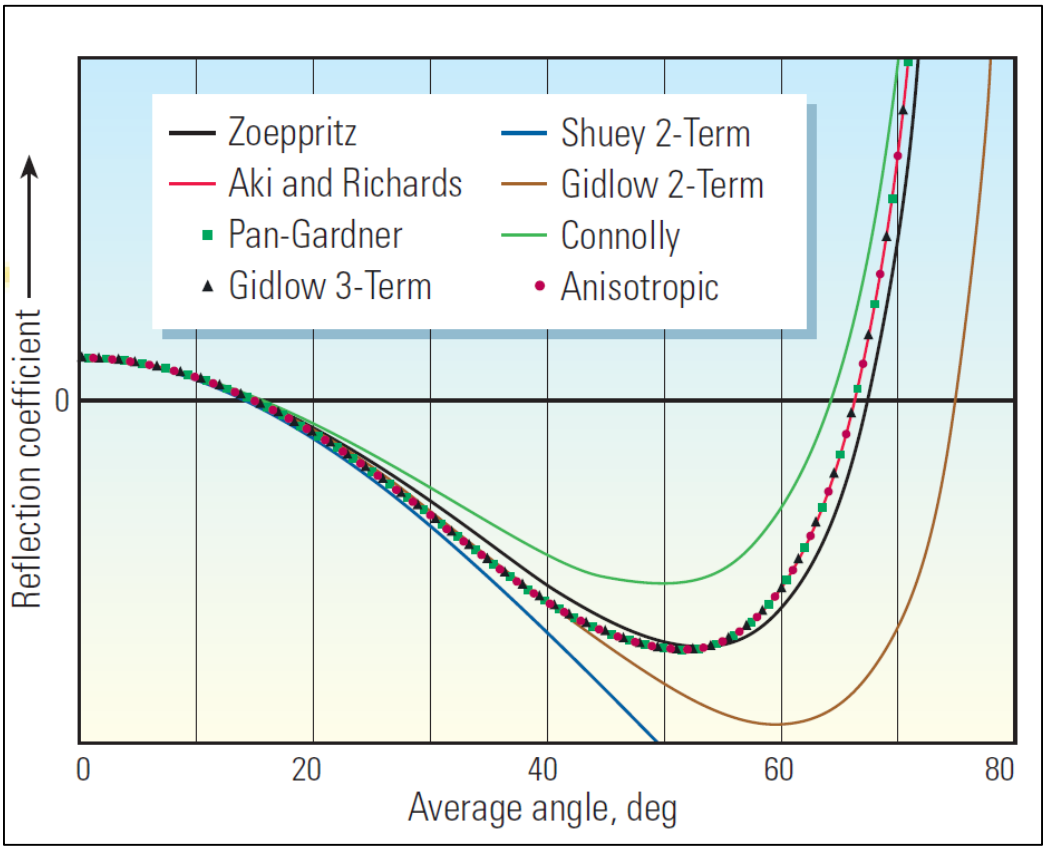

Figure 21: Comparison plot of various approximations of the Zoeppritz equations. The original equation is the black line. From Barclay et al. (2008)

An example of these simplifications is the Shuey 2-term approximation, which provides a relatively straightforward equation and yields a reasonably accurate portrayal of reflectivity for incident angles up to approximately 35° (Shuey, 1985):

$$R(\theta) = R_0 + \left[A_0 R_0 + \frac{\Delta\nu}{(1-\nu)^2}\right] sin^2\theta + \frac{1}{2}\frac{\Delta V_p}{V_p}(tan^2\theta - sin^2\theta) \qquad (3)$$

Ultimately, various authors have refined these equations into more comprehensible forms, and one notable example is Hilterman's modification of the Shuey equation (Hilterman, 1989):

$$R(\theta) = R_0 cos^2\theta + 2.25\Delta\nu sin^2\theta \quad (4)$$

where θ is the angle of incidence, and R_0 is the reflectivity coefficient at zero offset. The normal incidence reflectivity coefficient at zero offset (R_0) is defined as:

$$R_{0\ (normal\ incidence\ RC)} = \frac{\Delta AI}{AI_2 + AI_1} \quad (5)$$

The gradient of acoustic impedance is defined by the following formula:

$$\Delta AI = AI_2 - AI_1 \quad (6)$$

Acoustic impedance on its own is calculated from the product of bulk density and P-wave velocity:

$$AI_{(acoustic\ impedance)} = \rho * V_p \quad (7)$$

where ρ is the bulk density, and V_p is the P-wave velocity. The Poisson's ratio (ν) is given by:

$$\Delta\nu = \nu_2 - \nu_1 \quad (8)$$

$$\nu = [0.5 - \left(\frac{V_s}{V_p}\right)^2]/[1 - \left(\frac{V_s}{V_p}\right)^2] \quad (9)$$

where V_s is the S-wave velocity.

5.2 Amplitude versus offset analysis

During the seismic processing phase, it is possible to obtain seismic reflections from all offsets, this is known as a full stack, or to select specific offsets to form partial stacks. In the oil and gas industry, subsurface exploration teams often derive near-angle and far-angle stack seismic data in addition to full stack data for the purpose of analysing hydrocarbon signatures (Schroeder, 2017). Observing the variations in reflectivity amplitude between near and far stack seismic data can be indicative of the type of fluids present in the reservoir pore spaces of reservoir rocks and assist in differentiating certain rock types (Øygarden et al., 2015). The practice of Amplitude Versus Offset (AVO) is utilized to investigate such differences in seismic amplitudes. The reflection amplitude changes with the angle of incidence, θ, and is influenced by the physical properties on either side of the interface between two layers, including (Schroeder, 2017):

- The rock or lithological properties.

- The characteristics of the fluids in the rock's pore spaces.

A straightforward example of amplitude variation with offset is comparing amplitudes across near and far offsets at the top of the reservoir (Figure 22). Progressing from the geophone closest to the source (the near stack) to the farthest one, the highlighted interval marked by a red line, which represents a trough, indicates a negative reflection. In the case of hydrocarbon-filled pore space this negative amplitude becomes more negative when moving from the near

to the far stack or as the angle of incidence increases. Consequently, the amplitude can be plotted, and given that it represents a trough, the values are negative and become increasingly negative with greater angles or offsets. A linear fit can be applied to these reflection amplitudes, which allows for the derivation of both the intercept and the slope of the line (Schroeder, 2017). In the example provided (Figure 22), the result would show a negative intercept as well as a negative slope, also known as the gradient.

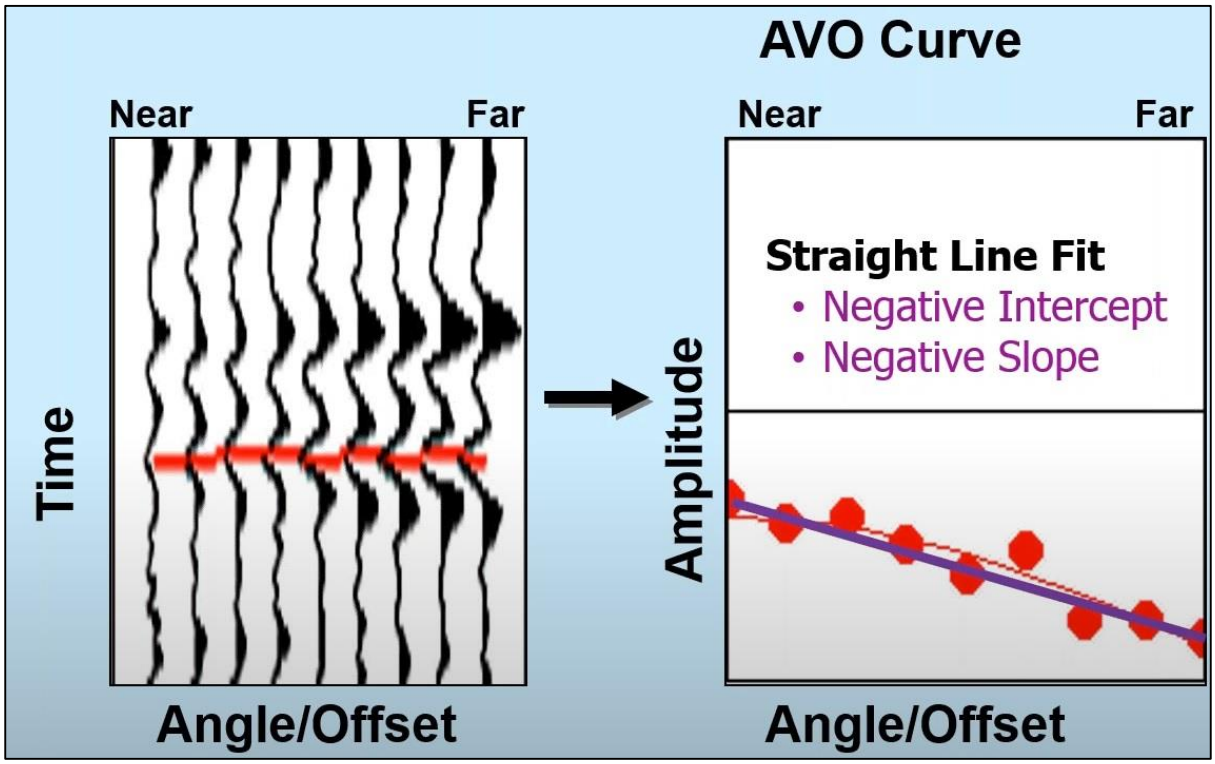

Figure 22: Figure 22: Amplitude variation with offset in a case at the top of the reservoir, along with a graph plotting the respective amplitudes against the angle or offset. From Schroeder (2017)

The subsequent step in AVO analysis involves taking the amplitude as a function of offset, which has been reduced to a linear equation, and plotting the corresponding intercept and gradient values as the AVO intercept (A) and AVO gradient (B) (Figure 23). Typically, the AVO response of shales tends to form a diagonal line, whereas water-saturated sands deviate farther from the shale reference line, and sands containing oil and gas diverge even more from this line (Schroeder, 2017). By evaluating the distance of a particular amplitude response from the shale baseline, it is possible to infer the type of fluid present within a reservoir. The AVO response, therefore, can be quantified using two parameters (Castagna et al., 1998):

- Intercept (A) – where the curve intersects the y-axis, corresponding to a 0º angle of incidence.

- Slope (B) – a linear fit applied to the AVO data, representing the rate of change in amplitude with offset.

Once the data points have been plotted, they can be categorized according to the classification system detailed in chapter 5.2.1.

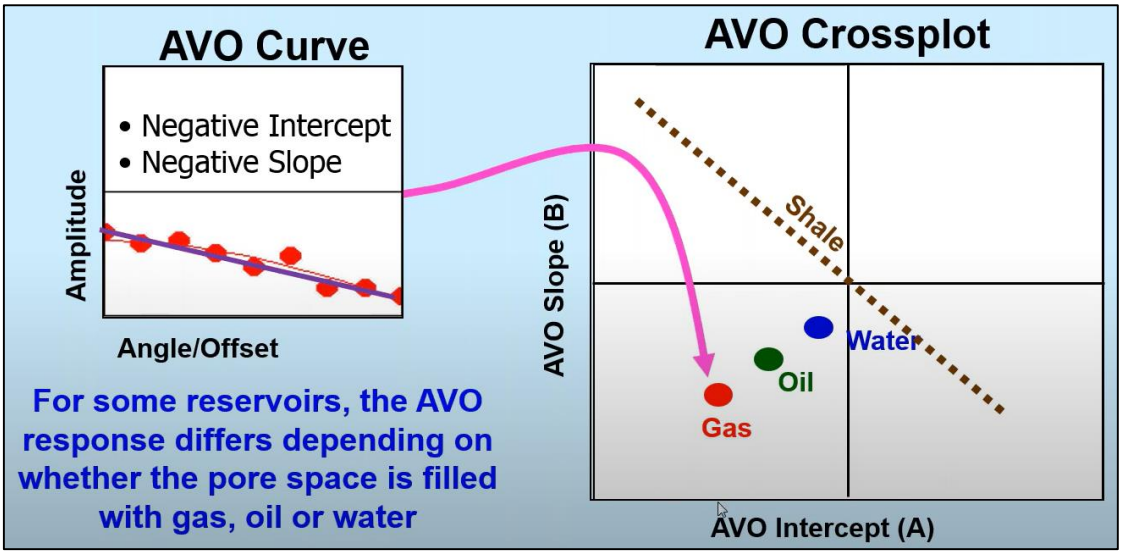

Figure 23: An illustration of how to graph amplitude against angle/offset and transform this data into an intercept/gradient (slope) plot. From Schroeder (2017)

Following the observation of various AVO responses, essential questions emerge (Schroeder, 2017):

- What characterizes the AVO response of brine-saturated sand?

- What is the AVO response of an oil-saturated sand?

- What is the typical AVO response of a gas-saturated sand?

- Can these responses be differentiated?

Distinguishable fluid responses can be achieved by conducting fluid substitution experiments within the reservoir strata, encompassing gas, oil, and brine (Goodway et al., 1997). This can be done utilizing distinct fluid property logs - for brine, oil and gas. With access to relevant well data, the model can be calibrated using data from a nearby or analogous well (Figure 24).

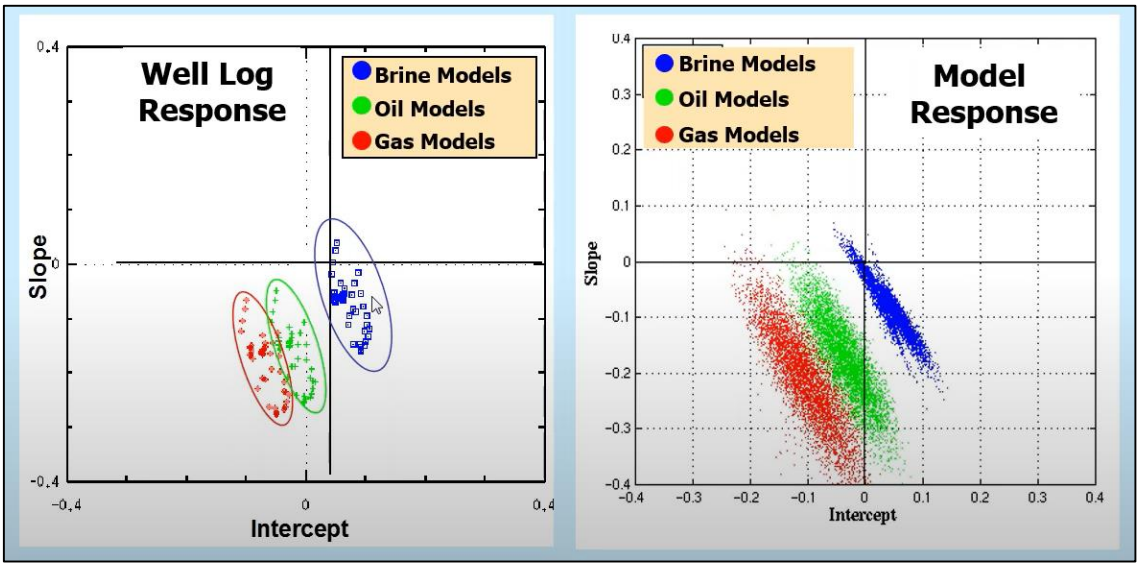

Figure 24: Calibration of the Amplitude Versus Offset (AVO) model using data from a proximal well. From Schroeder (2017)

5.2.1 AVO classes

Rutherford and Williams (1989) categorized gas-sand reflectors based on their AVO attributes into three distinct classes, which are determined by the reflection coefficient at zero incidence ($R_{(0)}$, intercept) at the top of the gas sand layer and its gradient. Figure 25 shows this relationship schematically for the gas reservoir top and different impedance contrasts between reservoir sand and overlaying shale. Class I includes sands with high impedance, Class II and IIp feature sands with near-zero impedance contrast, and Class III encompasses sands with low impedance. Later, Castagna et al. (1998) introduced an additional category, Class IV, characterized by an initially negative reflection coefficient that increases, approaching zero in magnitude as the offset increases (Figure 25). According to the classifications by Rutherford and Williams (1989), reflections at the base of a gas sand typically plot above the background trend line (representing brine-saturated sandstones and shales) on a cross-plot of AVO intercept (A) and gradient (B), while the reflections at the top of a gas sand generally appear below this line (Castagna et al., 1998) (Figure 25).

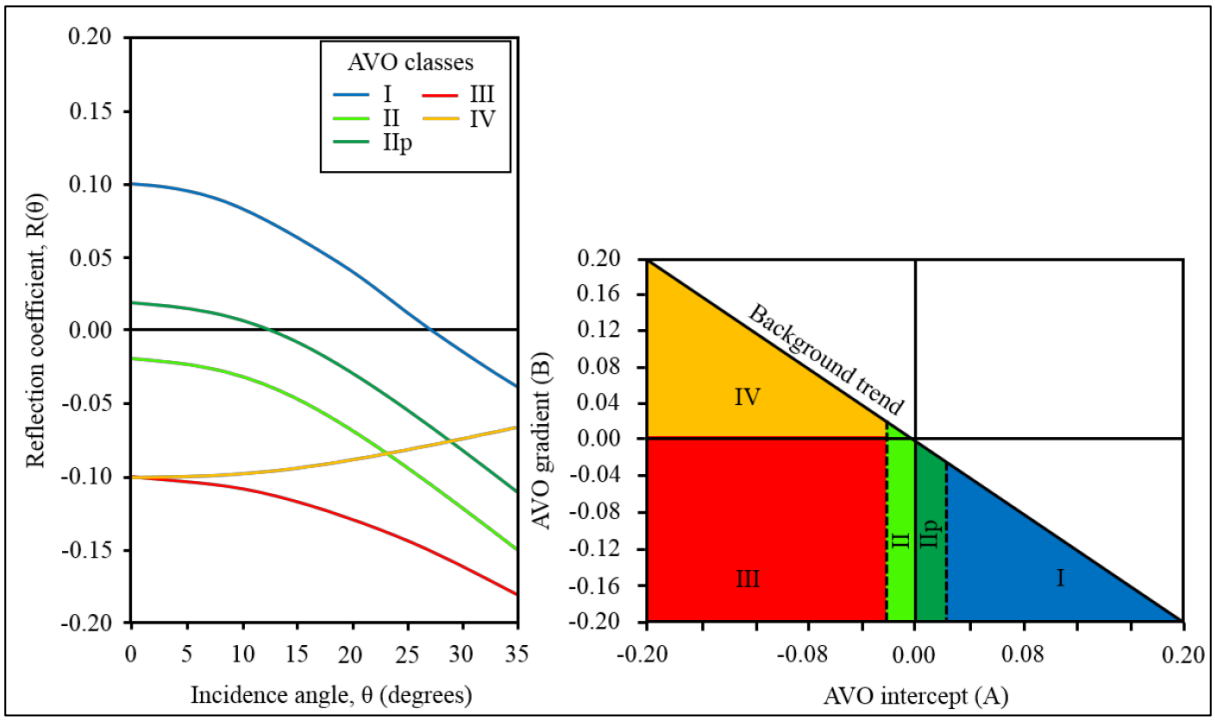

Figure 25: AVO classification. a) Reflection coefficients as a function of incidence angle at the gas sand top showing the different classes defined by Rutherford and Williams (1989). b) AVO intercept (A) versus gradient (B) cross-plot showing the same gas sand classes. Top of gas sand reflections tends to plot below the background trend (brine-saturated sandstones and shales). From Frette (2018)

5.3 Seismic inversion

Seismic inversion is the process by which seismic reflectivity data is transformed into a layered model of rock properties. This is accomplished by integrating well log information with seismic reflection data to shift the focus from reflectivity at major geological boundaries to the prediction of rock properties throughout an interval (Barclay et al., 2008). Figure 26 illustrates the traditional methods of seismic inversion, though there have been more recent advancements

that expand this classification. The depicted classification shows the inversion techniques commonly employed to estimate subsurface properties using seismic and well log data (Maurya et al., 2020).

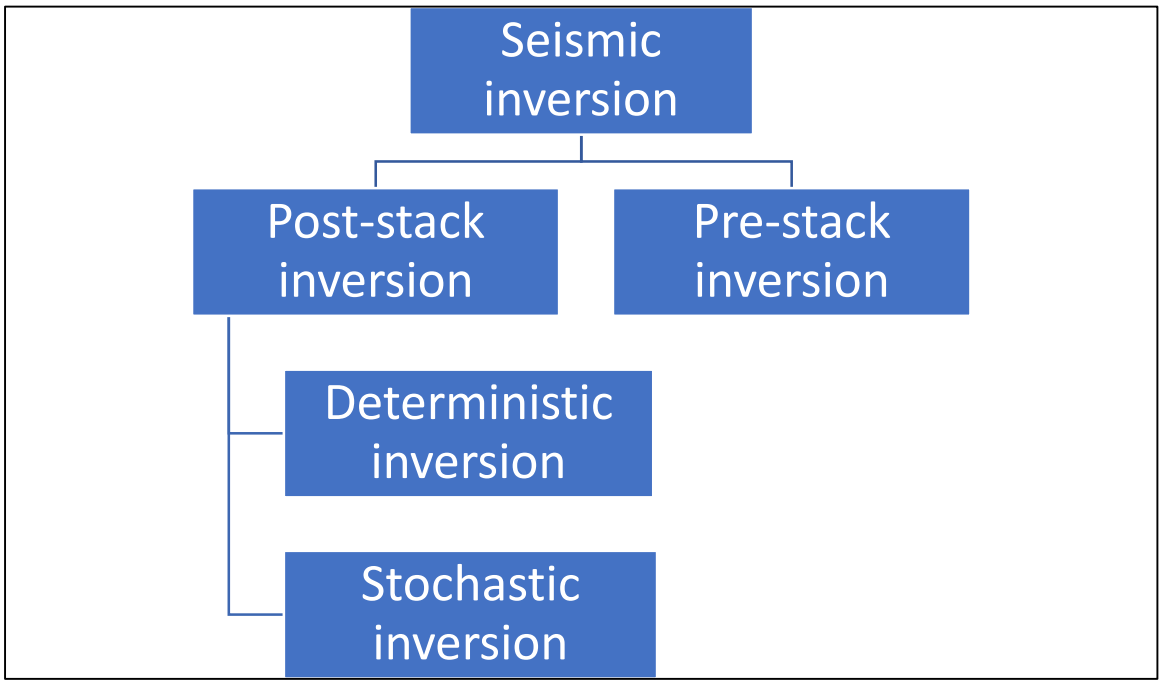

Figure 26: Classification of seismic inversion methods. Modified after Maurya et al. (2020)

Seismic inversion is the inverse process of forward modelling, where the aim is to simulate seismic signals from acoustic impedance (Figure 27) (Barclay et al., 2008). Seismic inversion can be categorized into two distinct approaches:

Acoustic Impedance Conversion: The first method involves transforming the seismic trace into a measure of acoustic impedance. An instance of this is the Relative Acoustic Impedance seismic attribute. Due to the absence of low frequencies in seismic data, relative acoustic impedance cannot provide absolute values for acoustic impedance.

Model-Based Approach: The second method is founded on modeling techniques. Here, the low-frequency component of the acoustic impedance is typically derived from well data, which is then extrapolated across the area of investigation. Subsequent steps involve systematically adjusting each impedance trace, computing the reflectivity, and convolving it with a wavelet that has been extracted from the seismic data (Gelderblom & Leguijt, 2010). By comparing these created synthetic traces with the actual seismic traces, the initial impedance traces undergo iterative modification until a satisfactory match is achieved between the synthetic and seismic traces.

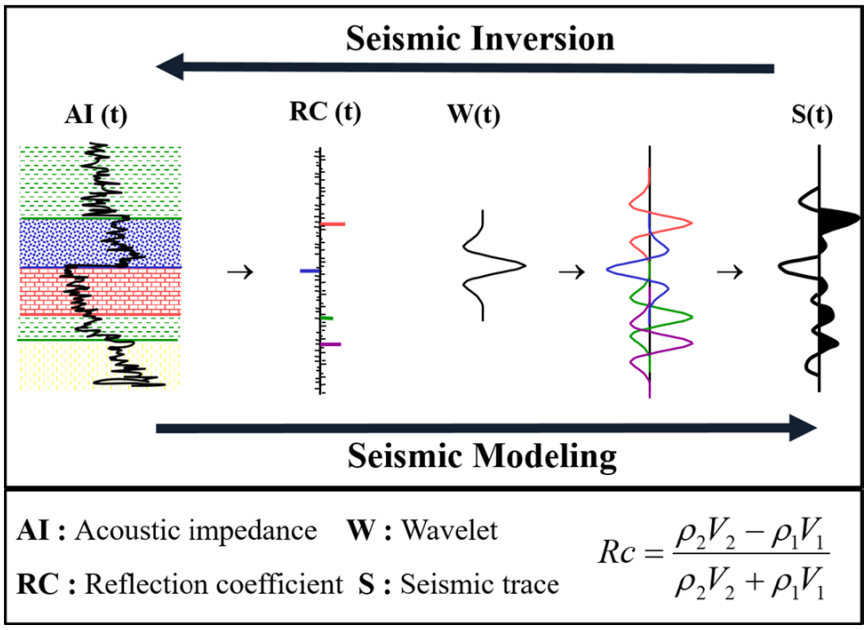

Figure 27: The seismic trace modelling to inversion and vice versa. From Bashir et al. (2024)

Most seismic images are produced using stacked data (Barclay et al., 2008). However, in the context of this research, where structures connected to remobilization exhibit strongly variable amplitudes with offset, inversion is conducted using unstacked traces — prestack inversion.

5.3.1 Pre-stack inversion

The stacking procedure often inadequately captures amplitude in certain situations. For example, when individual seismic traces exhibit amplitude variation with offset (AVO), then this information gets lost during the stacking. In such instances, it is preferable to apply inversion techniques to angle-stacked data, using modelled parameters that recognize and adjust for changes in amplitude, thereby refining the inversion output.

Pre-stack seismic inversion is beneficial for several reasons (Maurya et al., 2020):

1. It yields a higher resolution of subsurface geological layers by diminishing the influence of the wavelet, tuning effects, and sidelobes.

2. Therefore the derived acoustic impedance can be better correlated with well log data, which is closely associated with reservoir characteristics.

3. Pre-stack inversion provides the S-impedance next to the P-impedance and in the case of an available reliable ultra-large angle stack the density. These properties deliver additional insight that can help to differentiate between the impacts of lithology and fluid contents, offering a better understanding compared to other inversion approaches such as post-stack inversion.

5.4 Extended Elastic Impedance

The Extended Elastic Impedance (EEI) approach is a relatively recent methodology in the field of seismic exploration that has been utilized over the past several years. Initially introduced by Whitcombe (2002), its primary purpose is to facilitate the prediction of lithology and fluid characteristics by leveraging the Amplitude Versus Offset (AVO) attributes of seismic data. Elastic Impedance (EI) was originally proposed by Connolly (1999) as a generalization of acoustic impedance for non-normal angles of incidence:

$$EI\ (\theta)\ = V_p^{(1+sin^2\,\theta)} V_s^{(-8\mathrm{K}\ \sin^2\theta)} \rho^{(1\,-4K\ \sin^2\,\theta)} \tag{10}$$

where $K = (V_s/V_p)^2$.

Whitcombe (2002), introduced the extended elastic impedance concept, aimed at predicting fluid and lithology by analysing seismic data. This approach expanded upon the foundational research of Smith and Gidlow (1987), which emphasized the importance of prestack data. Subsequent work by Goodway et al. (1997) explored the utilization of the shear modulus, G, and Lame's constant, λ, for differentiating between lithologies and fluids. Whitcombe then refined the concept of elastic impedance (EI) by replacing $\sin^2\theta$ with $\tan\chi$ in the two-term reflectivity equation, allowing EI to extend across a comprehensive range of angles, from -90° to +90°. This essentially enabled the use of extended elastic impedance to interpret any combination of intercept and gradient values.

The initial step began with the application of Shuey's 2-term approximation:

$$R(\theta) = A + Bsin^2\theta \tag{11}$$

where A is the intercept and B is the gradient derived from the angle stacks or CMP gathers.

After that replace $\sin^2\theta$ with $\tan\chi$:

$$R(\theta) = A + Btan\,\chi \tag{12}$$

Dividing by $\cos\chi$:

$$R(\chi) = A\,cos\,\chi + B\,sin\,\chi \tag{13}$$

It can be shown (Whitcombe et al. 2002) that:

$$EEI\ = V_p^{(\cos\chi+\sin\chi)} V_s^{(-8\mathrm{K}\ \sin\chi)} \rho^{(\cos\chi-4K\ \sin\chi)} \tag{14}$$

EEI as a function of the angle χ can be expressed as:

$$EEI(\chi) = AI_0\ [\left(\frac{AI}{AI_0}\right)^{\cos(\chi)} \left(\frac{GI}{AI_0}\right)^{\sin(\chi)}] \tag{15}$$

where EEI is the Extended Elastic Impedance, AI_0 – Acoustic impedance at zero offset (θ=0). At $\chi = 0$ EEI corresponds to the Acoustic Impedance (AI), and EEI at $\chi = 90$ EEI aligns with the Gradient Impedance (GI) (Whitcombe et al., 2002).

This can be expressed more simply as a combination of AI and GI:

$$EEI(\chi) = AI^{cos\,(\chi)}\, GI^{sin\,(\chi)} \tag{16}$$

The gradient impedance, GI, can be defined as:

$$GI = V_p V_s^{-8K} \rho^{-4K} \tag{17}$$

The equation utilized for rotating in the log space is the Extended Elastic Impedance (EEI) at a specific χ angle:

$$\ln\big(EEI(\chi)\big) = \ln(AI) * \cos(\chi) + \ln(GI) * \sin(\chi) \tag{18}$$

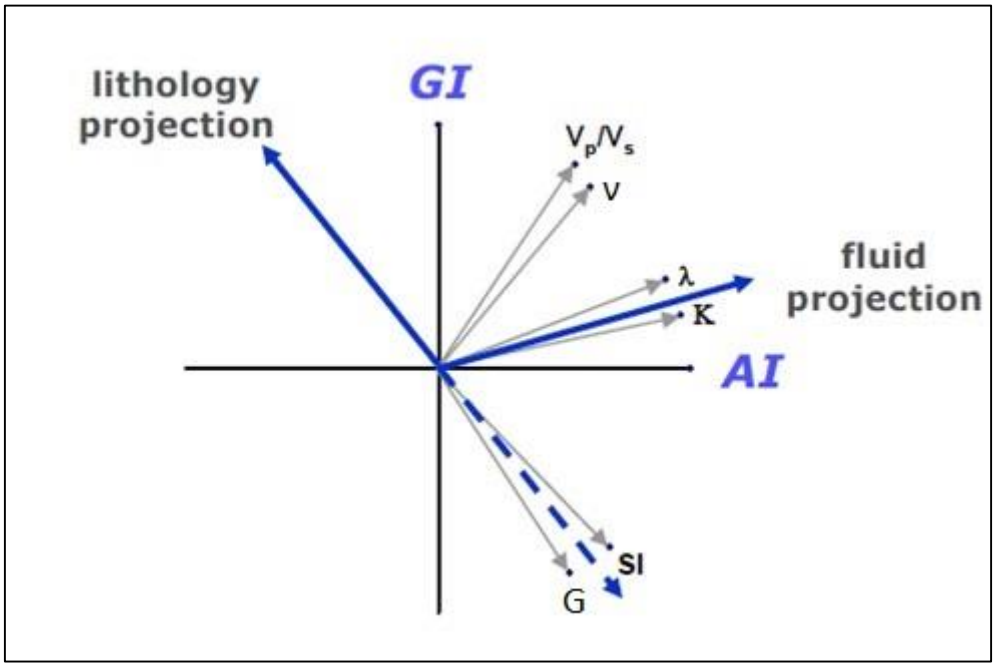

Figure 28: Cross plot of Acoustic Impedance/Gradient Impedance (AI/GI) displaying various rock physics attributes at distinct χ angles. v – Poisson's ratio, SI – shear impedance, K – bulk modulus, G – shear modulus, λ – Lame constant. The χ angle is extrapolated from the AI axis, with lithology projection, for instance, having a χ angle of approximately -45°. From Pranata et al. (2017).

EEI closely resembles conventional elastic impedance but is specifically designed to function with intercept/gradient crossplots in the ln-space. The acoustic impedance/gradient (AI/GI) cross plot serves as the foundational tool for emphasizing certain rock properties at a particular χ angle (Pranata et al., 2017). The EEI approach involves the rotation in the ln-space of AI and GI, (Figure 28) and gets for each rotation angle the ln(EEI(χ)). Then ln(EEI) is converted to EEI aiming to achieve the optimal correlation coefficient in relation to a particular geophysical log, such as those for water-saturation and gamma-ray (Figure 29). Hence, by examining the correlation coefficients, it can ascertain which chi (χ) angles provide the best understanding of changes related to fluids, such as water saturation (S_w), or changes related to lithology, such as those indicated by gamma-ray log (GR).

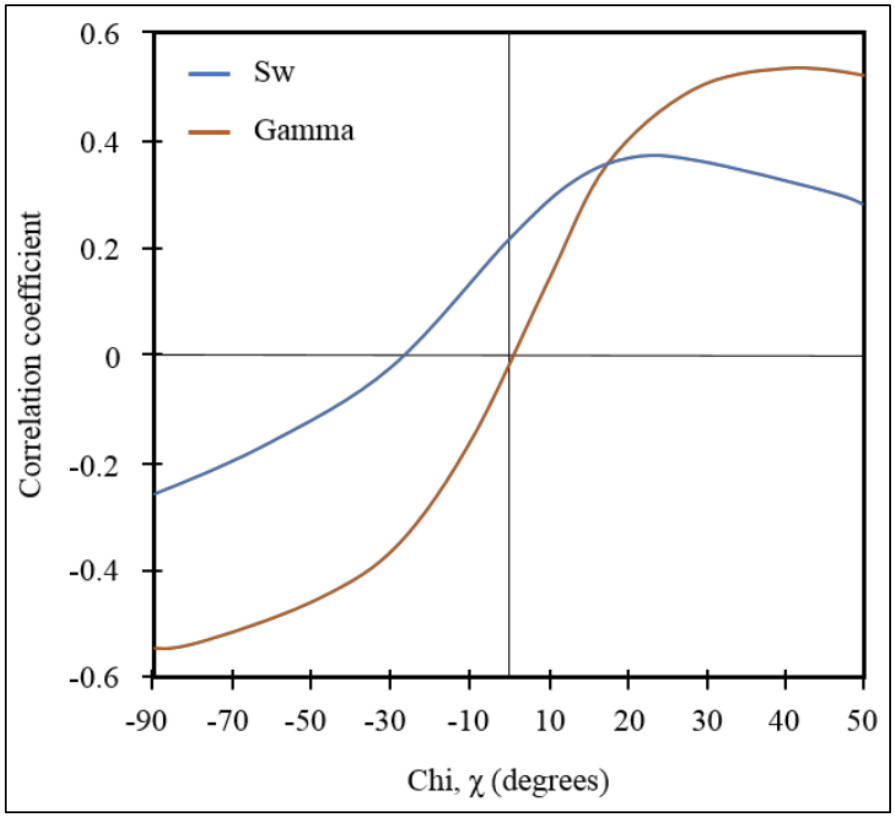

Figure 29: The correlation coefficient between Extended Elastic Impedance (EEI) and gamma-ray and water-saturation (Sw), across a range of chi (χ) values from -90 to 90°. From Frette (2018)

Different authors calculated different χ angles of various petrophysical parameters that can be derived, but overall, the angles stay in specific intervals and can slightly vary in different geological environments. The example below is from Ball et al. (2014) which illustrates the relative weightings of the intercept and gradient in terms of K (Figure 30). In essence, through the combination of varying weightings (W) of intercept and gradient, one can modify the orientation of the projection and subsequently infer diverse petrophysical properties.

	$W_{(int)}$	$W_{(grad)}$	chi			
			k=0.2	*k*=0.25	*k*=0.3	empirical
P-impedance	1	0	0	0	0	0
S-impedance	0.5	-1/8k	-51	-45	-40	-47
Mu-rho	1	-1/4k	-51	-45	-40	-48
K-rho	$\frac{2k-6}{4k-3}$	$\frac{-1}{4k-3}$	10	10	10	13 (K only)
Lambda-rho	$\frac{2k-2}{2k-1}$	$\frac{-1}{4k-2}$	17	18	20	22
E-rho	$\frac{4k^2-6k+6}{4k^2-7k+3}$	$\frac{-8k^2+16k-6}{8k(4k^2-7k+3)}$	-30	-24	-20	-
Poisson's ratio	$\frac{k}{2k^2-3k+1}$	$\frac{1}{8k^2-12k+4}$	51	45	40	51
Gradient	0	1	90	90	90	90

Figure 30: The relative weightings of the intercept and gradient in terms of k to optimize correlation with a range of elastic properties. The right-hand column shows the variation of the chi (χ) angle from the k parameter. From Connolly (2017).

For instance, setting the weighting for the intercept (W_{int}) to 1 and the weighting for gradient (W_{grad}) to 0 enables the extraction of P-impedance (which equates to the reflectivity at zero offset or the intercept at 0, controlled by impedance, as explained in section 5.1.2).

The key projections I am interested in are fluid (Lambda-Rho) and lithology projections (S-Impedance). The fluid projection highlights the effect of fluids and their saturation changes, reducing the effect of porosity changes. The lithology projection minimizes the effect of fluid changes and maximizes the effects of lithology and porosity changes (Pranata et al., 2017).

5.5 Seismic Tuning

The concept of seismic tuning is an essential principle in geophysics and is pivotal for interpreting thin injectite intervals on seismic data. Seismic tuning occurs due to the constructive interference of wave reflections at the boundaries between geological layers as their thickness diminishes. As the layers become thinner, the reflections from the top and bottom boundaries begin to overlap more to create constructive interference (Dowdell, 2020). At a specific thickness, this interference reaches its peak having maximum amplitude; this critical point is referred to as the Seismic Tuning Thickness. Below this threshold, the reflections from the top and bottom boundaries cannot longer be individually distinguished. Widess (1973) published the landmark paper, "How thin is a thin bed?", which was instrumental in clarifying misunderstandings regarding the resolution of thin beds. He analysed two identical seismic wavelets separated by a specific time interval, which corresponds to the bed thickness in terms of Two-Way Travel Time (TWT). These wavelets serve as analogues for reflections from a layer's top and base. The study led to several key definitions related to seismic tuning:

Onset of Tuning thickness in the depth domain:

$$\lambda_{tuning\ onset} = \lambda/2 \tag{19}$$

Tuning thickness in the depth domain:

$$\lambda_{tuning} = \lambda/4 \tag{20}$$

Limit of resolution in the depth domain:

$$\lambda_{limit} = \lambda/8 \tag{21}$$

where λ represents the wavelength in the depth domain associated with the layer's predominant frequency. The fundamental relationship connecting velocity, frequency, and wavelength:

$$\upsilon = f * \lambda \tag{22}$$

where υ – seismic wave velocity (m or ft/sec), f - frequency (Hertz or cycles/sec), and λ - the wavelength (in m or ft). This relationship is frequently restated as follows:

$$\lambda = \frac{\upsilon}{f} \tag{23}$$

This reformulation is useful because, in the context of seismic studies, we often have an estimate of both the velocity and frequency within a zone of interest and seek to determine the corresponding wavelength (Dowdell, 2020). Once the wavelength is estimated, then it is possible to calculate various tuning parameters using the definitions provided by Widess

(1973). For instance, the tuning thickness in the depth domain can be calculated using the formula:

$$\lambda_{tuning} = \frac{v}{f}/4 \tag{24}$$

The tuning thickness can be calculated in the time domain (in TWT) using the equation:

$$T_{tuning} = \frac{T}{2} \tag{25}$$

where T represents the period and can be derived as:

$$T = \frac{1}{f} \tag{26}$$

Onset of Tuning thickness in the time domain:

$$T_{tuning\ onset} = T \tag{27}$$

Limit of resolution in the time domain:

$$T_{limit} = \frac{T}{4} \tag{28}$$

Therefore, the thicknesses corresponding to the tuning parameters in depth are given by:

$$\lambda_{onset} = v * T/2 \tag{29}$$

$$\lambda_{tuning} = v * (T/2)/2 \tag{30}$$

$$\lambda_{limit} = v * (T/4)/2 \tag{31}$$

One benefit of presenting the various tuning parameters in terms of Two-Way Travel Time (TWT) rather than depth measurements is that this approach requires only an understanding of the layer's dominant frequency (Dowdell, 2020). For instance, if a pair of reflective layers has a dominant frequency of 25 Hz, then the corresponding TWT tuning thickness can be expressed as follows:

$$T_{tuning} = \frac{T}{2} = (1\ /\ f\ )\ /\ 2 \tag{32}$$

$$= (\ 1\ /\ 25\ Hz\ )\ /\ 2$$

$$= 20\ ms\ TWT$$

If the layer's velocity is known, which can be determined from well log data or a seismic velocity model, for example, 3,000 m/s, then the corresponding tuning thickness in meters is calculated as:

$$\lambda_{tuning} = v * (T/2)/\ 2 \tag{33}$$

$$= 3000\ m/s\ * 20\ ms\ TWT/2$$

$$= 3000\ m/s * 0.020\ s\ TWT/2$$

$$= 30\ m$$

5.5.1 Seismic tuning wedge model

With the principles of seismic tuning established, the Seismic Tuning Wedge Model brings a very practical application to this problem. This model is a straightforward three-layer forward modelling structure where the top and bottom layers are generally identical, while the intermediate wedge layer tends to emulate the target stratum (Figure 31). In other words, the encasing layers are often representative of shale, while the wedge layer models a sandstone (Dowdell, 2020). The wedge layer's thickness is assigned a value significantly greater than the tuning level at one end of the model, and it tapers to a zero thickness at the opposite end. The precise measurements of the top and bottom layers are less critical, as the focus is on the reflections produced at the interfaces bounding the wedge top and base layer.

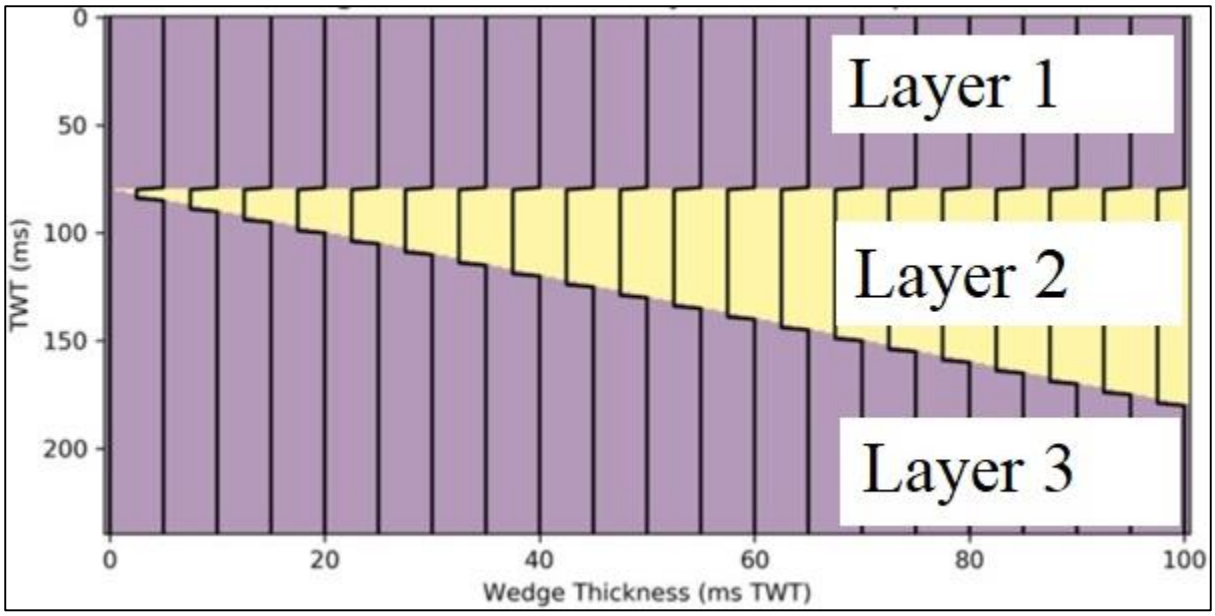

Figure 31: An illustration of the wedge model wherein the layers are differentiated by their Acoustic Impedance (AI). The model is comprised of three distinct strata, with both the top and bottom layers having identical AI. The central layer, shaped as a wedge, reaches its maximum thickness at one end while progressively narrowing down to a negligible, zero thickness at the opposing side. Modified after Dowdell (2020)

With a contrast in Acoustic Impedance (AI) between the wedge and the adjacent layers, a Ricker wavelet can be applied to the model (Dowdell, 2020). This convolution produces a synthetic seismic wedge representation (Figure 32).

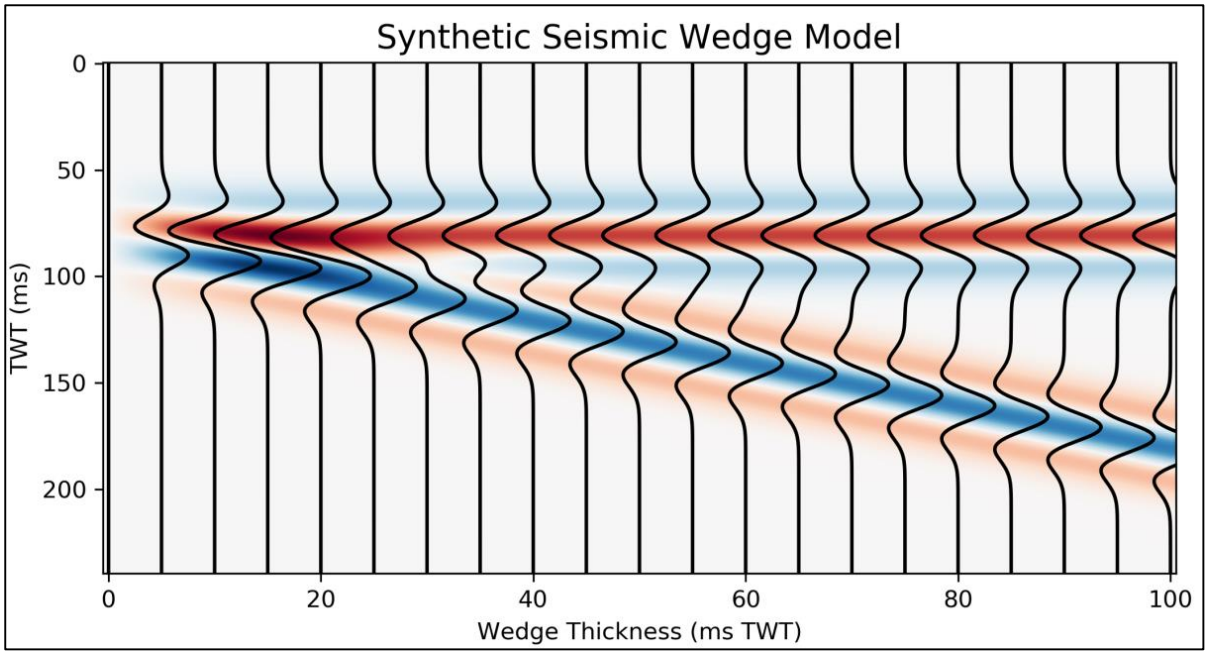

Figure 32: A synthetic seismic wedge model derived by convolving the reflectivity data of the wedge model with a Ricker wavelet. The plot displays every fifth trace. A decrease in impedance is represented by red while an increase is represented by blue. From Dowdell (2020)

By extracting the amplitude values along the top of the wedge, it is possible to construct a graph known as the Tuning Curve (Dowdell, 2020) (Figure 33).

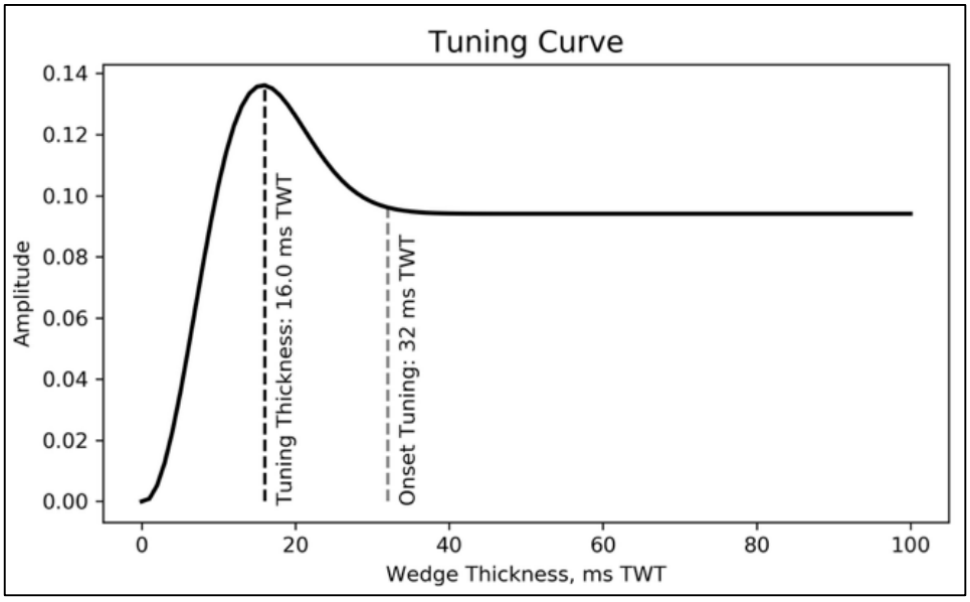

Figure 33: The Tuning Curve, which has been extracted from the upper boundary of the wedge at the interface of Layers 1 and 2. From Dowdell (2020)

The tuning curve provides valuable insight into the influence of layer thickness on reflection amplitude. Initially, when the wedge significantly exceeds the tuning thickness, the amplitude at the top interface remains constant (Dowdell, 2020). As the wedge thins to a certain thickness, noted as $\lambda/2$ or T_{onset}, the tuning curve starts to rise due to the constructive interference between reflections from the wedge's top and bottom boundaries. As the wedge continues to thin, the

constructive interference increases until it reaches its apex at a thickness of λ/4 in the depth domain or T/2 in the TWT domain (Widess, 1973). This point represents the Tuning Thickness, which is the minimum thickness at which a seismic survey can still differentiate between the top and bottom of a layer. If the wedge is thinned beyond the tuning point, destructive interference will occur, and the tuning curve will diminish. Should a layer be thinner than the tuning thickness, its top and base reflections may no longer be resolvable, precluding the direct estimation of layer thickness from seismic mapping (Widess, 1973).

5.6 Spectral Decomposition

Spectral decomposition is a technique for examining seismic data that involves disassembling seismic signals into component frequencies. This approach converts seismic information from the time domain to the frequency domain, enabling the use of various tuning frequencies chosen to emphasize layers of specific thickness (Partyka et al., 1999). Therefore, the motivation for employing spectral decomposition lies in the issue of thin-bed tuning and variations in bed thickness as in the case of remobilized sand, where the strata have thicknesses less than one-quarter the seismic wavelength (Chopra & Marfurt, 2016; Li et al., 2015). Strata that are thinner than this threshold can go undetected (Kenneth Samuel & Righteous, 2019).

As a result, this technique employs a series of band-pass filtered seismic cubes across a targeted area to produce a collection of amplitude maps at certain frequency bands. In spectral decomposition, individual frequency bands can be visually presented using distinct colours and blending tool (Figure 34). The RGB colour model is the most employed scheme, where three specific frequencies are represented by the colours red, green, and blue, respectively (Han, 2018). A white colormap suggests that the three analysed volumes exhibit strong hight amplitude simultaneously; meanwhile, dominant values of a particular volume will vividly display its designated colour (Li et al., 2015). In contrast, black presents no amplitudes for all three frequency ranges. The selection of specific frequencies, such as the range of 7-50 Hz used in this study, plays a critical role in effectively revealing the diverse geological formations. These were adjusted using the cross plot of tuning frequencies (section 6.2) to optimize the visualization of the geological features within each seismic unit.

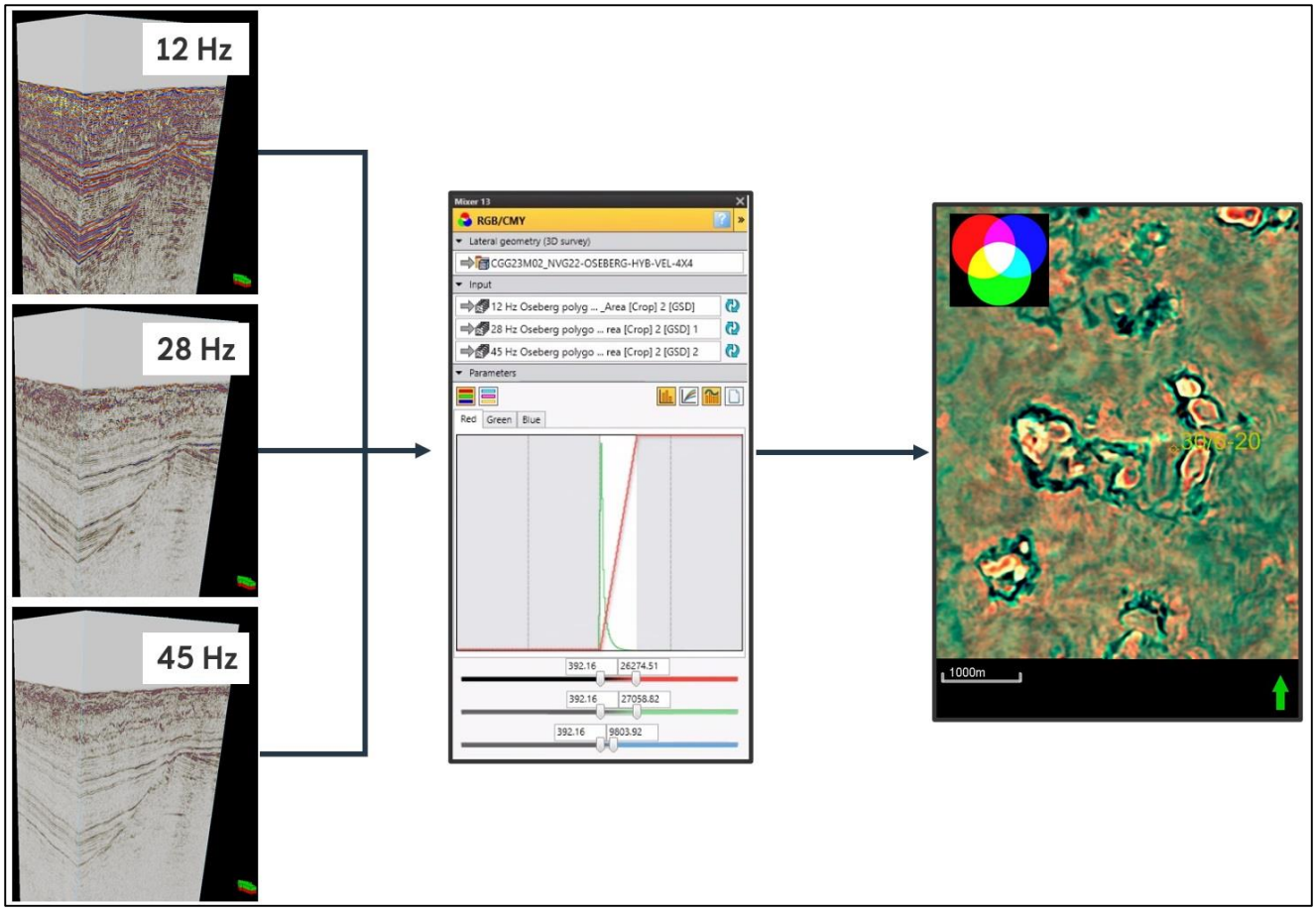

Figure 34: General workflow of Generalized Spectral Decomposition Colour Blending. The cubes are assigned to colours: 12 Hz – red, 28 Hz – Green, and 45 Hz – Blue.

The correlation algorithm is a technique utilized within Generalized Spectral Decomposition. Correlation, as a metric, evaluates the degree of similarity. This method initially computes the correlation between a constructed wavelength of a specific narrow frequency range and every individual trace from the provided input seismic data. It keeps only the positive correlations while removing any negative ones. Subsequently, for each cube correlated with a wavelet of a specific frequency band, the algorithm allocates the positive portion of the correlation function within a gliding window.

Spectral decomposition is highly effective at highlighting particular geological features. For instance, when relying solely on vertical sections of seismic reflectivity data, interpreting the underlying geology can be quite challenging without this technique (Aarre, 2016) (Figure 35).

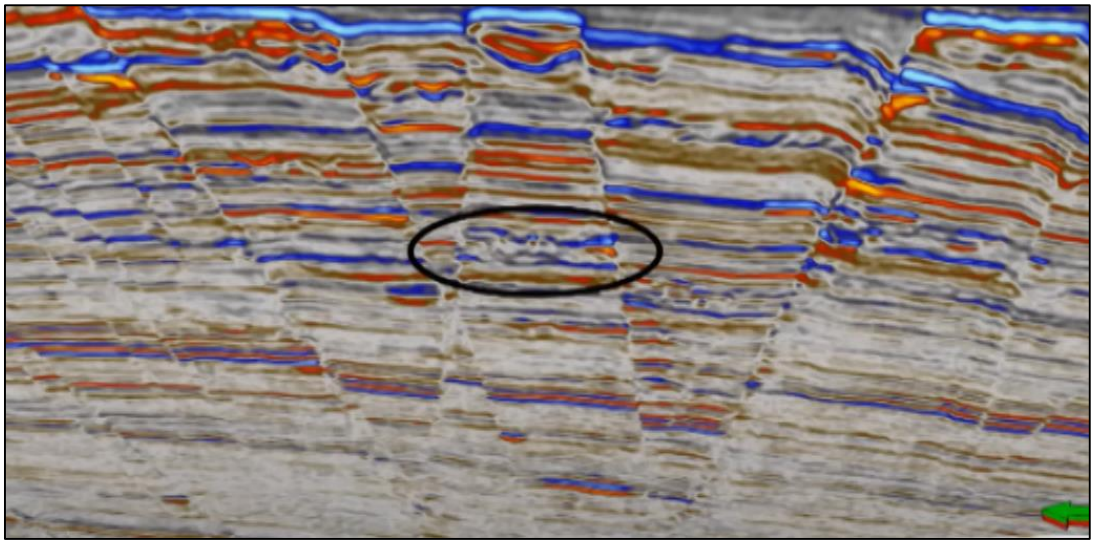

Figure 35: Seismic reflectivity section from the Barents Sea. The black circle highlights a meandering channel. From Aarre (2016)

However, by applying spectral decomposition to a time slice intersecting that section (Figure 36), one can suddenly discern features in the central area, such as a delta system and meandering channels bounded by faults (Aarre, 2016). Furthermore, the prominent blue coloration, which indicates a response at 40 Hz, suggests that the thickness of these layers is approximately 12 ms. This information is particularly valuable for geological interpretation.

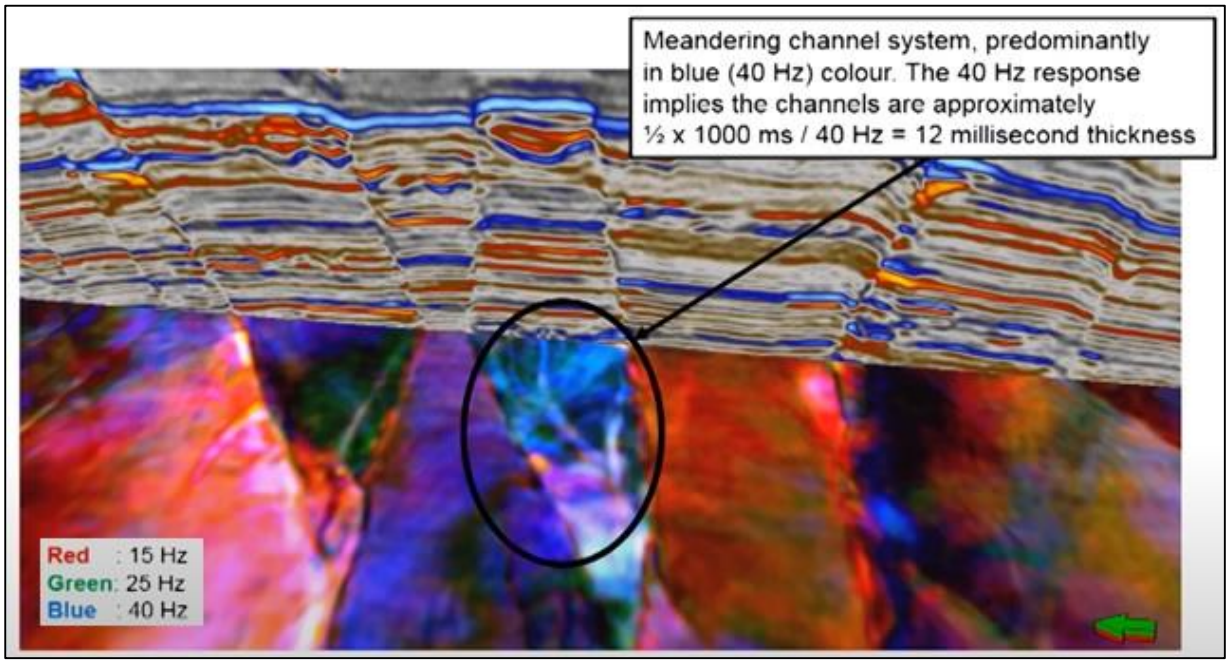

Figure 36: Implementation of Generalized Spectral Decomposition Color Blending technique to emphasize the channel system. Red is assigned to 15 Hz, green to 25 Hz, and blue to 40 Hz. From Aarre (2016)

The key objectives for applying spectral decomposition are:

- **Frequency Band Analysis for Optimal Imaging:** By breaking down the seismic signal into its main frequencies, we can analyse how sand injectites appear at different frequency bands. This approach enables the identification of which frequency bands most effectively

image the sand injectites. To determine the frequencies of interest for settled analysis, an amplitude spectrum of the seismic is produced.

- **Enhanced Layer Resolution:** Frequency dependency of the tuning thickness means that high-frequency components will allow for the resolution of thinner layers. This is particularly useful in the context of sand injectites, which have varying thicknesses along strike (sills). By decomposing the seismic signal into small frequency bands, it is possible to distinguish between thin layers more effectively. In our case, where the area of interest is around 1.2-2 s, using higher frequencies can indeed enhance the resolution and help in better identifying the finer details of these structures.

6. Methodology

This chapter provides a detailed description of the workflow used in this project. Each method has a different workflow, but in the end, the outputs from different methods are compared and integrated. The general methodology workflow is illustrated in Figure 37.

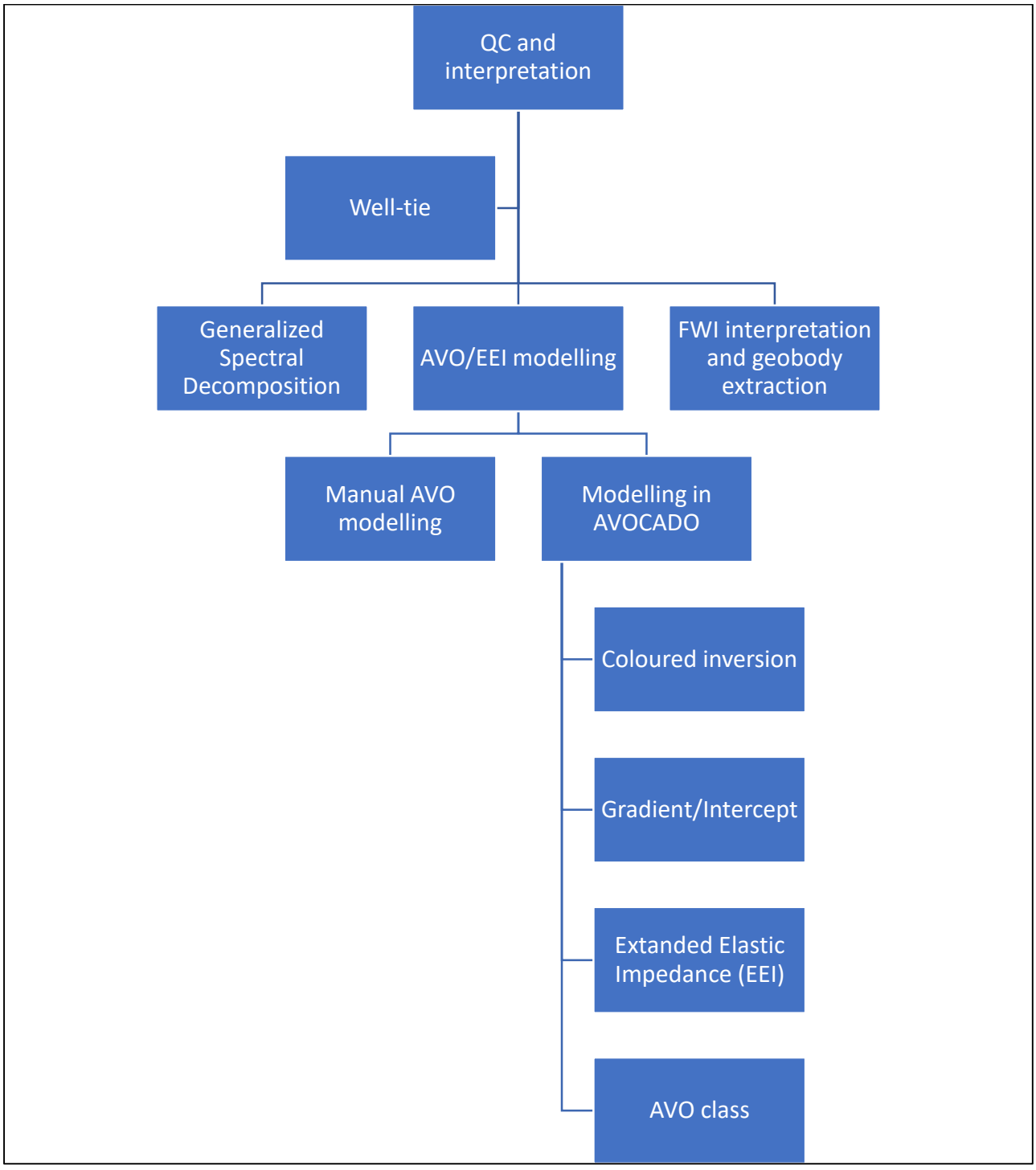

Figure 37: Schematic showing the workflow of the thesis.

6.1. Wavelet extraction and seismic to well tie

The seismic-to-well tie process is essential for correlating seismic horizons with stratigraphic layers by calculating a seismic response at the well using the synthetic trace derived from the

sonic and density logs and then comparing it to the seismic data. Well 30/6-20 was selected for this task, as it contains a compressional sonic log, a check-shot information, a density log, and numerous other valuable logs. Accomplishing the seismic-to-well tie involved creating a synthetic seismogram from the impedance log and an Ormsby wavelet. Figures 38 and 39 illustrate the well section with the acoustic impedance log, the synthetic trace, and the seismic sections for key horizons — specifically, the top of the Shetland and Hordaland Groups. These horizons are markedly pronounced in both the seismic and acoustic impedance logs as strong reflectors. To align the synthetic with the actual seismic data, a bulk shift of 19ms was applied to the synthetic trace (Figure 39).

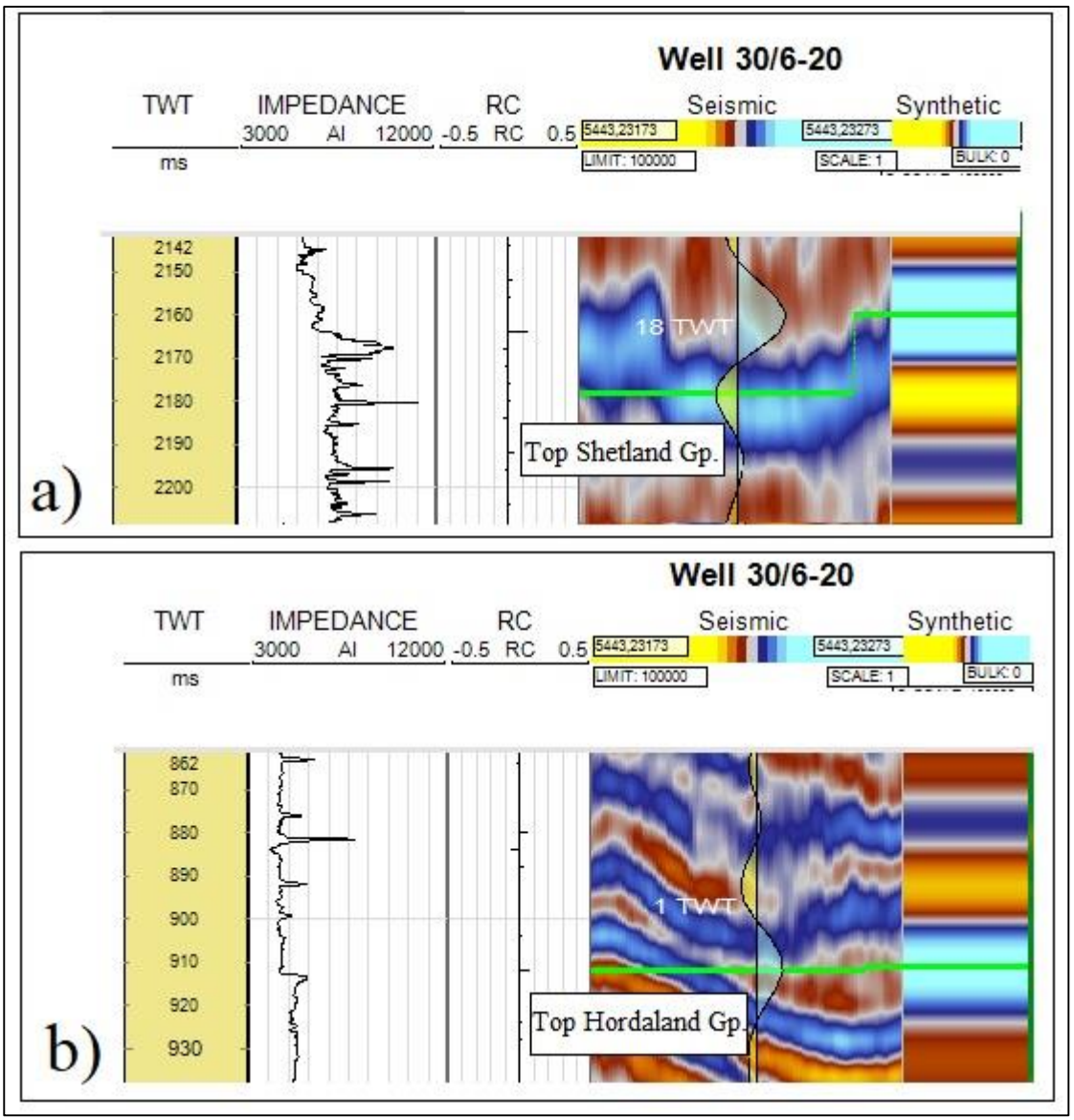

Figure 38: Seismic-to-well tie prior to implementing the bulk shift on the seismic section: a) Showing Top Shetland Gp. b) Showing Top Hordaland Gp. The acoustic impedance log and its corresponding reflectivity log are on the left. The near angle stack and the synthetic seismogram indicate a mismatch.

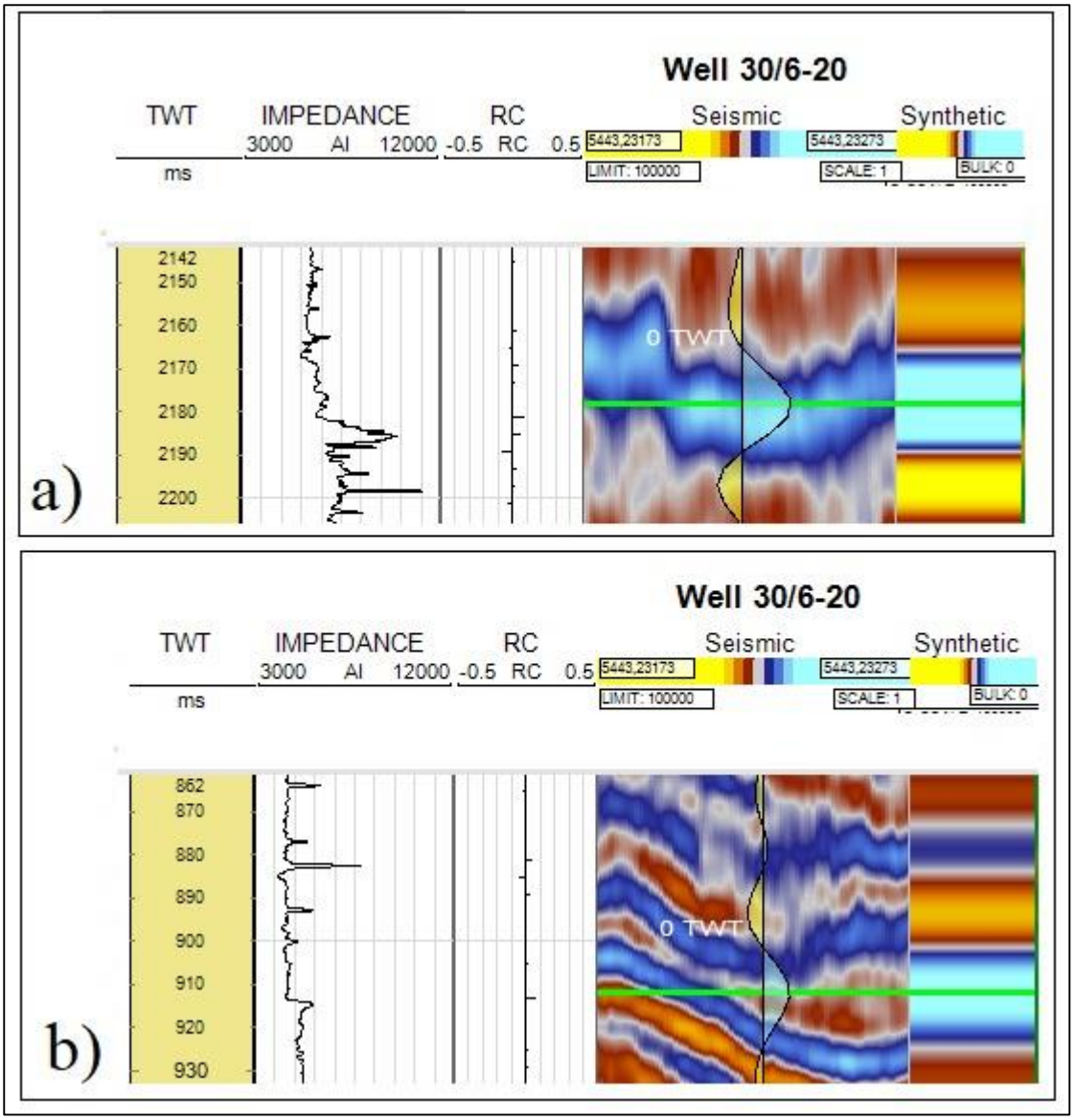

Figure 39: Seismic to well tie after implementing the bulk shift: a) Showing Top Shetland Gp. b) Showing Top Hordaland Gp. The seismic section is adjusted such that the synthetic seismogram is now consistent with the near angle stack.

For a good well tie where the well log data and seismic amplitudes correspond, extracting an appropriate wavelet is crucial. The characteristics of a wavelet—its phase, frequency, and amplitude spectrum—determine its shape. The Ormsby wavelet was chosen because of its flexibility, permitting easy adjustment and control with four principal frequencies: the low cut, low pass, high pass, and high cut. The prevalent frequency range within the investigated interval is between 7 and 30 Hz. As depicted in Figure 40, the Ormsby wavelet is symmetrical and has a zero-phase frequency spectrum. The frequency spectrum selected for the wavelet's low cut, low pass, high pass, and high cut is 3, 7, 30, and 50 Hz respectively (Figure 40)

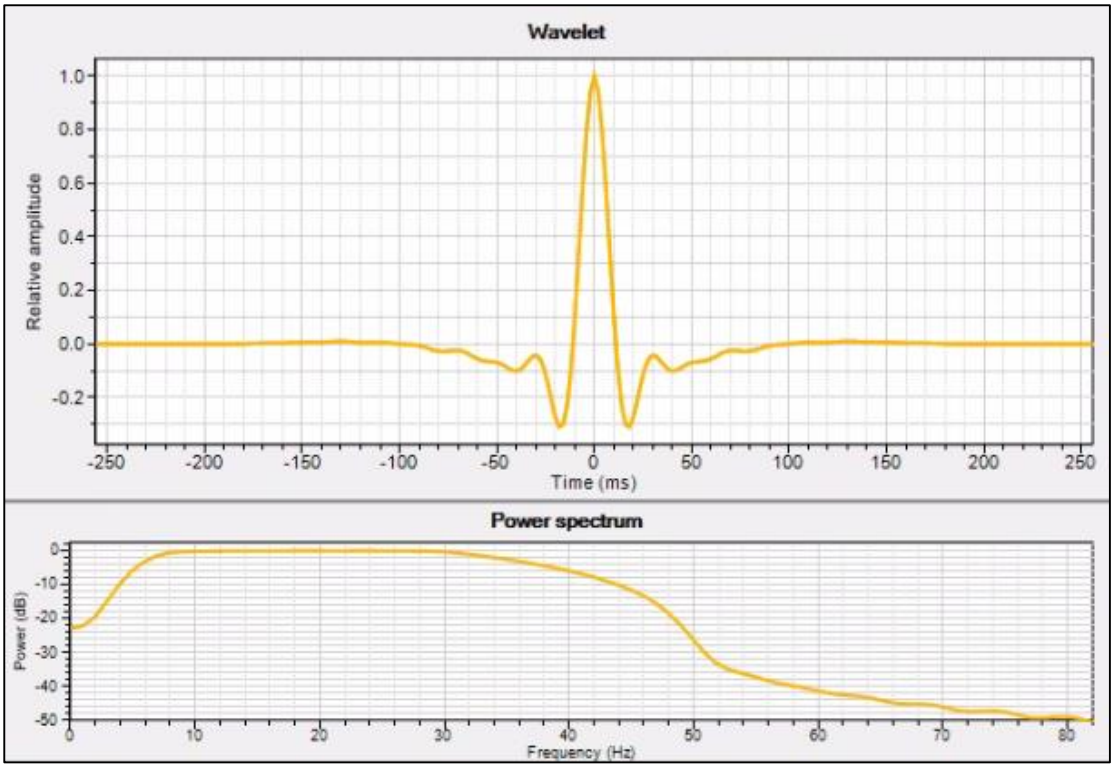

Figure 40: The Ormsby wavelet extracted from the near angle stack. (a) Designed zero-phase wavelet. (b) power spectrum plot highlighting a frequency range of 7-30Hz.

6.2. Spectral Decomposition

The initial step involved analysing the frequency band of the target interval within the seismic data. To accomplish this, the frequency spectrum analysis was employed (Figure 41) to examine the interval of interest ranging from -1s to -2 s TWT. The frequency band was divided into three sub-bands spanning low, mid, and high frequencies: 7-19 Hz, 20-37 Hz, and 38-50 Hz (Figure 41).

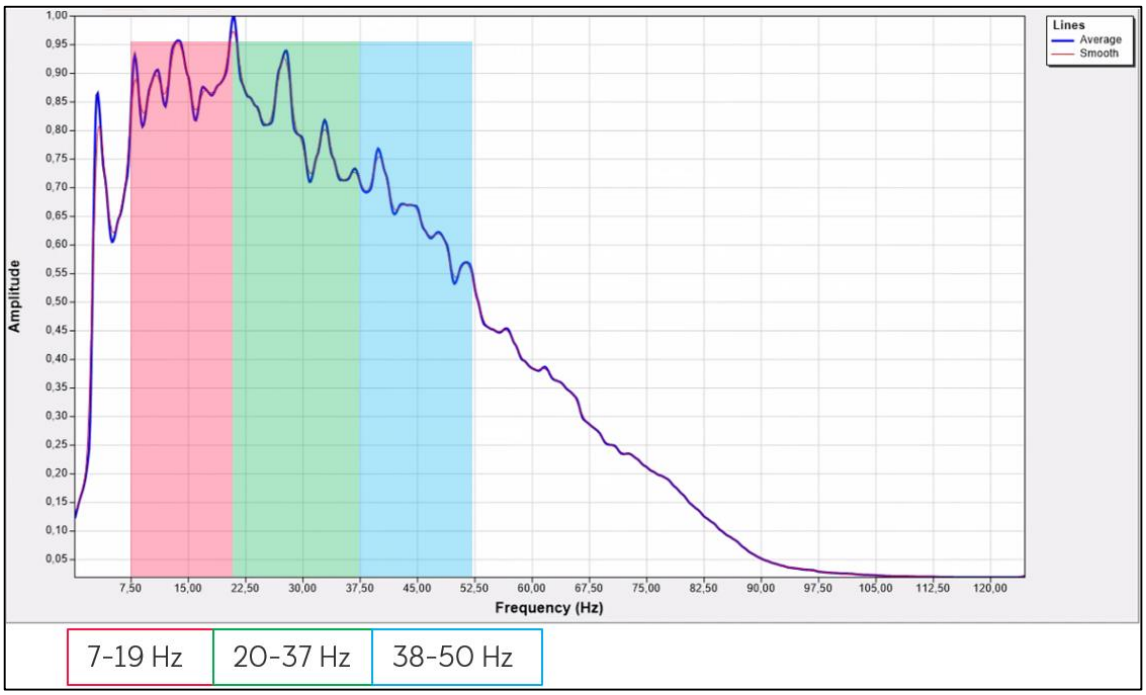

Figure 41: Frequency spectrum of seismic data and red, green, and blue frequency bands used for spectral decomposition.

The whole process entails performing spectral decomposition at three chosen frequency ranges, compiling the results, and then merging them into a single image, with each frequency mapped to a specific colour (Figure 42).

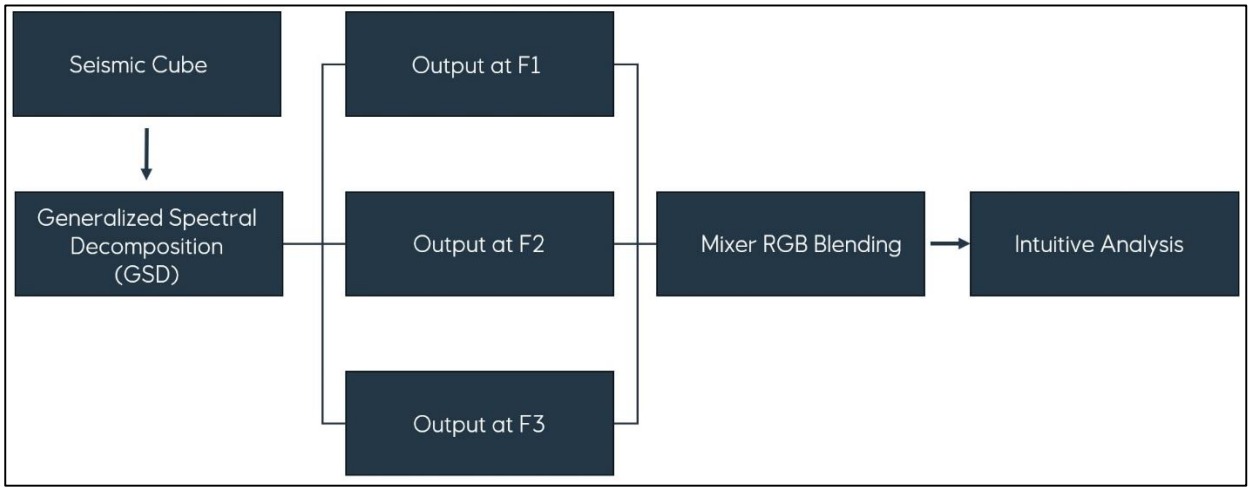

Figure 42: Generalized Spectral Decomposition colored blending workflow.

To determine the precise frequencies that would best emphasize the thin layers of remobilized sands within the tuning range, a cross plot of tuning frequency versus layer thickness was generated as outlined in chapter 5.5 (Figure 43). Various frequencies were tested by following the layer thickness line on the cross plot, with particular attention given to frequencies above 35 Hz for their potential to highlight the thinner layers.

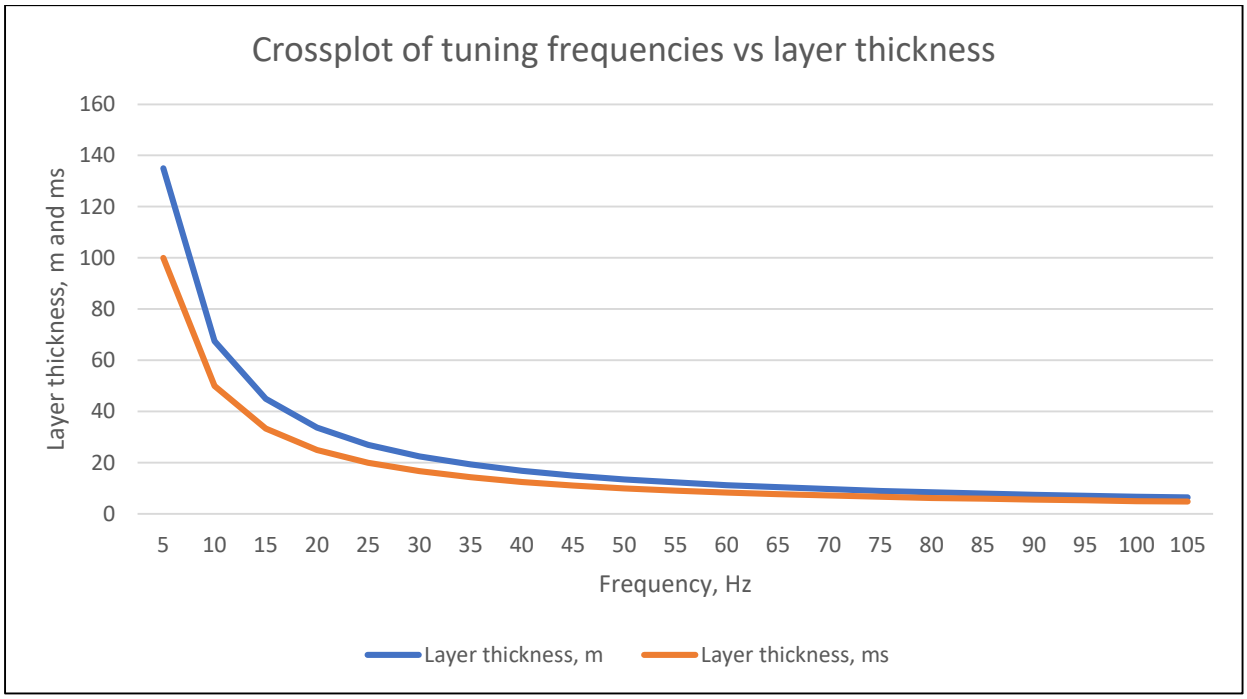

Figure 43: A reconstructed map of tuning frequencies following the procedures outlined in chapter 5.5. The thickness of the layers is expressed in both m and TWT ms.

The next step involves conducting generalized spectral decomposition in Petrel to segment the seismic data into the desired frequency ranges. Petrel's Generalized Spectral Decomposition (GSD) volume attribute uses a correlation technique that is based on the cosine function of a

specific frequency with the seismic within a gliding window. The methodology for utilizing the GSD volume attribute in Petrel can be divided into the stages shown in Figure 44.

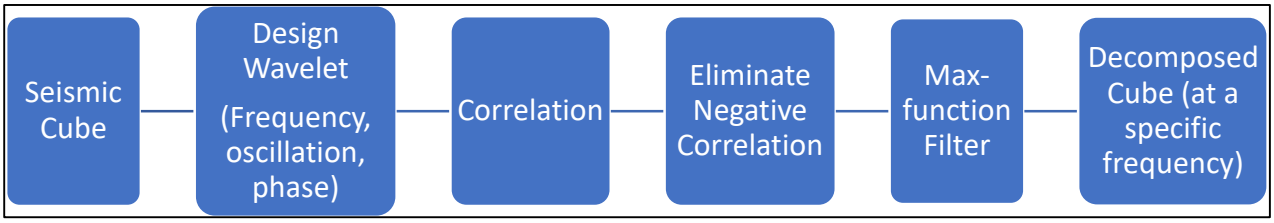

Figure 44: Schematic showing the Generalized Spectral Decomposition attribute workflow.

The chosen correlation algorithm, which quantifies similarity, was employed because it removes negative correlations between the seismic trace and the created wavelet, thereby enhancing the vertical precision of the frequency response.

6.3. Amplitude vs offset calculation

To lay the groundwork for AVO modelling, preliminary manual calculations were performed in Excel to benchmark the results, understand the process and investigate the relationship between gradient and intercept. For these calculations, Hilterman's modification of Shuey's reflectivity equation was used to determine reflectivity as a function of the angle of incidence, as explained in chapter 5.1.2. As the first step, average values for input parameters like bulk density (ρ), compressional wave velocity (V_p), and shear wave velocity (V_s) were obtained from well log data for specific intervals (sand units and overlying shales). There are four variations of well log data for each parameter – LFP_name_V (raw, real log), LFP_name_B (brine-saturated), LFP_name_O (oil-saturated), and LFP_name_G (gas-saturated), representing fluid-substituted logs. These logs provide insight into the expected seismic response for specific fluid types within the pore spaces. After determining the input values from each fluid-substituted log set, calculations were made for acoustic impedance (AI), Poisson's ratio (ν), and zero-offset reflectivity (R_0), based on the formulas mentioned in chapter 5.1.2. The next phase involved calculating the reflectivity coefficient as a function of the angle of incidence θ using the provided inputs and Hilterman's adaptation of Shuey's equation. With this information, the gradient can be determined – the difference in reflectivity between the first and last offsets – and define the intercept, which corresponds to the reflectivity at zero offset (R_0). In the last step, Gradient-Intercept plots and amplitude-angle plots were constructed. This enabled the analysis of the seismic response variations with offset and facilitated the identification of AVO class anomalies. In conclusion, the entire workflow can be summarized and visualized through a schematic diagram line in Figure 45.

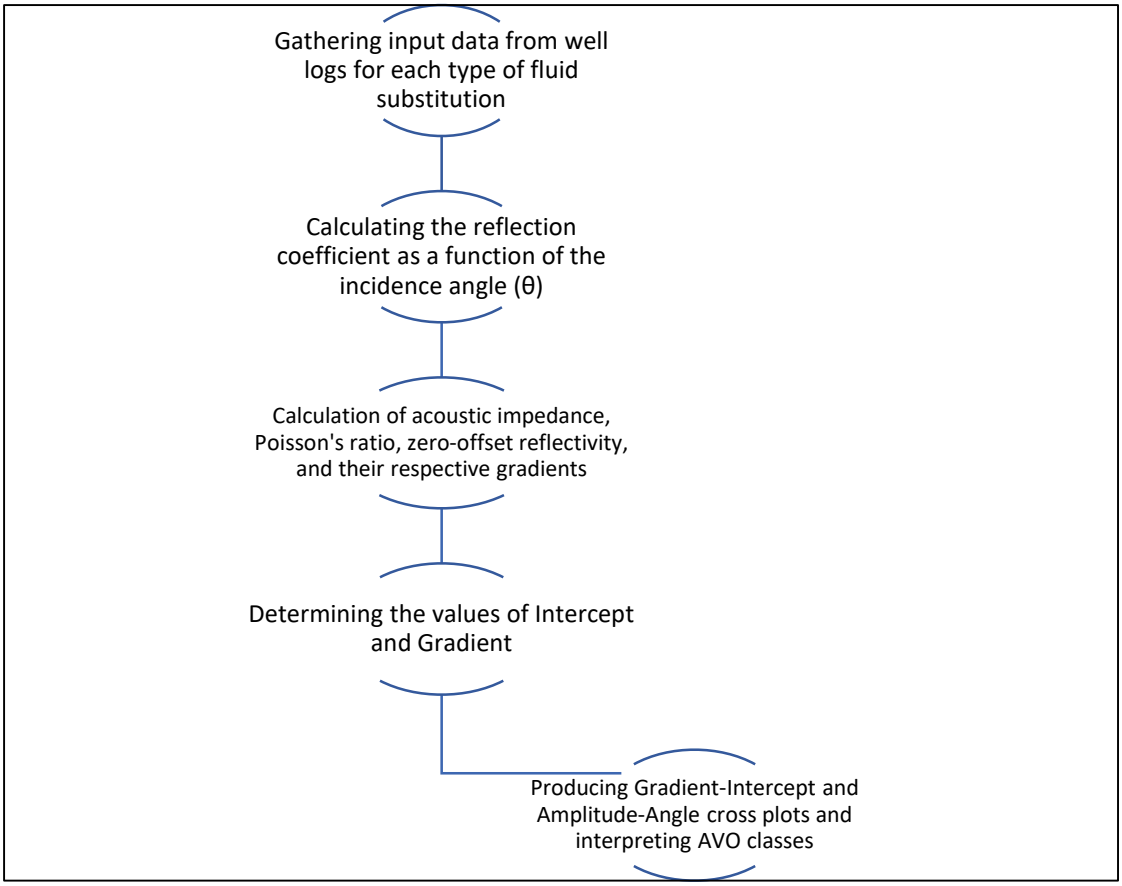

Figure 45: Schematic showing the AVO modelling workflow.

6.4. Seismic inversion, AVO, and EEI

The entire procedure was conducted using the AVOCADO module from Cegal, which is integrated into Petrel. The preliminary step involved determining the mid-angles at which the seismic data begin to ensure proper placement on the output Intercept/Gradient graphs. This information was found in the ZGY ASCII headers of each angle stack, specifically from the mute parameter. In this situation, the angles were - Near: 10°, Mid: 18°, Far: 26°, and Ultra Far: 34°. Once the appropriate AVOCADO tools were selected and all the angle volumes acquired, AVO analysis was conducted concurrently across all volumes (Figure 46).

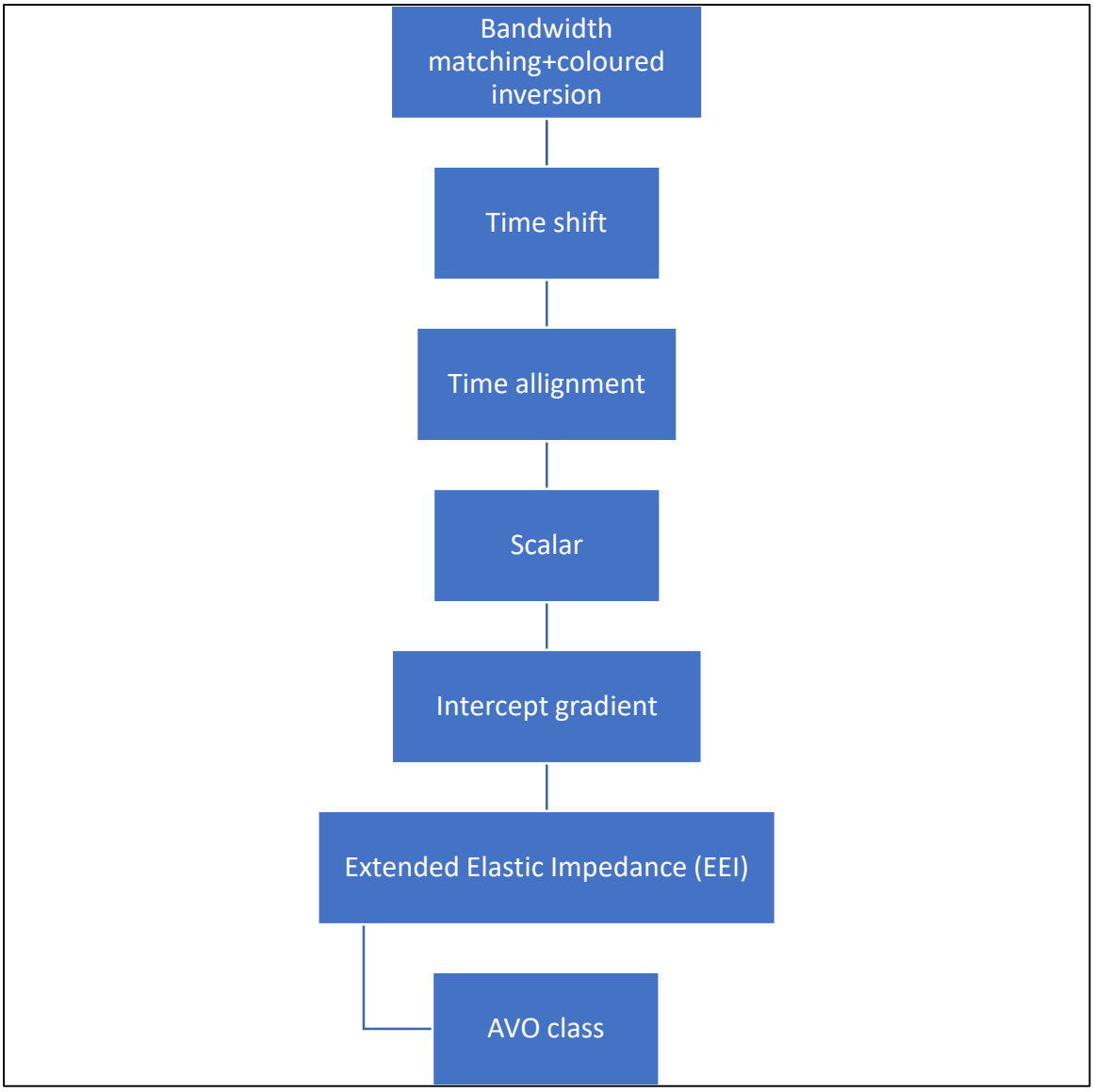

Figure 46: Schematic showing the Seismic inversion, AVO, and EEI attributes workflow.

6.4.1. Bandwidth matching and coloured inversion

The initial phase of the AVOCADO workflow involves performing Bandwidth Matching. This entails conducting a spectral analysis of the data to ensure that each seismic cube aligns within the same frequency spectrum. For instance, the near-cube typically encompasses the highest frequency range, while the ultra-far cube contains the lowest. The process begins by defining the analysis window, which ranges from -1 s to -2.5 s TWT over the chosen crosslines and inlines. The region of interest (ROI) was delineated around the sand injectite target by crosslines and inlines. Random traces were selected and a set of 300 traces, which provide a balance between a quick analysis and a sufficient overview of the overall frequency spectrum. The data was then smoothed to mitigate excessive noise. Subsequently, the spectra were calculated for all four seismic cubes. Upon examining the Amplitude-Frequency spectrum plot, it became evident that the ultra-far stack is richer in low frequencies, whereas the near stack predominantly features high-frequency content (Figure 47). This graph offers insights into the spectral properties, essentially displaying the frequencies present in the data and the relative

amplitude strengths of the volumes. Notably, most of their energy is concentrated around 15 Hz. The four red dots on the plot represent the filter parameters of the selected Ormsby target wavelet, which include the low-frequency cut-off, low-frequency pass, high-frequency pass, and high-frequency cut-off. Adjusting these points enables tailoring the frequency content of input data and design a specific target wavelet.

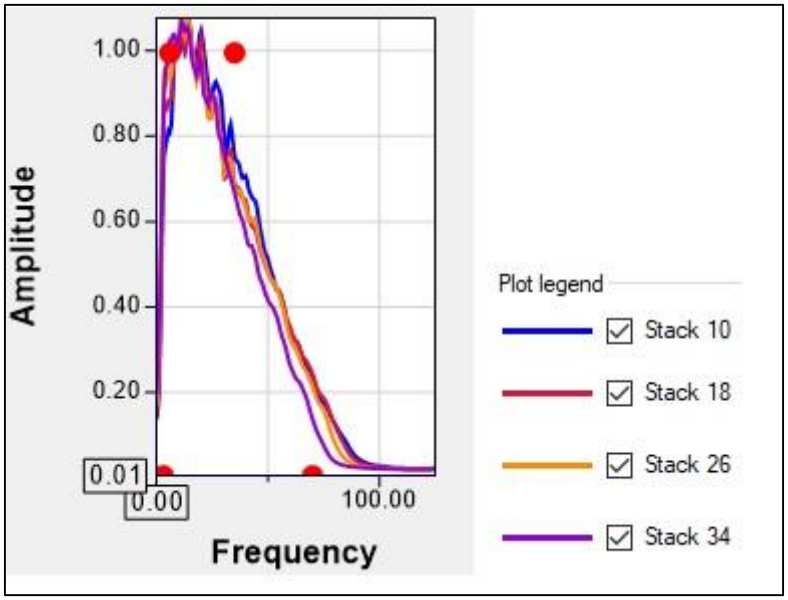

Figure 47: Amplitude-frequency spectrum of four volumes – near (stack 10), mid (stack 18), far (stack 26), and ultra-far (stack 34) stacks.

Upon close examination of the frequency spectrum of actual data (Figure 47), areas where all four volumes closely align correspond to the common frequency range through 3, 6, 28, and 70 Hz. The initial wavelet employed is a zero-phase wavelet, characterized by its symmetry around the zero point on the time axis. Due to the broad bandwidth of the data, there are minimal side lobes, with the bulk of the energy concentrated in the main lobe (Figure 48)

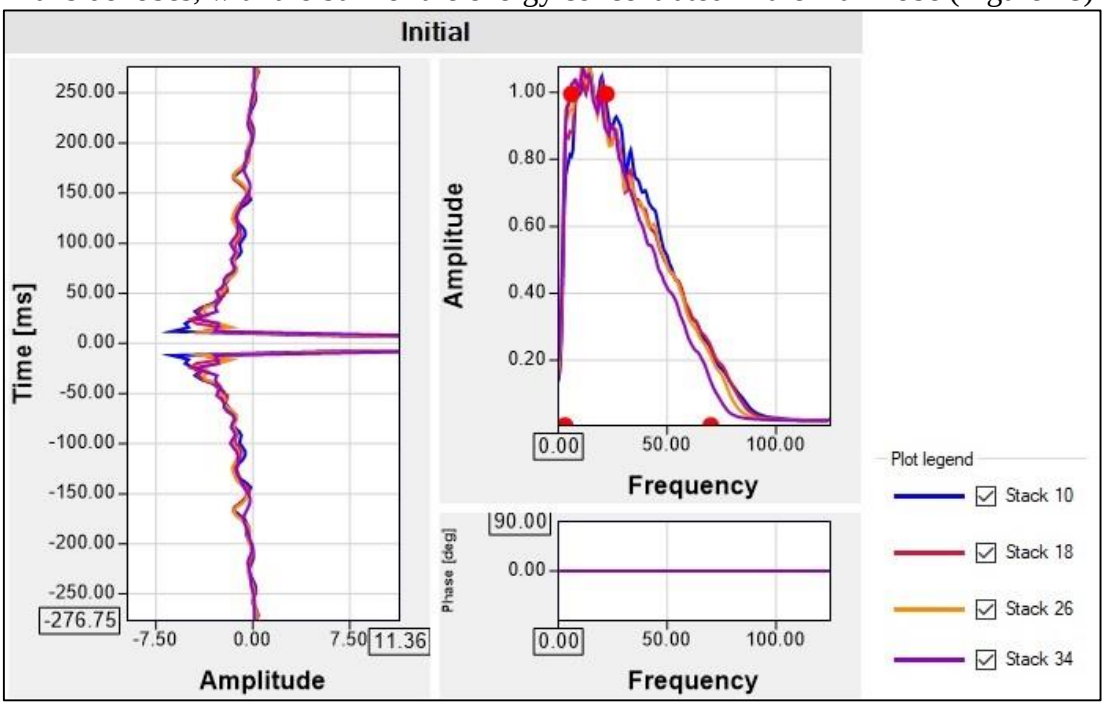

Figure 48: Initial wavelets for all four seismic volumes - near (stack 10), mid (stack 18), far (stack 26), and ultra-far (stack 34) stacks.

The next step was initiated with input data and a target wavelet to which all volumes would be aligned. Utilizing this target wavelet enables the execution of coloured inversion, which transitions from the reflectivity domain to a layer model, effectively moving energy to the layer. By adjusting the slope in the Frequency-Amplitude spectrum plot (Figure 49) and rotation settings correctly, an outcome equivalent to coloured inversion can be achieved. Consequently, the Amplitude-Frequency spectrum slope was set to a value of -0.8, aligning with the typical range for coloured inversion, which is between -0.9 and -0.7. Another critical step involves rotating the phase of the wavelet by -90°, transforming the reflectivity wavelet into a coloured inversion shape (Figure 49). As I modify the slope on the Amplitude-Frequency plot, it is possible to shift the energy toward the lower frequency end of the spectrum. This methodology, adopted from Equinor's workflows, employs a hands-on approach that sets it apart from the conventional techniques discussed in section 5.3. Grounded in the company's empirical experience, it has been determined that utilizing a negative slope value, that was used, tends to align well with the log spectrum; this empirical finding informed the decision to apply such slope values.

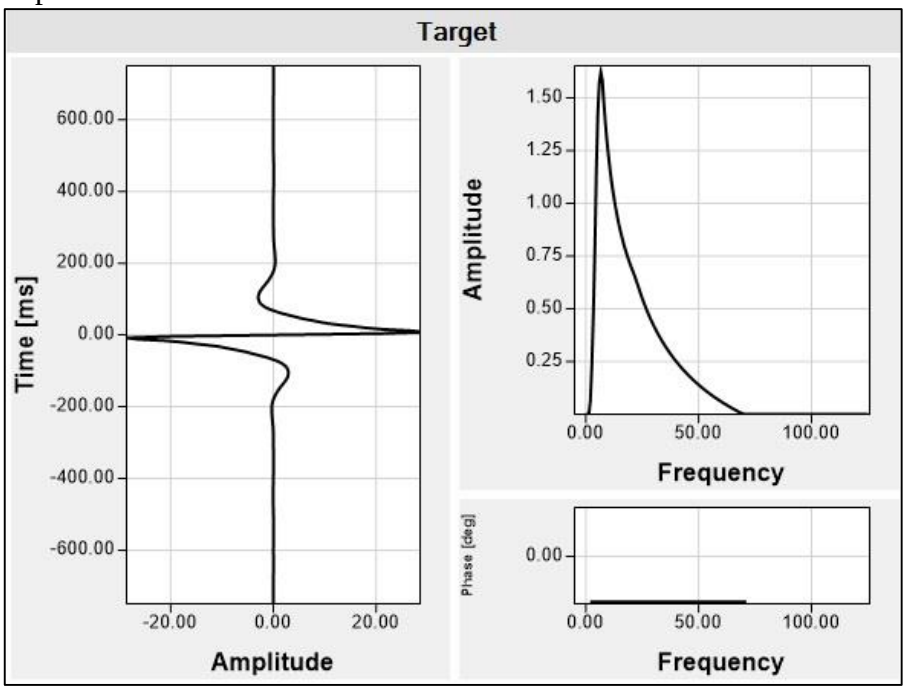

Figure 49: Produced target wavelet corresponding to the colored inversion shape.

Following these procedures, the coloured inversion volume was successfully generated (Figure 50).

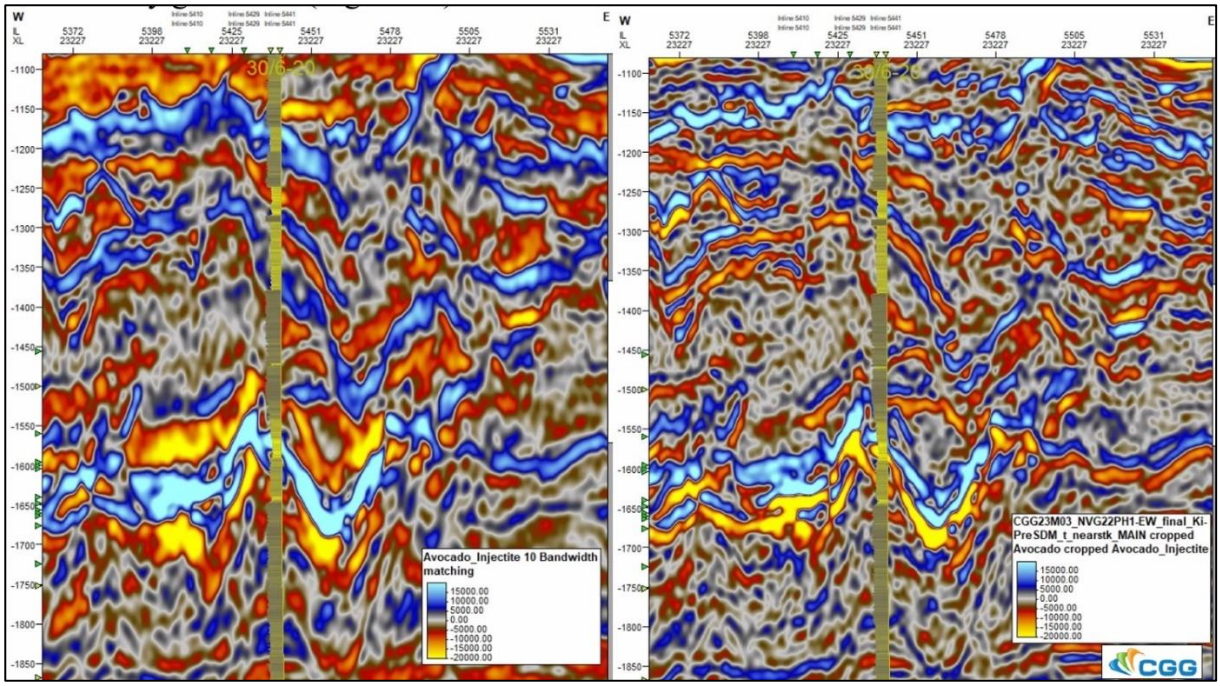

Figure 50: Comparison between reflectivity data volume (left) and colored inversion volume (right).

6.4.2. Phase matching

The goal of phase matching is to prevent amplitude variations that are due to differing phases across the cubes. The phase matching step is essentially performing a cross-correlation to assess the similarity of the datasets. Specifically, when applied to seismic data, cross-correlation computes the similarity between two seismic traces. The resultant trace from this correlation is obtained by systematically shifting one seismic trace in relation to the other, beginning with a zero shift and calculating the correlation at each incremental shift, which is known as the lag.

With a cross-correlation max lag setting of 200 ms, the analysis begins at -1500 ms (sand injectites interval), and a gliding time window of 600 ms is used. This setup means that the system will scan starting from -1500 ms within a +/- 600 ms gliding window and adjust one dataset by a maximum of +200 ms or -200 ms relative to another dataset. The master cube, set as the near stack, serves as the reference to which the phase of the other volumes is compared. If there is a symmetric correlation, it indicates that the datasets are best matched and effectively share the same phase, especially when there is no time shift or lag (i.e., a zero-time difference between the two volumes being compared).

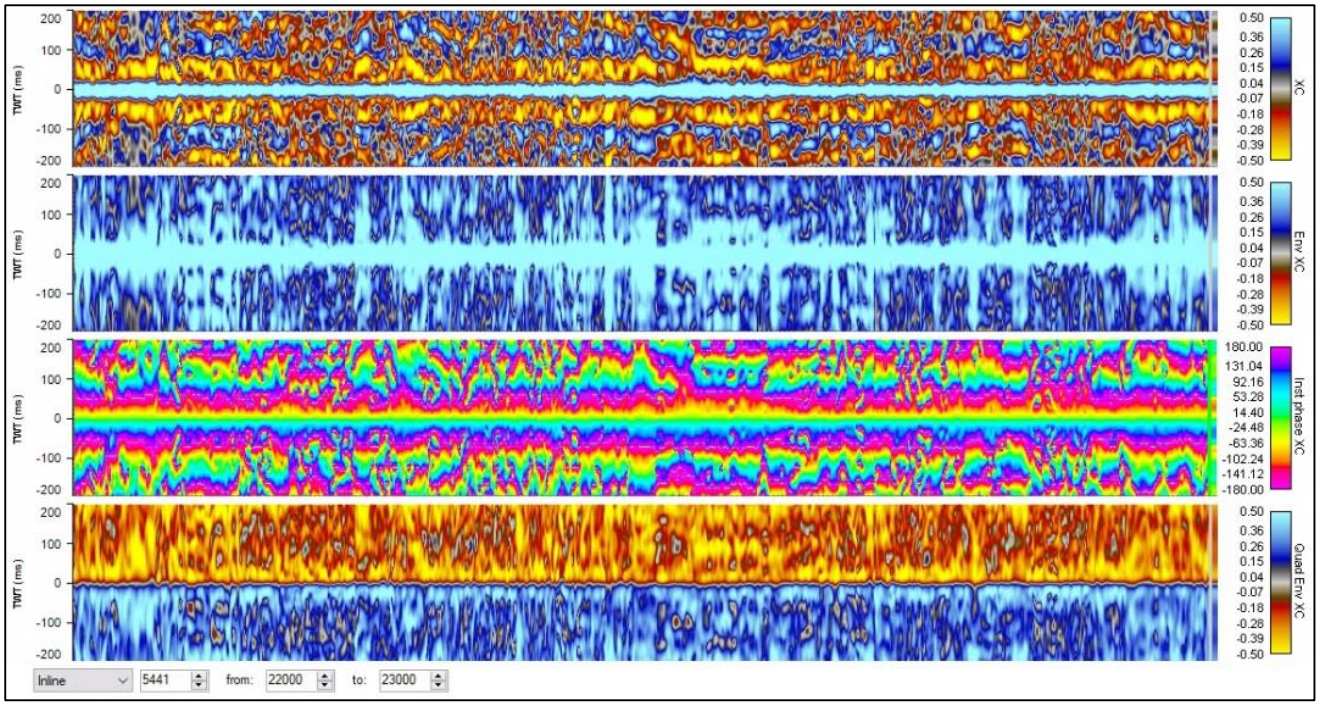

Figure 51: Phase matching plots that help to analyze differences in phase across seismic volumes.

Upon executing the phase matching module calculations, a variety of graphs are presented (Figure 51). The cross-correlation plot (XC plot) allows to observe that the side lobes are symmetrical, with minor acceptable variations (some spatial discrepancies evident). The second graph, which depicts the envelope function of cross-correlation (Env XC), transforms all troughs into peaks (highlighting only strong amplitudes), pinpointing the time difference. This is because the peak of the envelope function indicates the time shift between the cubes, even in the presence of phase differences. The plot reveals that the maximum amplitude lies at zero time—indicating there is no time shift, which is the desired outcome. The instantaneous phase graph of cross-correlation (Inst phase XC) indicates that there is a phase flip at zero time, with the colour legend providing clarity. Then the Quadrature Envelope of cross-correlation (Quad Env XC) adjusts the colour legend and exhibits a crossing at zero time. This zero crossing can be traced throughout the dataset to evaluate if there is a time shift between the volumes. These plots allow us to examine the phase as well as any overall time shift within the dataset. By analysing them, it is evident that there is not a significant average phase difference between the datasets, nor there is an observable systemic time shift. Nonetheless, at a very local, trace-to-trace level, sometimes discrepancies are detected, which require closer investigation using the time alignment tool.

6.4.3. Time alignment

The time alignment tool quantifies the magnitude of the time shift on a trace-by-trace basis across every cube, which is an extremely computation-intensive task. It performs pairwise comparisons among the cubes. The time alignment tool employs an algorithm that identifies local cross-correlation peaks and calculates the corresponding time shifts necessary to adjust seismic traces vertically. To determine a time shift between traces, it necessitates the presence of a seismic signal and a high correlation coefficient. The time shift is taken from the difference between the maximum of the correlation and what is referred to as the zero-lag. It's important to note that the cross-correlation is computed by sequentially shifting one trace in relation to the other, sample by sample, and calculating the correlation at each incremental shift (or lag). In instances where the data is noisy, the correlation results become noisy as well, affecting the

accurate identification of lag time at the point of maximum correlation. Under such conditions involving noise or lack of signal, the algorithm is simply interpolating horizontally and vertically the time shift from reliable cross-correlated data. This is done to correct for the residual time shift that exists when comparing traces from the near to the ultra-far stacks. A maximum allowed time shift value of 8 ms was selected because it is sufficiently large to capture subtle sample-to-sample variations, yet small enough to prevent incorrectly aligning with neighbouring seismic events that may display similar peak-trough patterns. By implementing a maximum time shift of 8 ms, all four near to ultra-far volumes were successfully aligned, from the near to the ultra-far (Figures 52 and 53).

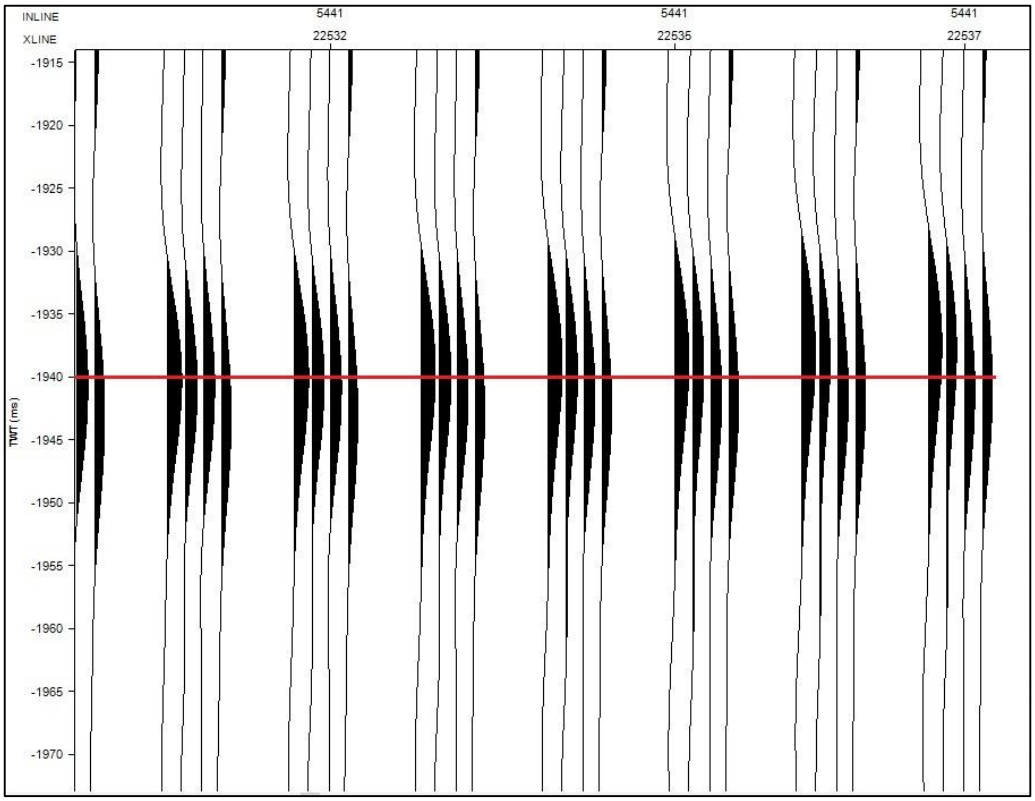

Figure 52: Original gathers before applying the time alignment shift. The red line at -1940 ms aims to help in comparison of time shift.

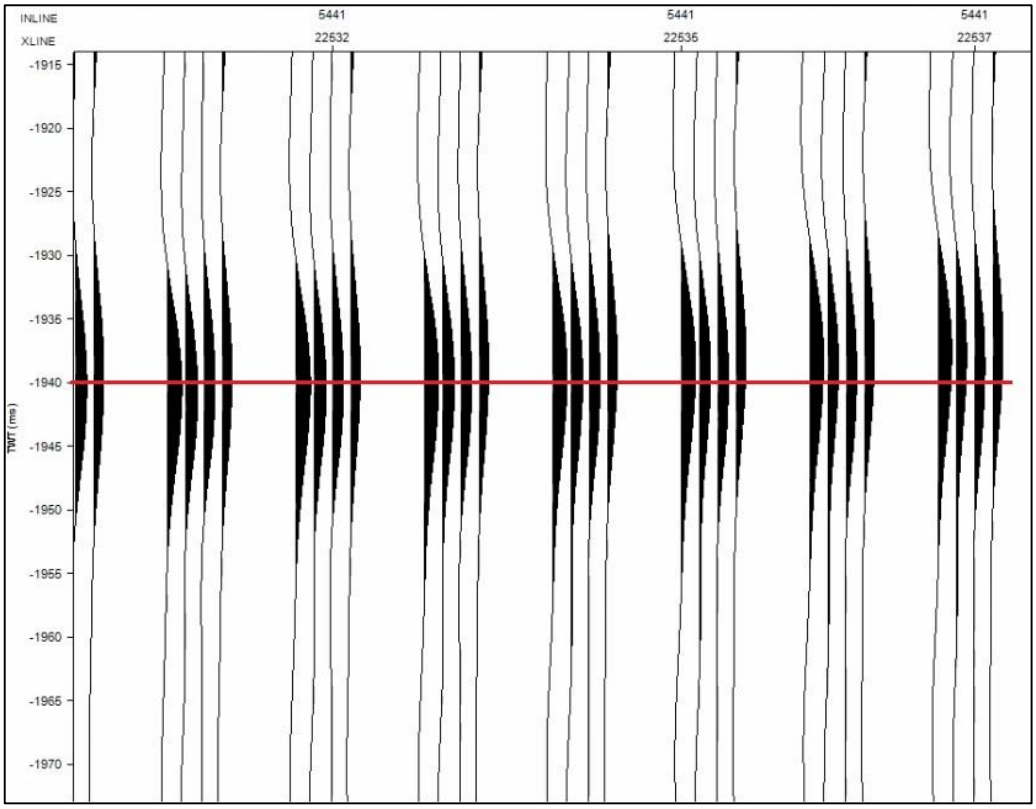

Figure 53: Gathers after applying the time alignment shift. The most notable upward shift is on the ultra-far trace (4th trace on each gather). The red line at -1940 ms aims to help in comparison of time shift.

6.4.4. Scalar

The scalar tool is designed to align the amplitudes of seismic events between the cubes by applying a uniform multiplier across each cube. This adjustment can either raise or lower the amplitude of each cube.

The scalar was applied after performing AVO calibration against known seismic responses. For instance, the Top Shetland Group is anticipated to exhibit a negative gradient (amplitude becoming less positive with offset), but anomalies showing a positive gradient were detected (Figure 54). Similarly, undesirable anomalies with positive gradients were noted in the Top Frigg Formation and within the investigated area of interest. By calibrating 'the AVO class: class strength' (explained in section 6.4.7) volume against the Top Shetland Group and considering the known gas response from the adjacent Nuggets field in the UK sector, an optimal scalar of 1.6 was applied (iteratively defined) to the near stack, which then linearly interpolated to 1 at the ultra-far stack.

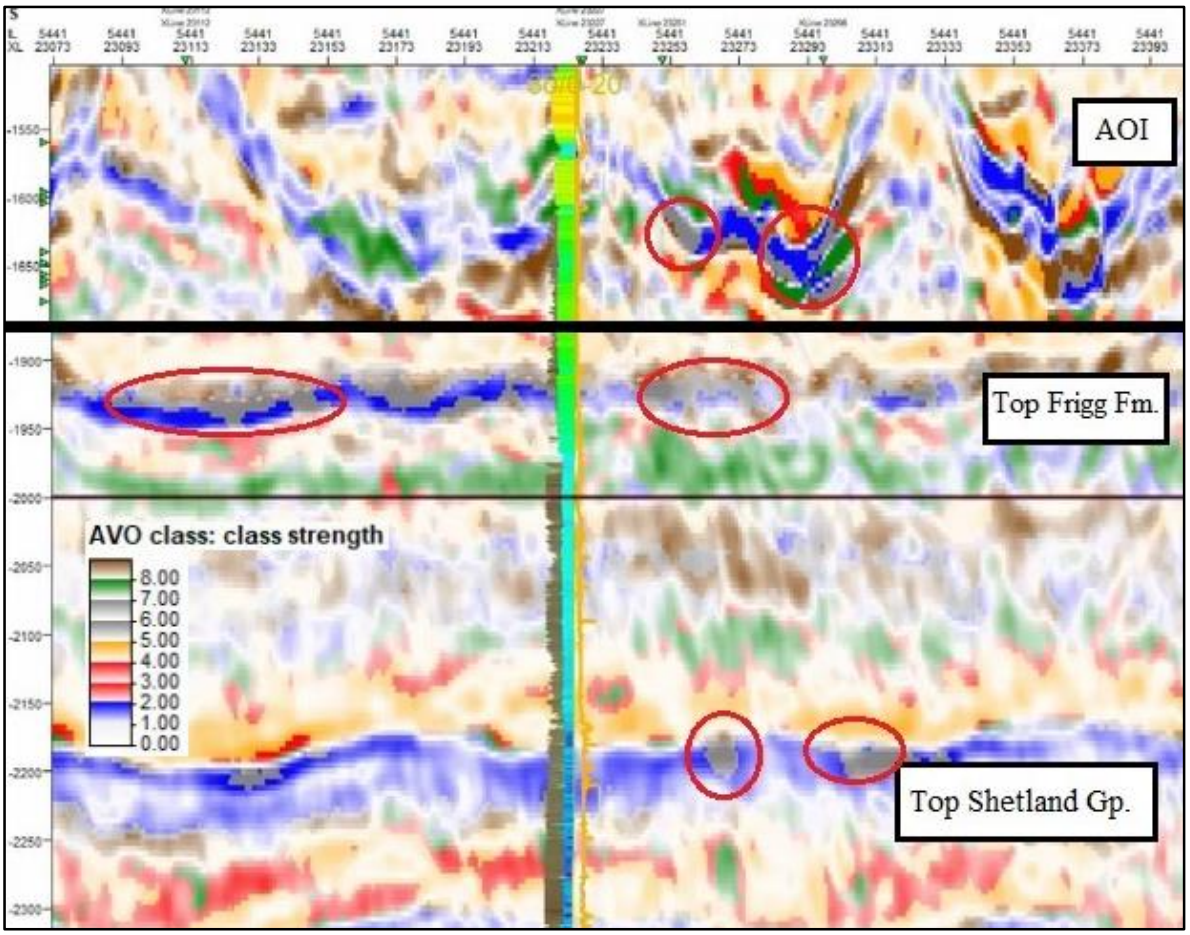

Figure 54: The AVO class volume reveals unusual anomalies within the Top Shetland Group, Top Frigg Formation, and the studied remobilized sands, which are highlighted by the red circles. The anomalies in the grey areas indicate a positive gradient where a negative gradient is expected.

6.4.5. Intercept-gradient

The intercept represents the best-fit line of angle stacks reflectivity projected back to zero-degree incidence angle ($\theta=0$). Similarly, by following this best-fit line, one can calculate the gradient, which essentially indicates how the amplitude varies as one moves from zero offset (the intercept) to other angles. In the intercept section, the top of the Shetland group is observable as a notably strong event (Figure 55). From the corresponding cross-plot showing reflectivity against $\sin^2(\theta)$, we can see that this event has a positive intercept, which gradually becomes less positive as the offset increases. The four blue dots on this plot denote the amplitude values at the top Shetland group observed at each of the examined angle volumes (10, 18, 26, and 34 °) for one CDP. The specific values for the intercept (I) and gradient (G) are determined and presented at the bottom of the cross plot.

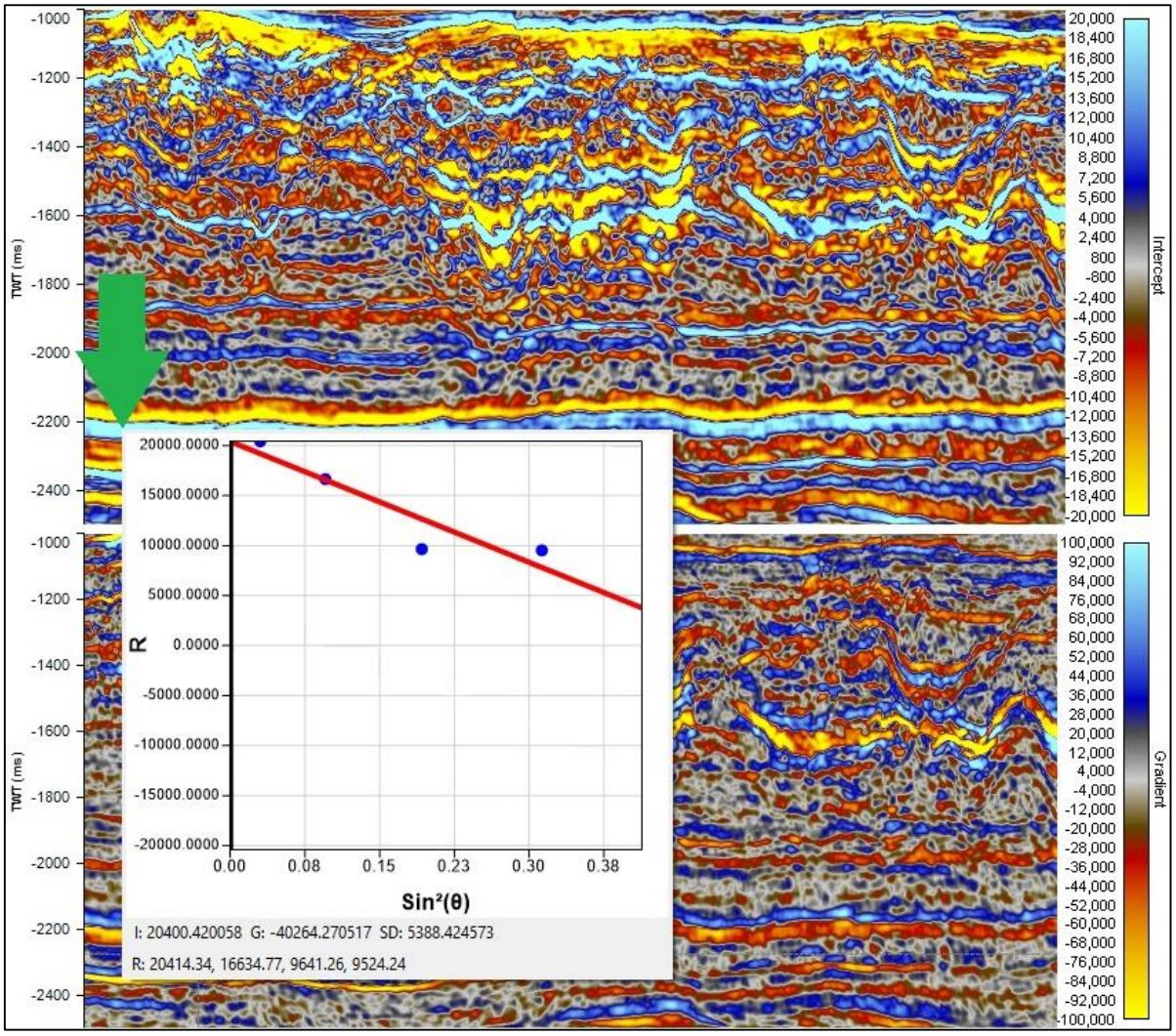

Figure 55: Intercept and gradient sections created across the Area of Interest (AOI). The data point is at the top of the Shetland Group and is indicated by the green arrow. For this point, a smaller plot illustrating Reflectivity (R) versus angle (expressed as $\sin^2(\theta)$) is generated.

6.4.6. Extended Elastic Impedance (EEI)

As discussed in Chapter 5.4, Extended Elastic Impedance (EEI) is influenced by the chi angle, χ, and its various projections, which serve to highlight different properties.

The initial step in this process is to make a normalization probe, which is intended to accurately balance the relative strengths of the gradient and intercept, derived from the coloured inversion of the angle stacks, allowing them to be standardized. To do this, a line probe (selected area of interest) is used along an Inline (at the location of the well) to calibrate the intercept and gradient and define an interval of Xline that encompasses the region of interest – sand injectite complex.

The EEI tool is designed to generate extended elastic impedance attributes for specific χ values that correspond to fluid sensitivity and lithological differentiation. The formula used is equation (15).

By employing the Blueback Seismic Reservoir Characterization tool, the cross-correlation between the EEI log and the wells shear impedance log was computed for each χ projection. In essence, this process determines the χ angle which delivers the highest correlation coefficient between the rotated elastic impedance and the selected well log. For this study, the optimal χ

angle for creating a lithology volume (shear impedance volume) was identified as -45° in the AI and GI cross plot (Figure 28). This angle yielded the highest correlation coefficient (Figure 56). Shear impedance is chosen as a marker for lithological variations because it utilizes shear wave velocities and bulk density. These velocities are predominantly influenced by the rock matrix or the lithology itself, making shear impedance a valuable tool for isolating and accentuating changes in lithological properties. When cross-correlating the Lambda-rho parameter, which is associated with the fluid projection (Figure 28), the relevant well log data was not accessible in the dataset. Therefore, χ angle of 15 ^{0} was selected, guided by the company's experiential knowledge.

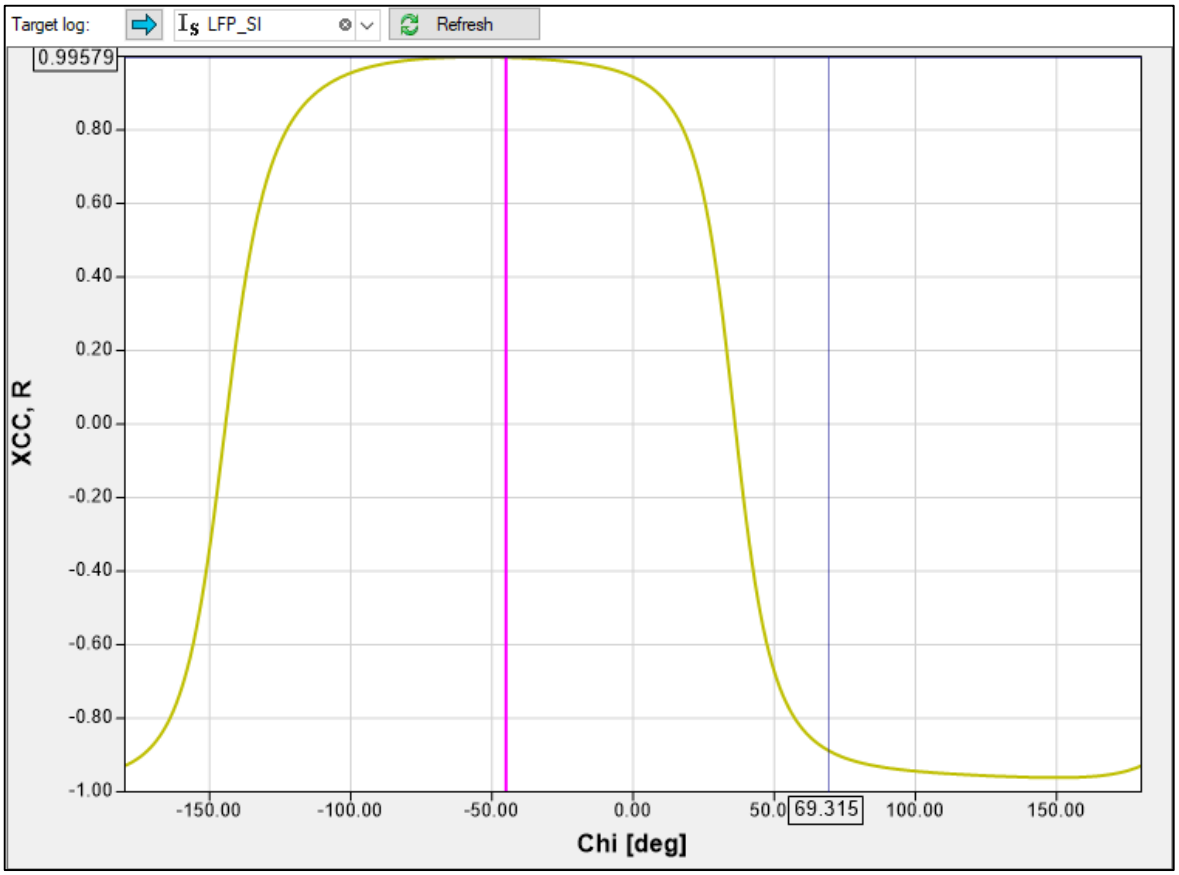

Figure 56: Plot of Correlation coefficient EEI of shear impedance (LFP_SI) and chi angle (χ) for a range of -180 to 180°. The highest correlation occurs at approximately -45°, which is shown by the pink line on the graph.

6.4.7. AVO class

In the final step, the AVO class module was employed. Utilizing the same spatial selection from the preceding steps, intercept and gradient values were extracted. These were then plotted onto a color-coded display, where specific AVO classes were assigned to various data regions (Figure 57).

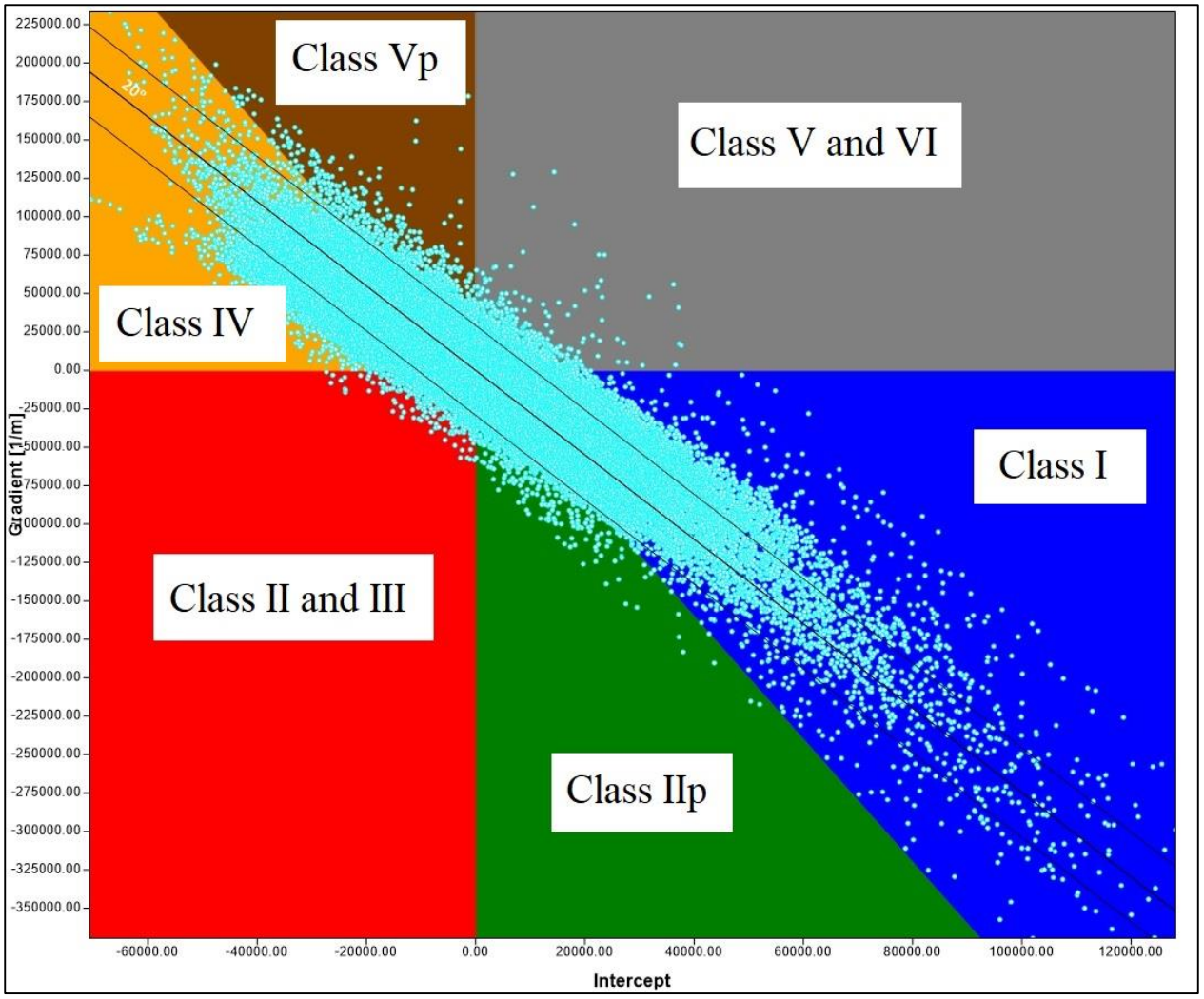

Figure 57: Gradient-Intercept plot with data points. The overall pattern of the points aligns with a fluid line response at approximately 20°.

Upon obtaining the plot, the shale line is introduced to be somewhere between 15 and 20°, which allows to assign a strength parameter to each point. This parameter essentially represents the distance between the fluid line (referred to as the mud line or shale line) and the point: the greater the distance, the higher the strength. To accommodate the bulk of the point cloud effectively, the ideal strength scale window has been established for 30,000 data points.
Finally, the module outputs virtual seismic attributes containing information about the AVO class of the data. It creates three attributes:

- AVO Class, containing an integer value mapped to the colour scale bar for the AVO class of each sample point.
- AVO Strength, containing a value between 0 and 1 indicates the strength of the AVO anomaly.
- Combined AVO Class + Strength, containing a value combining the integer part of the AVO Class, and the decimal part of the strength. A colour scale bar is created so that the stronger the anomaly, the brighter the colour. Weak anomalies show white.

7. Results

This chapter covers the results and their interpretation in light of the thesis objectives. The spectral decomposition, AVO, EEI, and FWI results are compared, discussed, and summarized in separate chapters.

7.1. Overview of structure

The focus of this study is on a local (few km) concentration of wing-shaped formations spanning from -1200 ms to -1800 ms TWT, intersected by well 30/6-20 (Figure 58). By looking at the near to ultra-far angle stacks, it is evident that the remobilized complex exhibits notable amplitude variations with changing offset, with the maximum amplitudes appearing in the near stack. Additionally, sand injectite formations are characterized by cross-cutting existing strata, wing-like shape, hard reflections at the base, and near-zero amplitude at the top. These features make the delineation of these bodies a complex task.

Alongside the seismic data, well log data were employed, and these substantially aided interpretation. As discussed before, well 30/6-20 was tied to seismic, which facilitates the understanding of the seismic-well log response for the events of interest. With the Gamma Ray (GR) log and acoustic impedance (AI) log displayed, there is a clear correlation between the seismic and well data, where the strong (blue coloured) amplitude reflectors correspond with lowered blocky GR responses and an increase in AI at the base of the reflectors. This is indicative of sandy formations. Such seismic-well log patterns are observed across four distinct intervals (Figure 58).

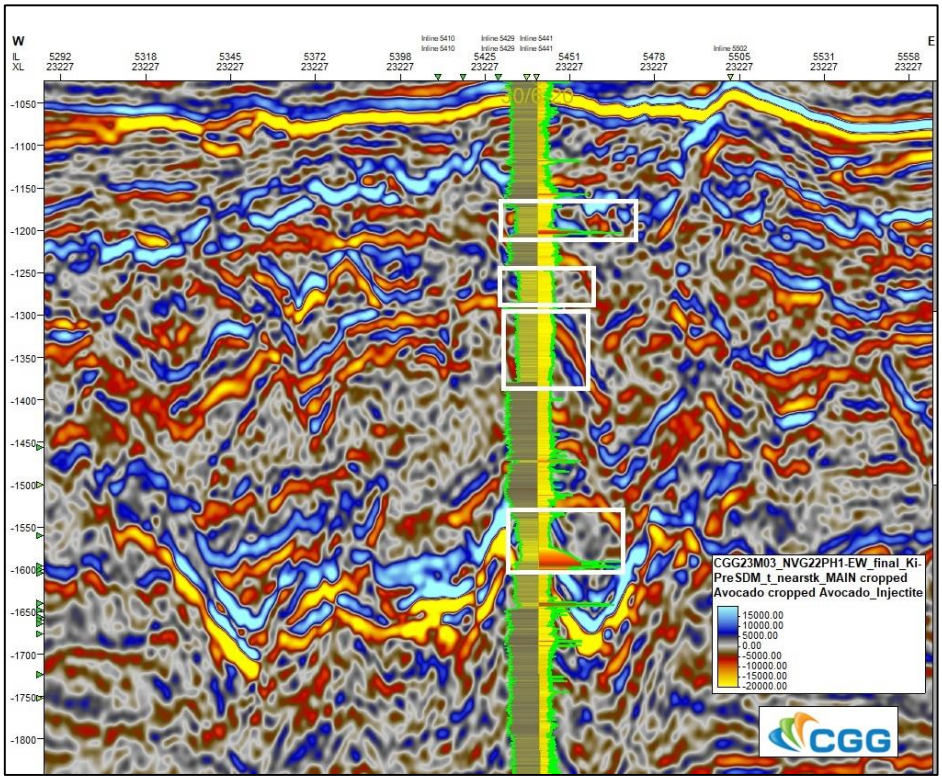

Figure 58: Near-stack reflectivity data with GR (to the left) and AI (to the right) logs along well 30/6-20. Four sand sections can be identified (white rectangles) and these can be remobilized sands.

Examination of the well logs, including Gamma Ray (GR), bulk density (LFP_RHOB), and P-wave velocity (LFP_VP_V) (Figure 59), reveals that these four intervals are easily distinguished by blocky responses—a signature that suggests the possibility of drastic changes in lithology or processes such as sand remobilization. Specifically, the GR values fluctuate between 44 and 52 gAPI, which are substantially lower than the average background response and indicative of sandstone, limestone, or dolomite. The bulk density ranges between 2.07 and 2.11 g/cm³, aligning with the densities typically associated with sandstone. P-wave velocities display notable deviations from the surrounding lithology and are approximately 2170 m/s within the four intervals, except for some localized peaks that reach 3200 m/s at the bottom of the layers. The increase in both V_p and bulk density explains the rise in acoustic impedance at the same points, raising suspicions of possibly cemented sections within the sandstones (Figure 59).

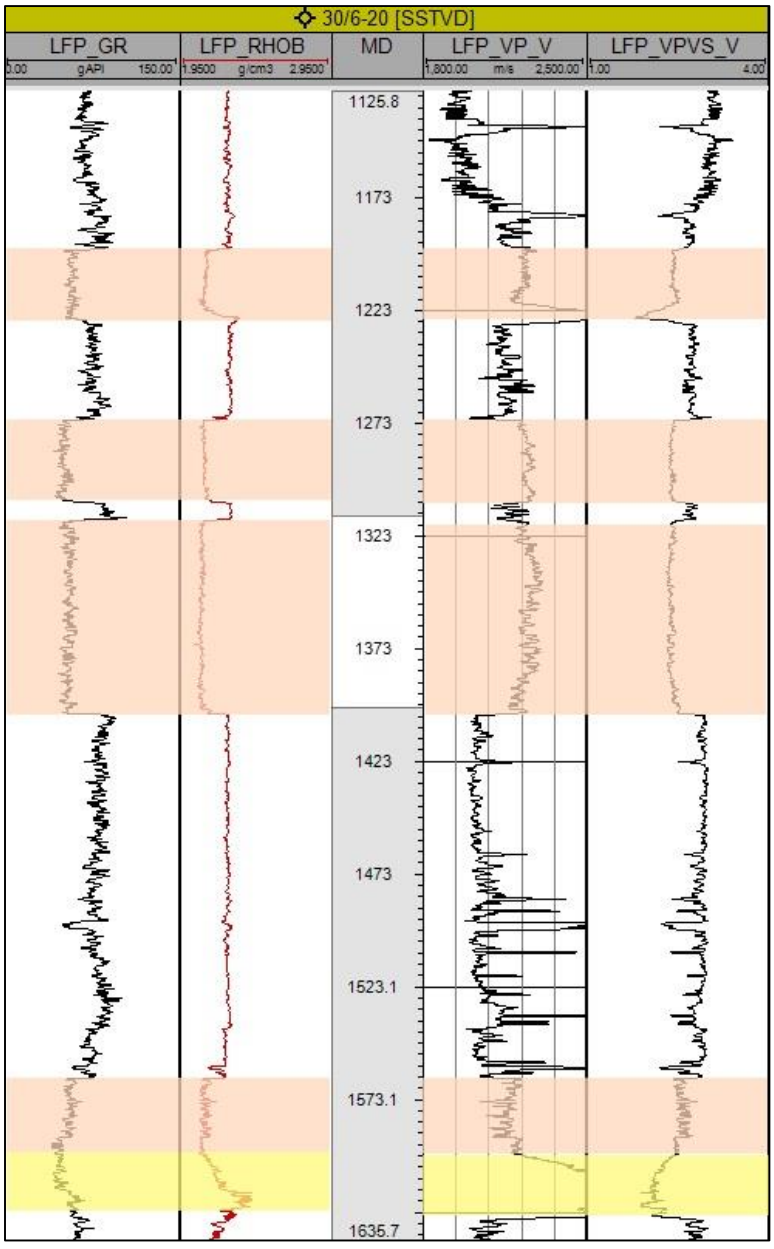

Figure 59: Gamma Ray (LFP_GR), bulk density (LFP_RHOB), acoustic impedance (LFP_AI), and V_p/V_s ratio (LFP_VPVS_V) logs in well 30/6-20. The orange intervals suggest zones of possible uncemented sand, while the yellow interval is likely cemented base sand. MD is in m.

The interpretation of the well logs is validated by drill cuttings photographs from the corresponding intervals and the surrounding shales. For instance, in the deeper section (Figure 60), there is a significant presence of carbonate cement (evidenced by whitish cuttings), along with minor quartz fragments—factors that contribute to the increased acoustic impedance and strong seismic amplitude between hard sands and soft shales. Moving upwards, the lithology is characterized by coarse grains and a rich concentration of quartz grains (Figure 60). The surrounding shale is also easily differentiated based on its fine-grained texture.

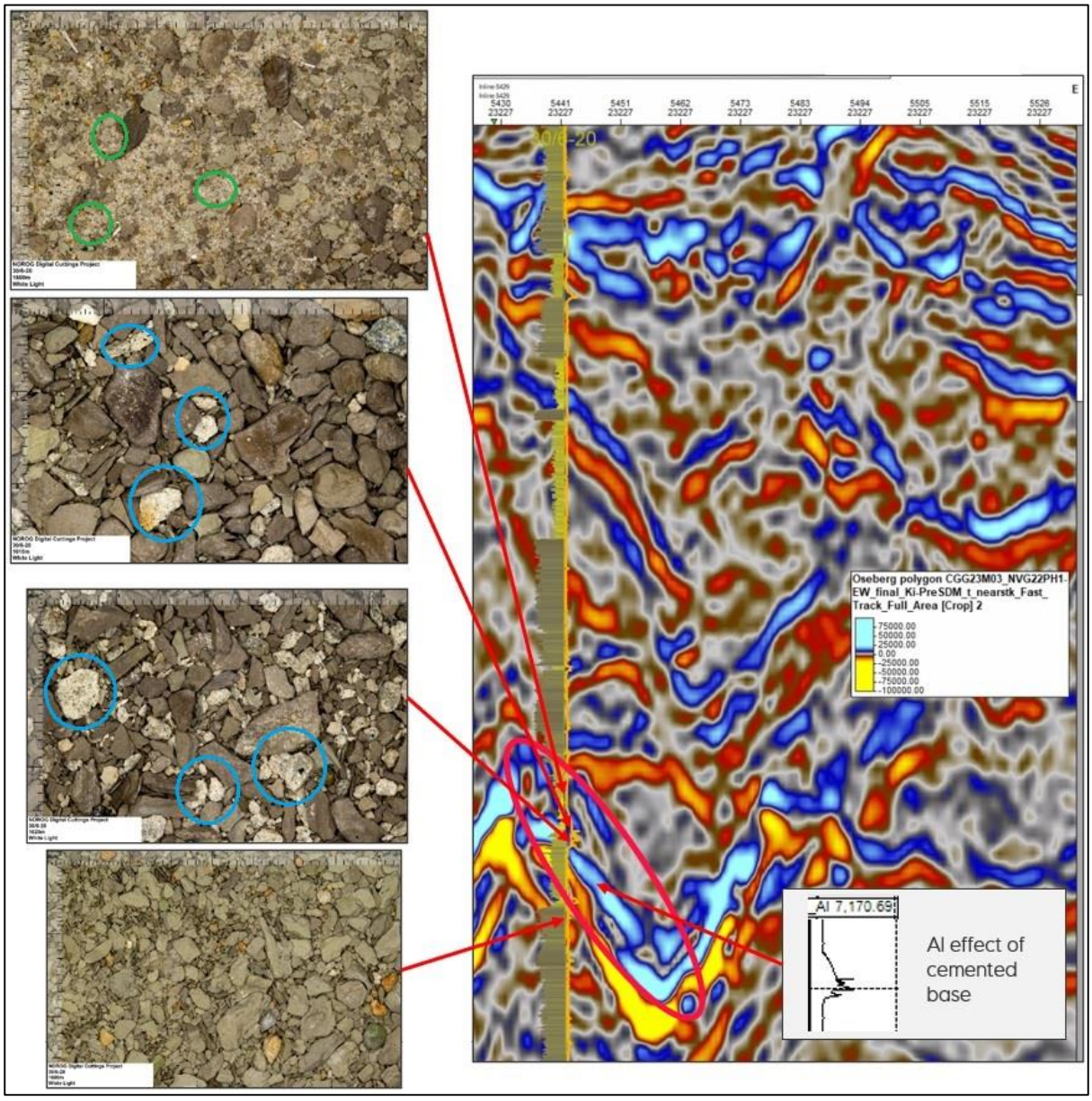

Figure 60: Near-stack seismic alongside photographs of drill cuttings along well 30/6-20. Red arrows indicate the corresponding depths of the drill cuttings. Blue circles show carbonate cement, green circles – quartz particles. Inset of the seismic section is the Acoustic Impedance (AI). The increase of AI coincides with carbonate cement.

As the remaining three intervals were examined, the pattern persists—the intervals feature uncemented sand with an abundance of quartz content and traces of carbonate cement. Similarly, the background shale stands out due to a drastic increase in GR (Figure 61).

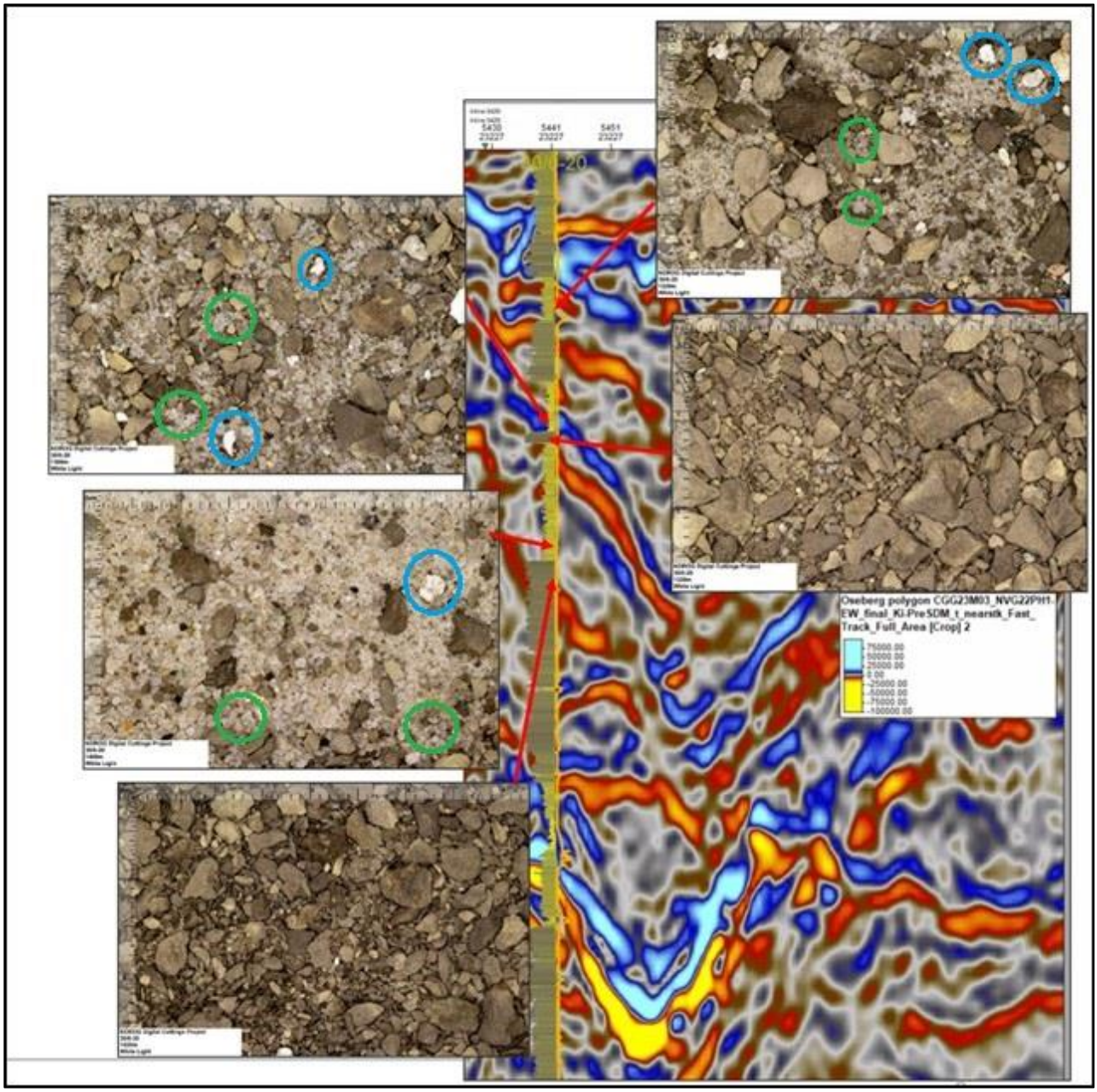

Figure 61: Near-stack seismic section and corresponding photographs of drill cuttings along well 30/6-20. The red arrows point to the depth levels of the cuttings. Blue circles show carbonate cement, green circles – quartz particles.

7.2. Spectral Decomposition

By selecting frequencies that highlight features with a thickness of less than 20 m, a cross plot of tuning thickness versus frequency was utilized (Figure 43) and frequencies from 10 to 45 Hz were tested. After iteration, optimal results were obtained for a frequency band combination of 12 Hz (Red channel), 28 Hz (Green channel), and 40 Hz (Blue channel). The spectral decomposition time slices are depicted in Figure 62.

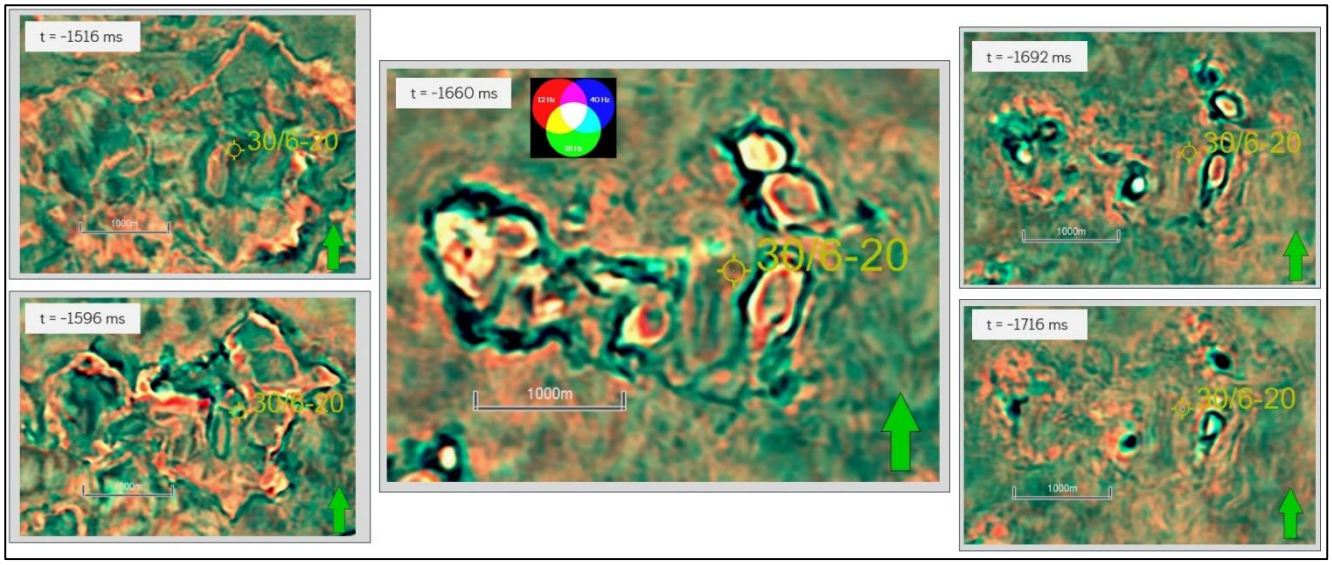

Figure 62: Spectral decomposition time-slices. More negative TWT means a deeper slice.

Starting with the deepest slice at -1716 ms, four dark point-shaped anomalies are evident, suggesting disruptions in the stratigraphy. These match well with the locations at the base of the remobilized conical-shaped bodies from the near stack seismic. Notably, within the south-east anomaly, there is a white response, indicating a concurrence of all three frequencies, and a drastic change in acoustic impedance. Moving upwards to the slice at -1692 ms, as anticipated, the area of these anomalies expands, which reflects the increasing size of the remobilized bodies up section. In the time slice at -1660 ms, the anomalies further grow, with red and white colours becoming prominent. The presence of red may indicate that the body's thickness is around 42 ms (refer to section 5.5), correlating with the measurements from the lower sections. At the upper time slices at -1596 ms TWT and -1516 ms, we observe that all bodies are enlarged, and their boundaries are more diffuse, with a weaker definition in colour response. The persistent white in the center with red-green at the edges suggests the same contours of the remobilized sands as identified by the reflectivity data (Figure 58). Minor green-blue events appear at the periphery of circular features, yet these responses are weak. From Figure 62, there are no extra signs of sand injection wings that weren't detected on the seismic, which might have been uncovered through tuning effects. A few theories might explain this observation:

- The spectral decomposition may be more effective at emphasizing and intensifying the boundaries of significant acoustic impedance changes already noted in the reflectivity data.
- It is possible that during the remobilization process, thin layers were not formed, possibly because there was sufficient pressure at shallow depths to fill only large fractures (chapter 4.2.3).
- Since the sand injectites manifest as sub-vertical wing-shape bodies, rather than horizontally oriented structures like sills or parent sand bodies, spectral decomposition finds it challenging to provide additional informative data.

Nonetheless, this manner of depicting the boundaries of the remobilized sands can be useful as a supplementary tool in the mapping of the sand base (Figure 63), particularly in areas where seismic reflection data may indicate a broad and intense amplitude response both from sands

and shales. The presence of pronounced white circular responses (Figure 63a) proved to be beneficial in interpreting the bottom sand layer (Figure 63b), by tracing the red markings (indicative of thicker sand) and the white responses (signifying strong amplitude across all three cubes). However, attempting to employ the same methodology for interpreting the near-top sand layer did not yield satisfactory results and continued to provide unreliable data (Figure 63c). Moreover, the distinct cross-cutting features sharply contrast against the background shale, providing valuable assistance during the preliminary phases of exploring the region for remobilized sands.

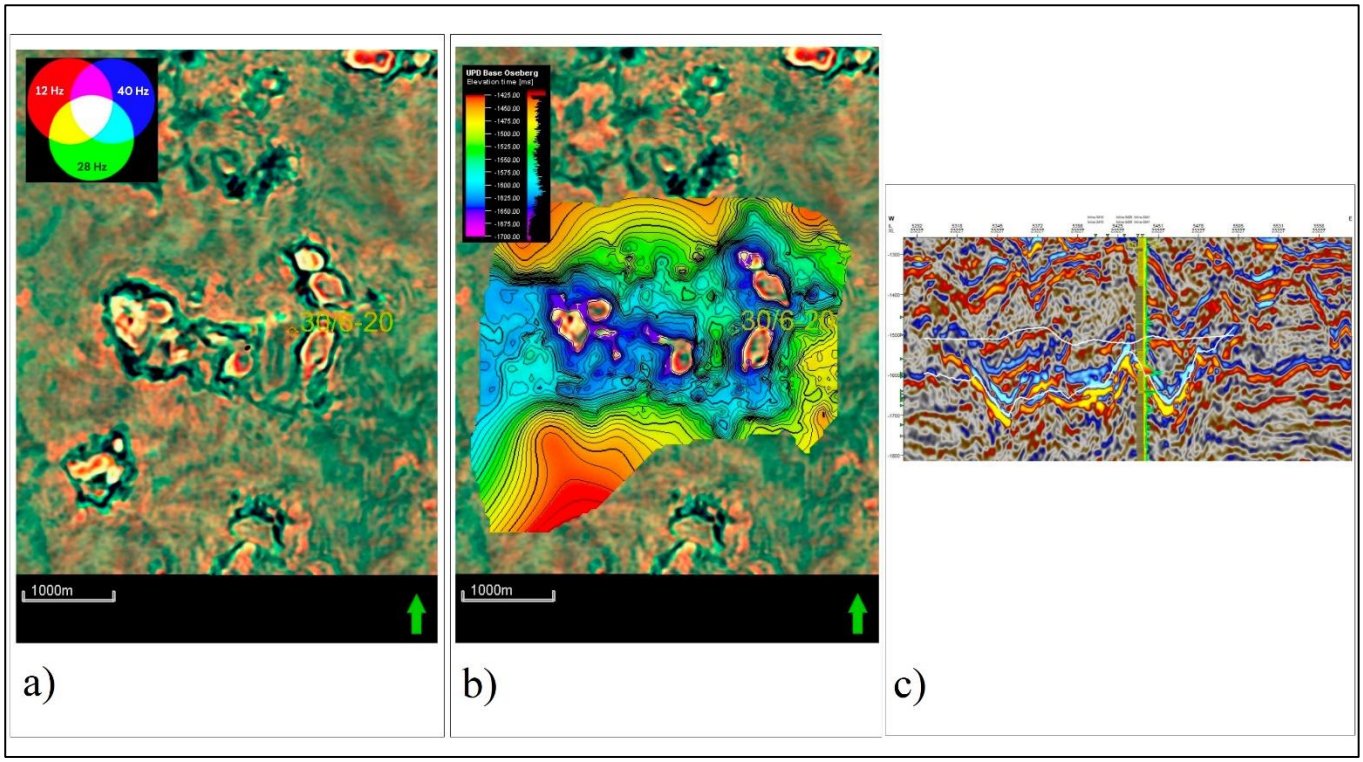

Figure 63: a) Generalized Spectral Decomposition (GSD) time slice at -1660 ms centred at the study area of sand injectites interval. b) Overlay of the picked bottom sand horizon on the GSD time slice. c) Crossline section of near-stack seismic data with displayed the picked near-top and bottom sand reflectors marked in white.

When contrasted with the near-stack seismic data, employing RGB blending of the frequency bands aids in emphasizing structures associated with remobilization, while diminishing the response from the background shales (Figure 64). Furthermore, attributes such as RMS (Root Mean Square) and variance also mark the boundaries of the zone of remobilization, though not as precisely as the RGB blending technique. The variance attribute tends to reveal discontinuities in both the background and the areas of remobilization. RMS amplitude emphasizes acoustic impedance variations in the sands, which could be instrumental in detecting cemented sections (Figure 64).

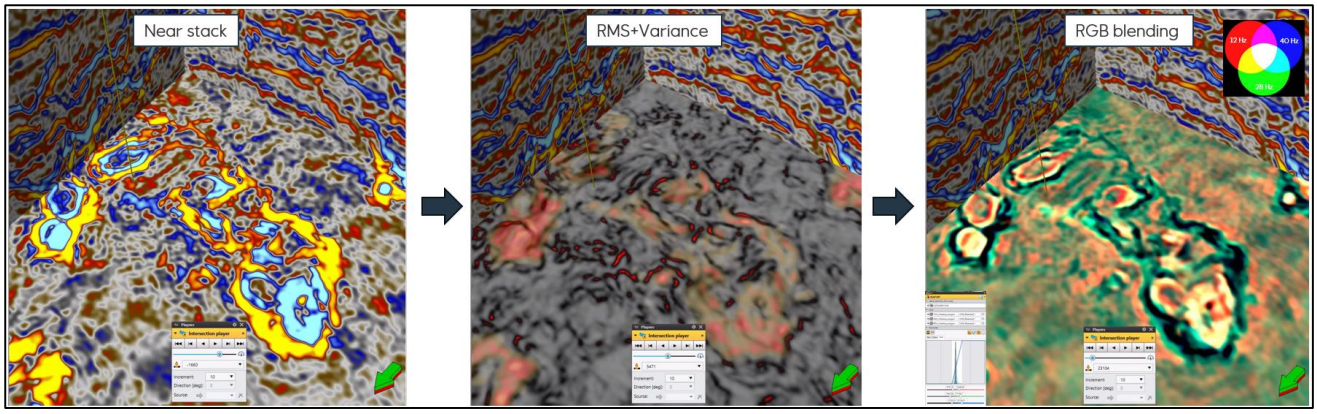

Figure 64: Comparison of the near stack, RMS+Variance attributes, and RGB blending of frequency bands. The displayed time slices are at -1660 ms.

Furthermore, in frequency domain analysis, the question emerged as to whether sand remobilization could be discerned from the background based on its frequency characteristics. The dominant frequency attribute was applied, revealing the absence of a significant regional-scale frequency trend that could assist in the identification of such features (Figure 65). While some local changes in dominant frequency are observed when comparing the background to the sands, these do not align precisely with the boundaries delineated through reflectivity data, spectral decomposition, and RMS+Variance attributes.

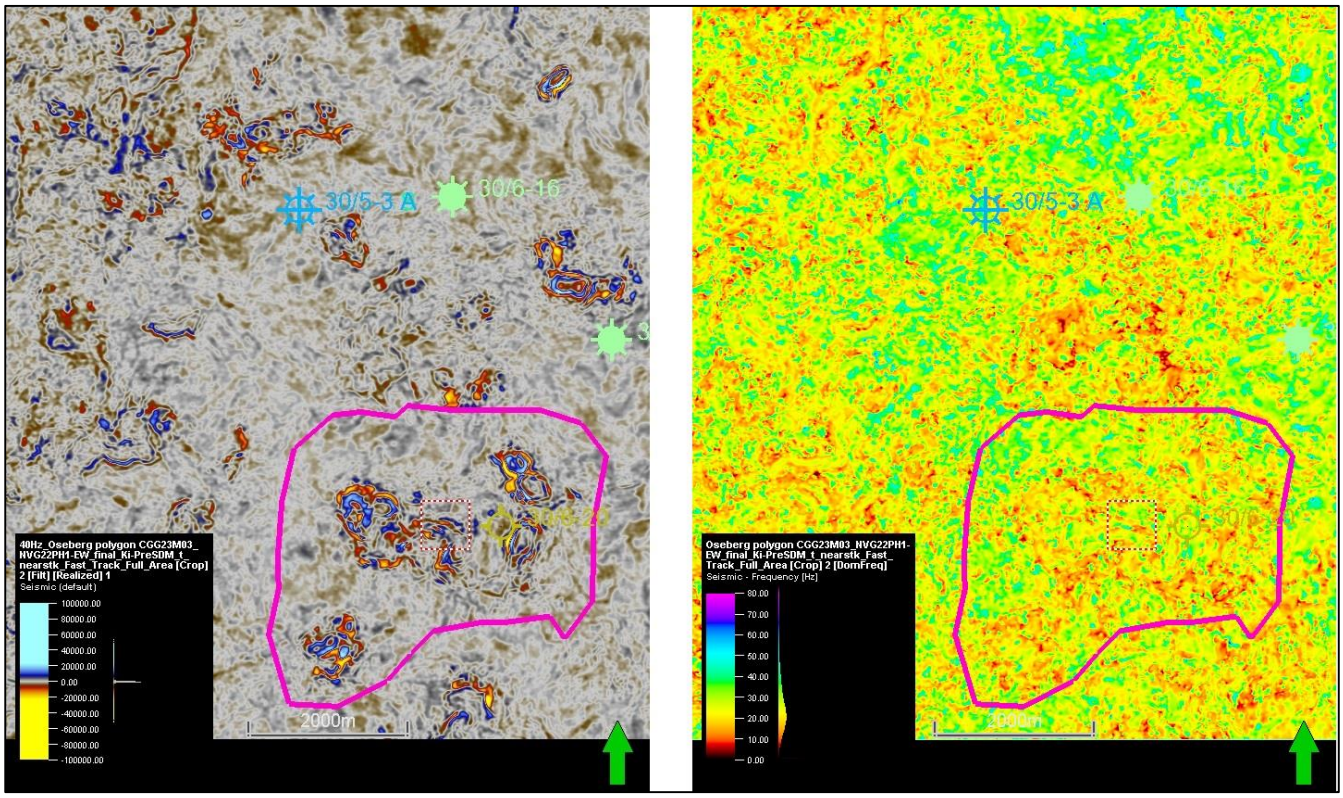

Figure 65: Full stack reflectivity (to the left) and Dominant Frequency attribute with pink polygon highlighting the area of interest.

7.3. Full Waveform Inversion (FWI) velocity model

Preliminary efforts were made to analyze the remobilized sands using the FWI velocity model. The analysis of the FWI velocity model revealed disparities between sands and shales. Shales exhibit velocities ranging from 2175 to 2250 m/s, while sandstones show distinct velocities for cemented and uncemented regions. Cemented sandstone velocities vary from 2300 to 2600 m/s, whereas uncemented sandstone ranges from 2059 to 2150 m/s (Figure 66). Velocity ranges were derived by comparing seismic horizons of uncemented and cemented sands and filtering velocity cube to observe what velocities correspond to given horizons.

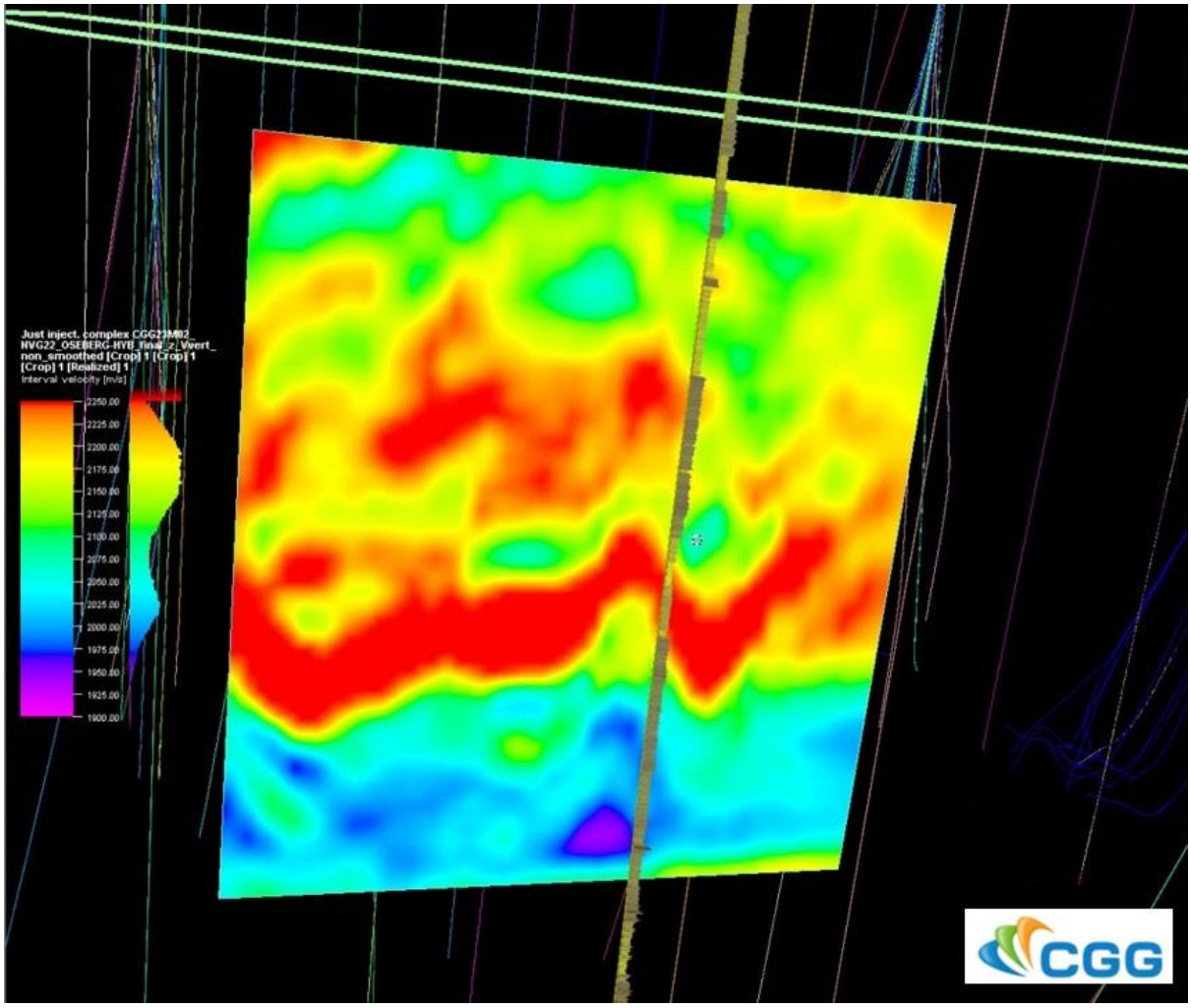

Figure 66: The Full Waveform Inversion (FWI) velocity model displaying variations in velocity within the studied interval. Well 30/6-20 is shown with the GR log.

Based on these differences, geobody extraction by velocity filtering has been carried out, effectively delineating the cemented and uncemented areas within the sand deposits (Figure 67a). However, upon extracting the velocity model values along the well trajectory and comparing them to the more precise V_p well log, it became apparent that while the velocity model generally follows the trend of V_p along the wellbore, it still falls short in resolving detail at the scale of meters (Figure 67b).

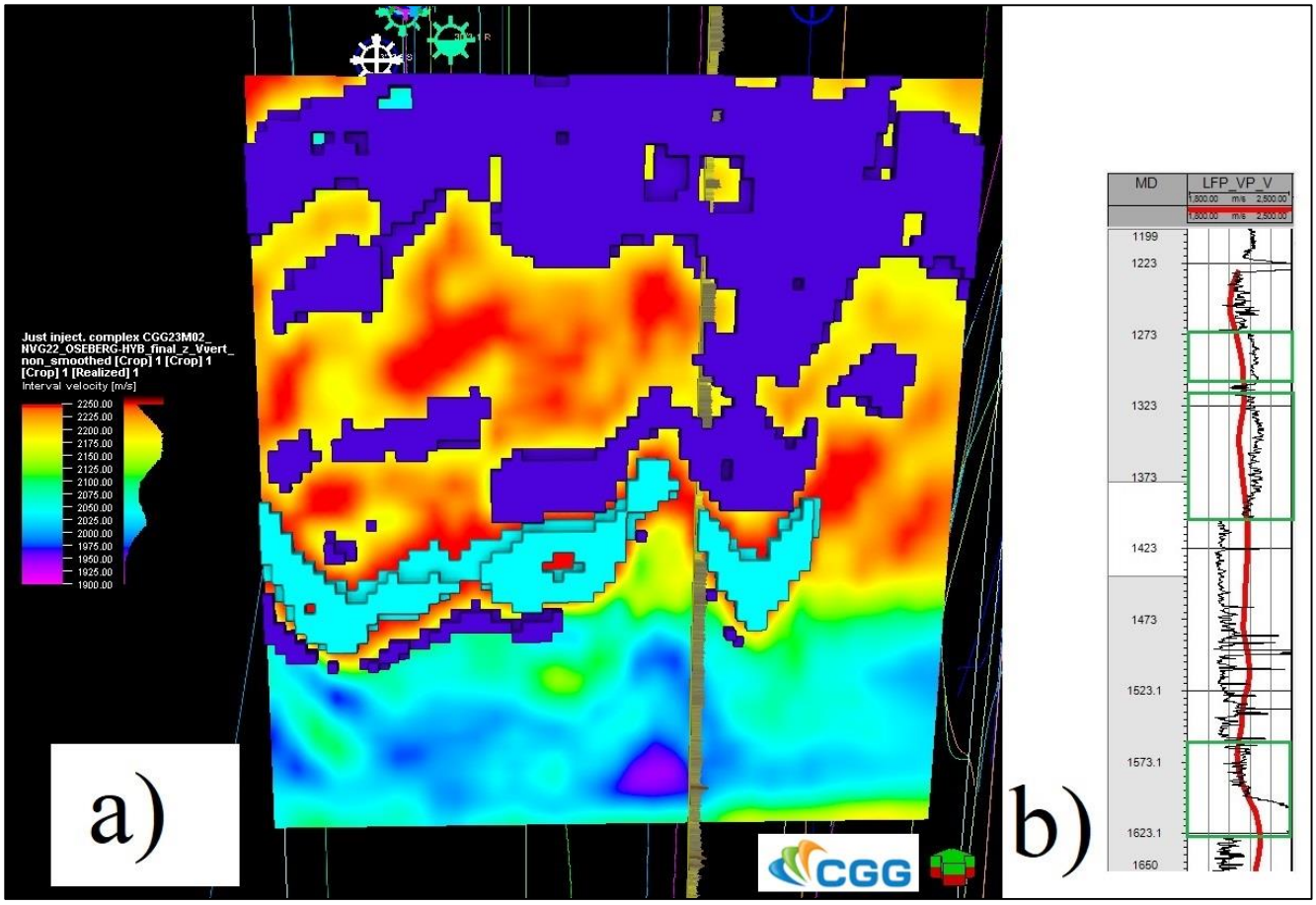

Figure 67: a) Geo bodies extracted based on selectively filtered velocities from the FWI velocity model. The turquoise blocks depict the deeper, cemented wing-shaped sand bodies, while the purple blocks depict the uncemented sands. b) Vp log (black line) in well 30/6-20 and extracted velocity log from the Full Waveform Inversion (FWI) velocity model (red line). Green rectangles highlight remobilized sands.

7.4. AVO

From the initial stages if this research, there were indications that the AVO (Amplitude Versus Offset) technique could be useful in distinguishing between shales and sands since the AVO reflectivity-angle relationship is dependent on Acoustic Impedance (AI) and Poisson's ratio (Chapter 5.1.2). By generating an AI-V_p/V_s plot for the interval under investigation (1170 - 1650 m MD along well 30/6-20), and overlaying a color table representing the shale volume, two distinct curved trends at the top and bottom of the point cloud are evident (Figure 68).

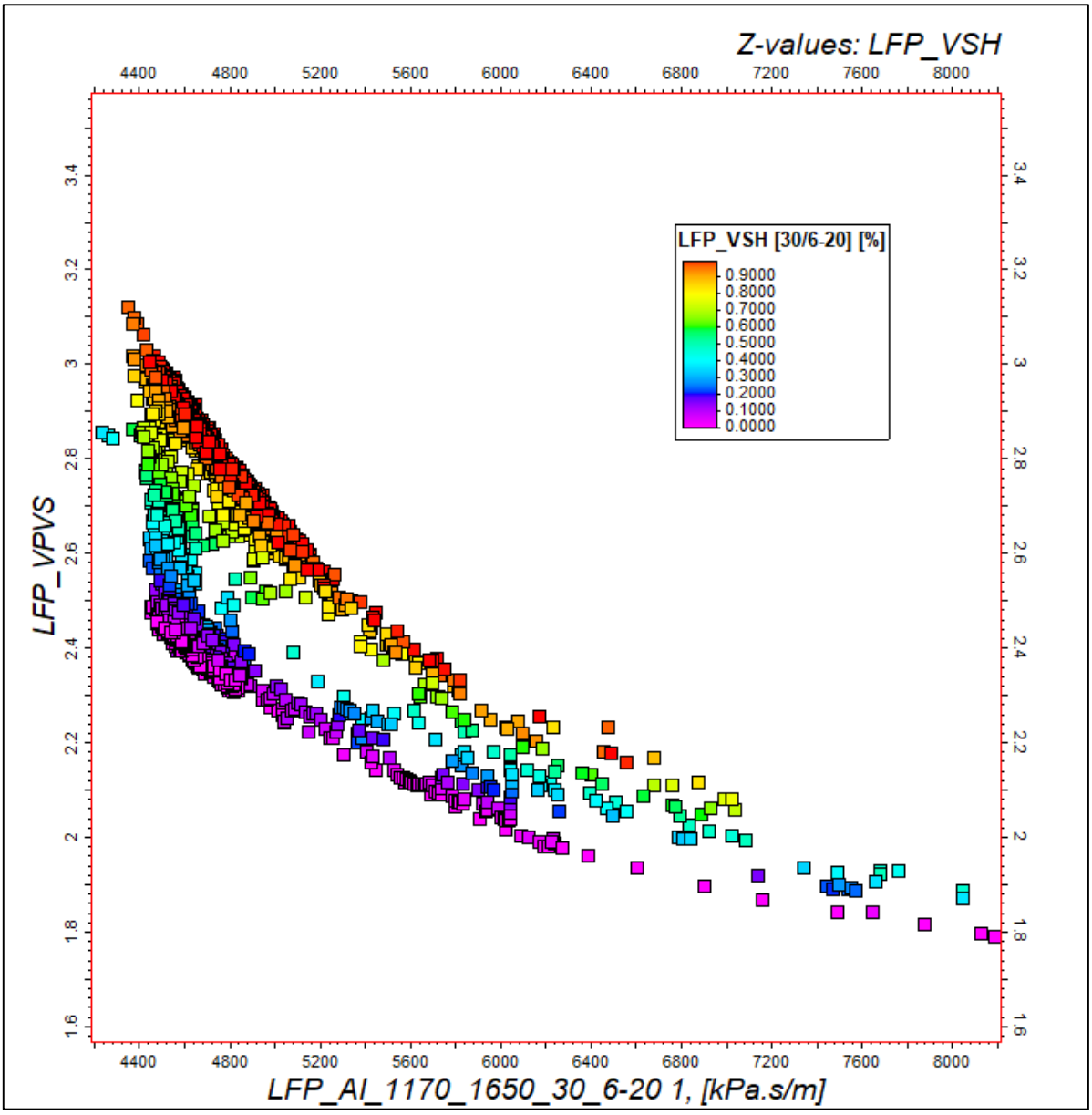

Figure 68: Acoustic Impedance (AI) versus V_p/V_s along well 30/6-20. Data points colored by shale volume. This graph reveals the distinct trends for shales and sands. Sands typically have a lower VSH, whereas shales are characterized by VSH.

Sands, which typically exhibit a low shale volume, correspond to lower V_p/V_s ratios. Conversely, shales, that display higher shale volume, have distinctly higher V_p/V_s values. It is clear that AI alone is insufficient to differentiate between shale and sand. For instance, at around 4400 kPa.s/m, there is a full range of data points with shale volume varying from near 0 to 0.9, illustrating that additional parameters are required for a clear distinction.

Observing previous trend that closely aligns with what is described in the literature (Abbey et al., 2018), Amplitude versus Offset (AVO) modeling was performed manually using Microsoft Excel. The input data for this modeling was derived from well logs, setting an expectation for high-quality outcomes. After computing the Intercept and Gradient for the selected intervals, it was determined that the prevailing AVO class for all top sand layers is Class II or III, depending on the pore content (Figure 69).

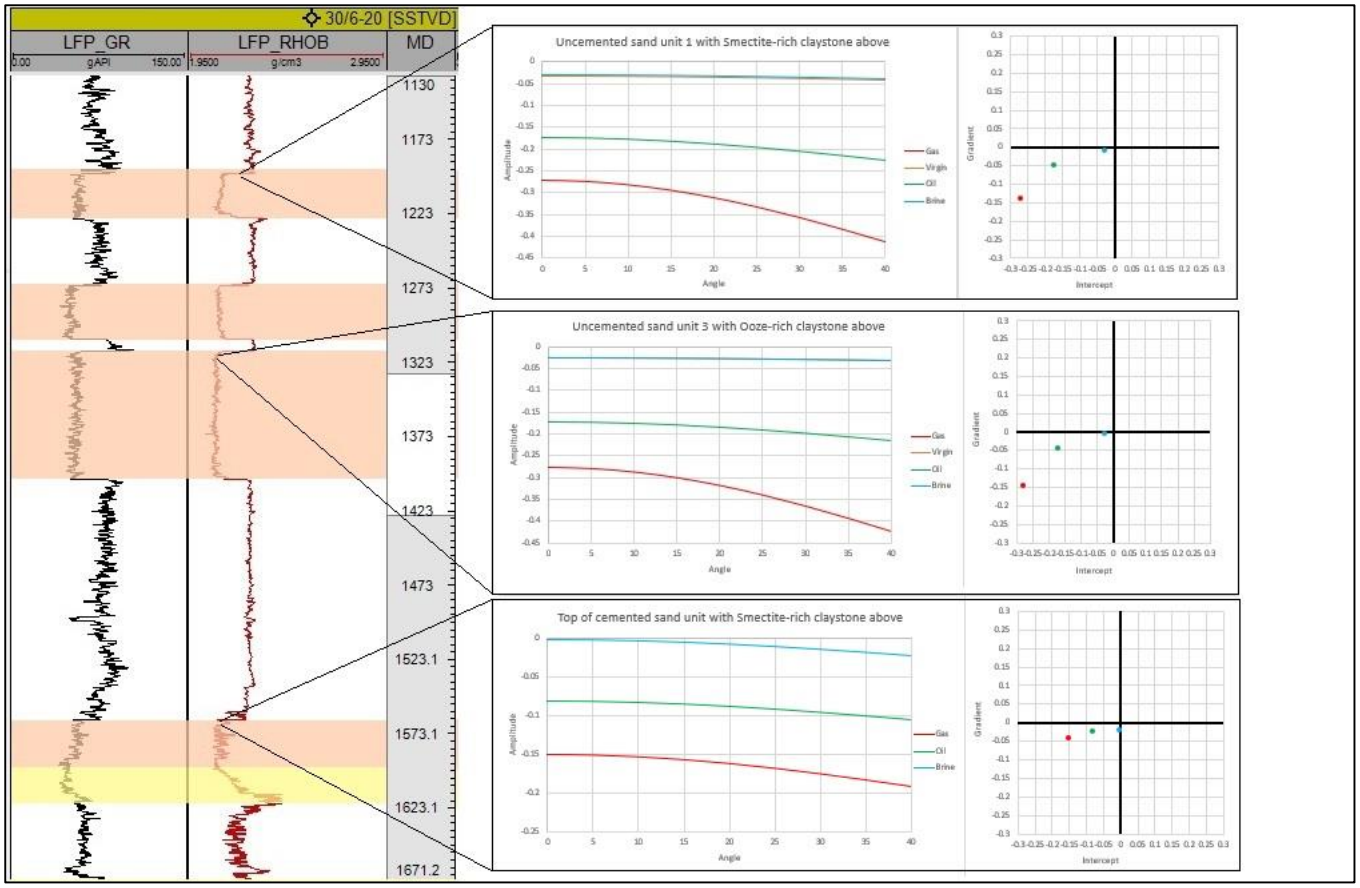

Figure 69: Amplitude-angle and Intercept-Gradient plots for the specified locations along well 30/6-20.

It is important to point out that all the fluid-substituted curves are below the zero-amplitude line. As anticipated, the scenario with gas substitution exhibits the most negative reflectivity at zero-offset (that is, the intercept) as well as the most negative gradient. Moreover, the intermediate location with sand interval capped by ooze-rich claystone exhibits a slightly higher gradient compared to lower and upper intervals with smectite-rich claystone on top. This could be attributed to the skeletal composition of the ooze, which typically possesses high internal porosity and a rigid structure, resulting in lower densities, seismic velocities, and V_p/V_s ratios (Øygarden et al., 2015).

Next, a similar modelling exercise was conducted, but using the AVOCADO module within the Petrel software platform. The resulting Combined AVO class + strength product can be observed in Figure 70. Upon examination of the events that crosscut the strata, which potentially represent remobilized sands, it becomes evident that they exhibit a Class I AVO response, denoted by blue.

Regarding the geometric configurations of the sands, they exhibit an AVO response that is distinctively different from the shale line. This distinction can be explained by the gamma-ray log data along well 30/6-20 (Figure 70), where the blocky gamma-ray signatures of the sands align well with the blue colour indicative of a Class I AVO response. Additionally, the strength parameter shows that the intensely saturated, blue-coloured sands (points that are far from the fluid line), having higher amplitude at the intercept, correspond to areas where high-amplitude, cemented sands were observed in the near stack seismic data.

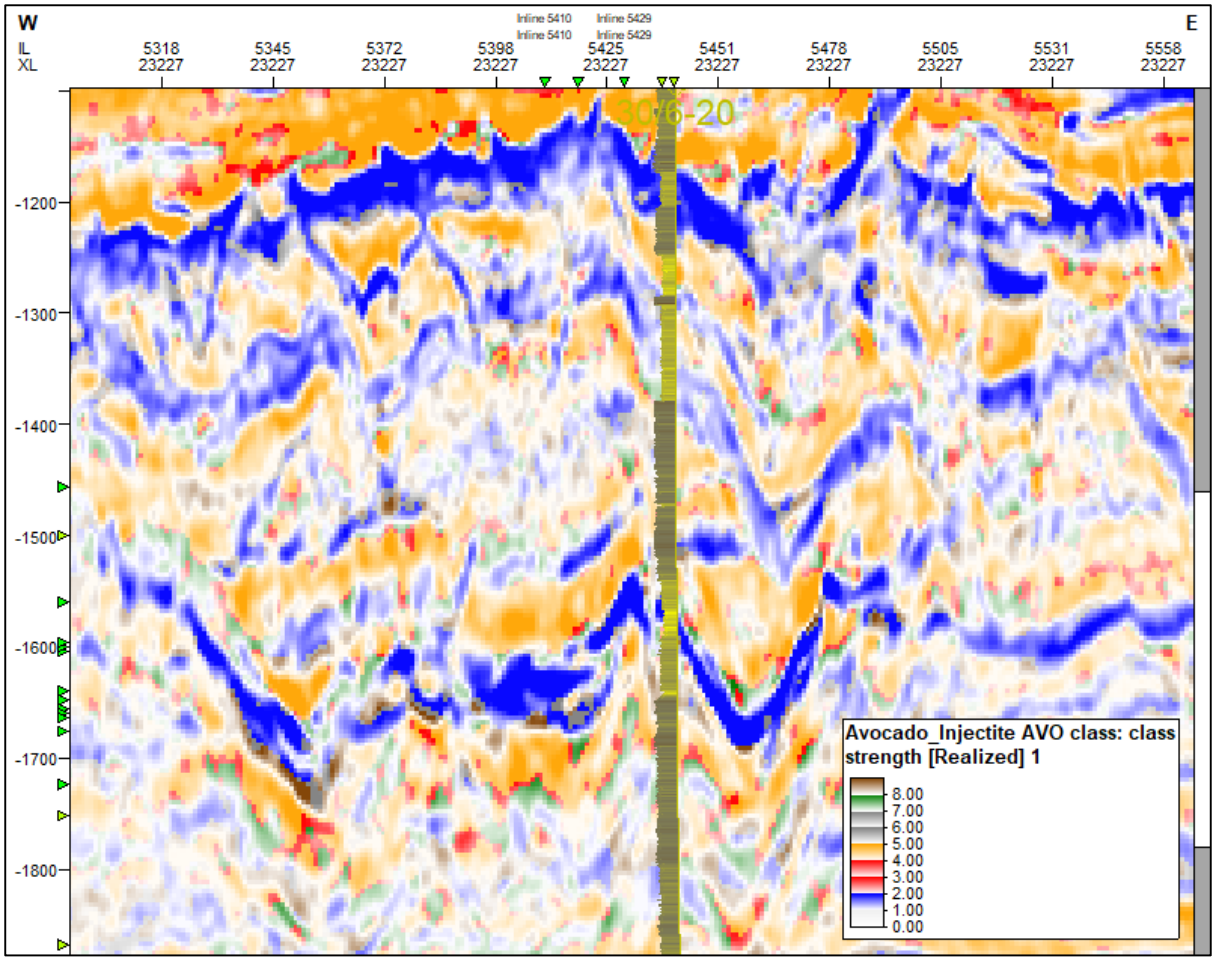

Figure 70: Combined AVO Class + Strength product showing interval of interest and well 30/6-20 with the gamma-ray log.

Yet, significant uncertainty emerges when considering the AVO Class I response indicated by the volume modelled using the software. In contrast, when the modelling was carried out manually using well log data alone, the sand response was categorized as Class II or III depending on the pore content. This discrepancy between the manually computed response and the software-modelled one, which indicates a Class I response, raises questions (Figure 71).

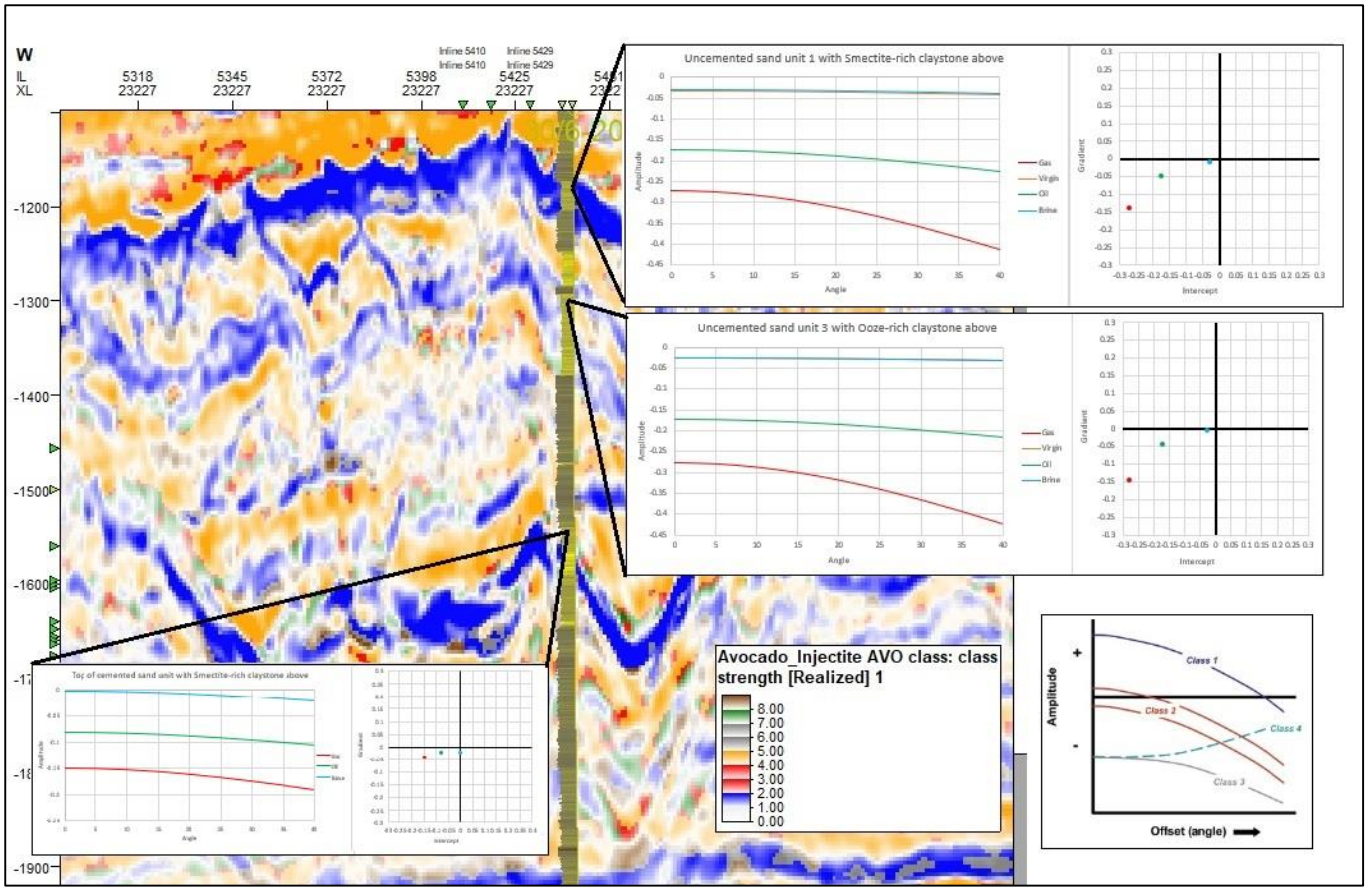

Figure 71: Comparison of Petrel-AVOCADO AVO model and hand-made results. The handmade model suggests an AVO class II, while the software indicates a class I.

7.5. Extended Elastic Impedance

After a thorough exploration to establish the best χ correlations with various parameters, two specific χ angles were identified for their ability to optimally delineate lithological variations ($\chi = -45^{o}$) and fluid changes ($\chi = 15^{o}$).

The lithological volume is distinctly sensitive to changes in lithology and discounts the effects of fluids. This is because the volume is primarily influenced by variations in the velocity of shear waves (V_s), which do not transmit through fluids (Figure 72). Within this volume, sands are hard events as they exhibit strong positive amplitude responses, while background shales manifest as soft negative amplitudes, depicted in blue and yellow respectively.

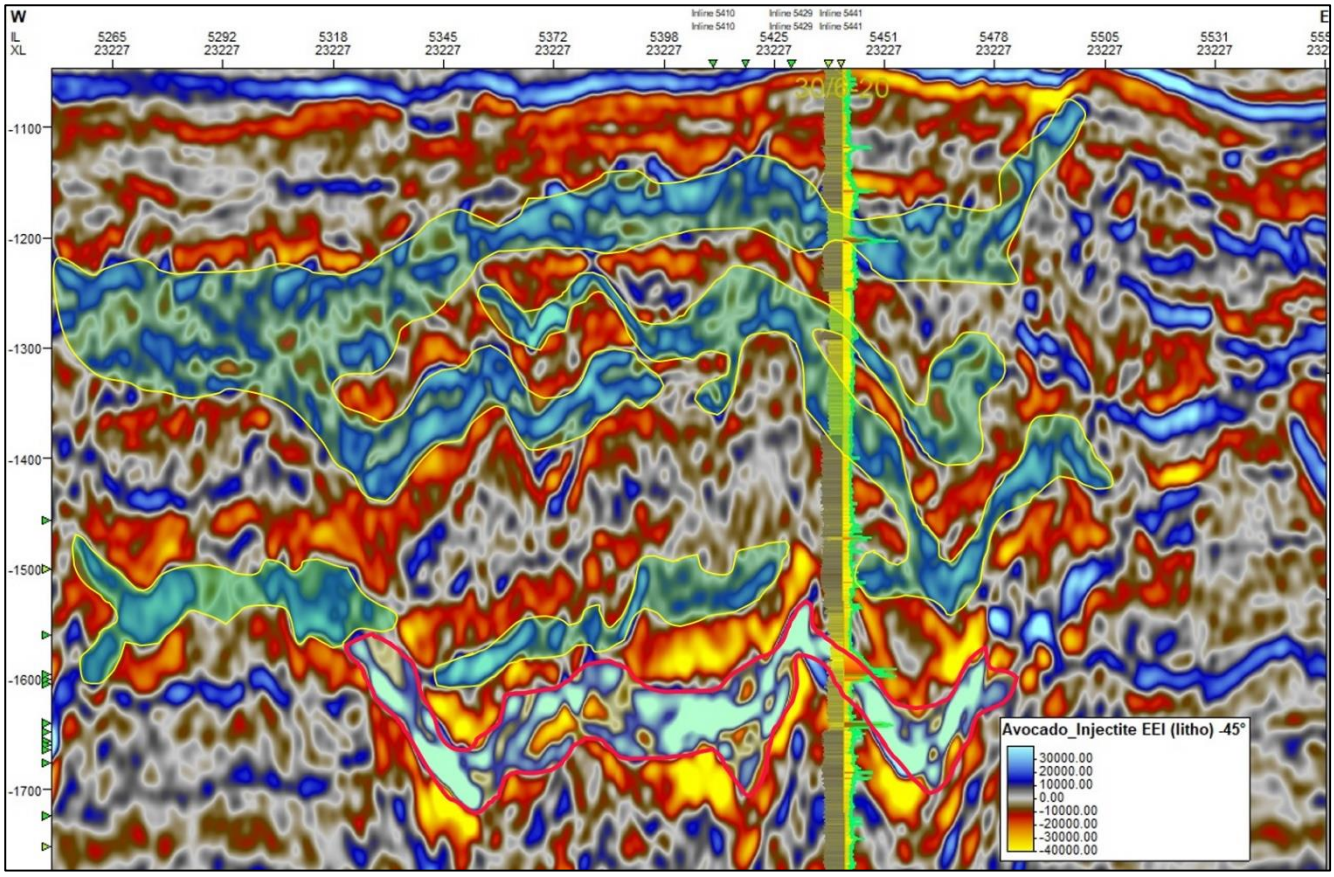

Figure 72: Resultant EEI volume of Shear impedance with highlighted remobilized sands. Red outline – cemented remobilized sands with high amplitude, yellow outline – uncemented remobilized sands. This volume considers only lithological-driven changes in the subsurface. Well 30/6-20 together with gamma-ray (left) log and acoustic impedance (right) are included.

An analysis of Figure 72 reveals that the sands coloured in blue correlate well with the gamma-ray signatures from sands in well 30/6-20, which are also observed in the cross-section. It is noteworthy that maximum positive amplitudes are observed at the base of the sands, indicative of increased acoustic impedance. These high positive amplitudes are associated with carbonate-cemented sands, as previously noticed. This calibration makes the lithology cube a reliable instrument for delineating the boundaries of remobilized sands, even when it is difficult to identify their elusive tops. Specifically, upper intervals of non-cemented sands display marginally weaker amplitudes in comparison to the carbonate-cemented base, and lithological volumes offer a higher level of detail in highlighting certain remobilized sand bodies that are not visible in reflectivity seismic data.

The generated Lambda-Rho volume, which is intended to emphasize fluid effects, did not reveal any fluid-related anomalies in the sand areas (Figure 73). Additionally, completion reports failed to indicate any presence of hydrocarbons within the examined interval. Despite this, the Lambda-Rho volume can be beneficial to compute, particularly when also computing the shear impedance EEI volumes.

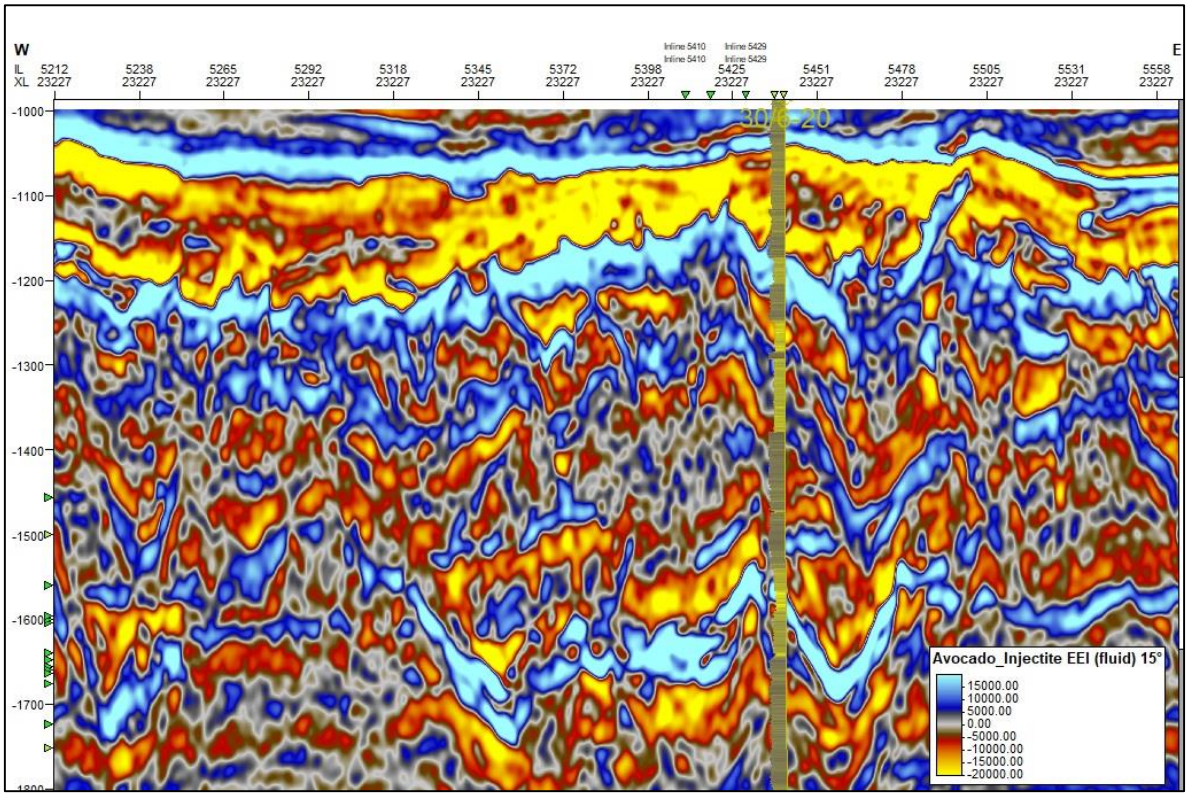

Figure 73: Resultant EEI volume of Lamba-rho. Well 30/6-20 together with gamma-ray log are included. The Bulk Modulus volume considers only fluid-related changes in the subsurface. Fluid-related anomalies in the sand bodies are not observed.

Upon analysing the near-stack, AVO class, and EEI shear (litho) volumes, it becomes evident that the litho volume is most effective in delineating the geometry of the sand injectites (Figure 74). While the near-stack reflectivity seismic data captures the thicker, cemented sands, it struggles to accurately reflect the top sands and displays chaotic responses in regions where the sands appear to be disconnected. The AVO class volume provides a substantially improved image of the sand geometries, revealing some connectivity, and effectively filtering out shale line responses that are prominent in the near-stack data. The EEI shear impedance (litho) volume further refines the imaging from the AVO class volume by better delineating the top uncemented sands and defining the boundaries of the sand bodies. Moreover, the sand bodies in all volumes align closely with the low blocky values of the GR well log (Figure 74).

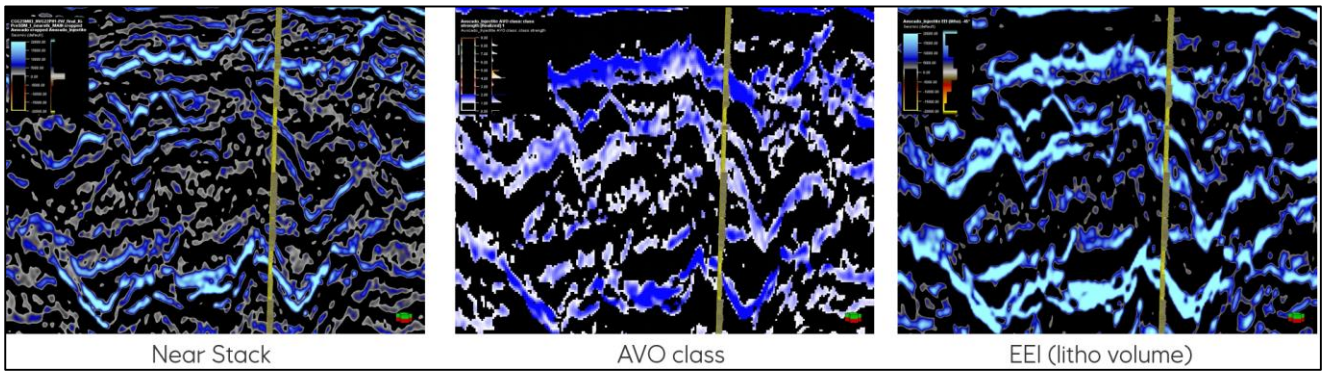

Figure 74: Comparison between the near-stack reflectivity seismic (left), AVO class (middle), and EEI shear/litho (far right) volumes. Only the response from the sands in blue is displayed as the background shales are muted. Calibration well 30/6-20 is displayed with the Gamma Ray (GR) log, which exhibits a strong correlation between the blocky low GR readings and the hard sand responses seen in the volumes.

8. Discussion

This chapter discusses the results in relation to the goals set out by the thesis. The outcomes from the spectral decomposition, AVO, EEI, and FWI velocity models are compared, examined, and discussed within respective sections.

8.1. Well logs and near-stack seismic data

As detailed in section 7.1, utilizing Gamma Ray, bulk density, and P-wave velocity logs alone can facilitate the differentiation of sands from shales (Figure 59). The abrupt changes and blocky responses observed in the well log data may hint at rapid lithological transitions that are challenging to assign solely to depositional environment variations. An important observation from the cuttings photos is the apparent trend of cementation (Figures 60 and 61) — while the bottom section reveals the presence of carbonate cement, the uncemented sands extend from the base to the upper part of the examined depth range (Figures 60 and 61). Moreover, the correlation between higher P-wave velocities and the occurrence of carbonate cement in the images sets the stage for expecting to identify similar features within the reflectivity seismic data (Figures 58 and 59).

By looking at near-stack reflectivity seismic data, positive amplitude events stand out by their high-angled, cross-cutting strata nature (Figure 58). Additionally mentioned earlier differences in cementation effect amplitude as expected by looking at well log readings. Having such observations from the data, it is clear that the observable sands present features of remobilized sands (Chapter 4).

8.2. Spectral Decomposition

Spectral decomposition enhanced the visualization of cemented, wing-shaped sand bodies, providing added clarity at the base of these sand bodies and helping with the mapping of base sands (Figure 63b). Additionally, it successfully reduced the impact of background shale on the display of the sand bodies. However, the method was less effective at detecting thinner sand injectites and the uncemented top sands within the study area. The anticipated 40 Hz blue response, which was hypothesized as tuning thickness to highlight thinner sands, did not appear as a distinct entity. This disagreement could stem from the sub-vertical orientation of the injectites, contrasting with the horizontally oriented features that spectral decomposition typically excels at illuminating. Moreover, the uncemented sand and its boundaries were unrecognized in both the reflectivity data (Figure 58) and spectral decomposition results (Figure 62), likely due to the inherent limits of seismic data. Nonetheless, these findings serve as a base for future mapping efforts, particularly when applied to areas where traditional reflectivity seismic data generates ambiguous responses.

8.3. FWI velocity model

The distinct differences between remobilized sands and shales observed from P-wave velocity well logs (Figure 59) set the expectation that the FWI velocity model could isolate sand injectites as separate geological bodies based on their velocity profiles. Examination of the velocity model (Figure 66) showed markedly different velocities in intervals that corresponded to shale, cemented sands, and uncemented sands as characterized in the well logs. With

identified velocity differences (Table 2), it was possible to distinguish between cemented and uncemented sands, including their structure geometry.

Table 2: Summary table of the extracted velocity values from the Full Waveform Inversion (FWI) velocity model pertaining to uncemented and cemented remobilized sands. The presented values correspond to the cut-offs that were employed in the filtering process for the extraction of geobodies.

Sand Unit	Minimum velocity, m/s	Maximum velocity, m/s
Uncemented sand	2059	2250
Cemented sand	2316	2600

Utilizing these velocity ranges allows for the extraction of geobodies (Figure 67a), which proves advantageous when navigating distinct velocity contrasts. These geobodies enable interpreters to evaluate the volumetrics of remobilized sands, simplifying one aspect of assessing oil reserves in such unconventional structures. Despite these capabilities, the precision of velocity models in spatially delineating remobilized cemented and uncemented sands is still lower than the resolution provided by well data, and there are instances where the model fails to detect the lithological changes that a conventional acoustic log would reveal. Therefore, it cannot be conclusively stated that the velocity-filtering method will hold universally across different geological settings. The success of such a methodology may vary depending on the following factors:

- The resolution of the velocity model, which is influenced by several aspects, including the methodology employed by the service provider, the quality of seismic data acquisition, and other related factors.
- The intrinsic lithological variances within the geological structures, such as the type of cement present, the nature of pore fluids, the volume of shale content, etc.

8.4. AVO Modelling

An initial question in the discussion of AVO modelling arises from the absence of hydrocarbon shows in the well within the studied interval: Why do brine-saturated sand injectites exhibit a notable AVO strength anomaly, distinguish themselves from shales, and why do its intercept/gradient values fall outside the typical shale/fluid line (Figure 70)? Conventionally, brine-saturated sands plot close to the shale or fluid line. The behaviour observed might suggest the presence of a minor percentage of gas within the sand pores, which could be enough to cause a significant AVO response (Figure 23). The findings from this study highlight the importance of conducting spatial exploration of seismic horizons that, despite lacking hydrocarbon shows in wells, may contain localized hydrocarbon accumulations. This is particularly applicable for sand injectites, which are characterized by their intricate geometrical structures with vertical and horizontal connections across various stratigraphic layers, introducing an element of uncertainty with regard to their connectivity.

A major challenge in AVO modelling results is the observed inconsistency between the Class II or III derived from well logs (Figure 71) and the Class I derived from seismic data (Figure 71). The comparison of intercept-gradient cross plots from seismic data modelling (Figure 75a)

and well data modelling (Figure 75b) clearly reveals that the discrepancy between the two arises from their differing intercept values. Whereas the well data suggests a negative intercept, the seismic data indicates a positive intercept. Notably, in both cases, the gradient is consistently negative.

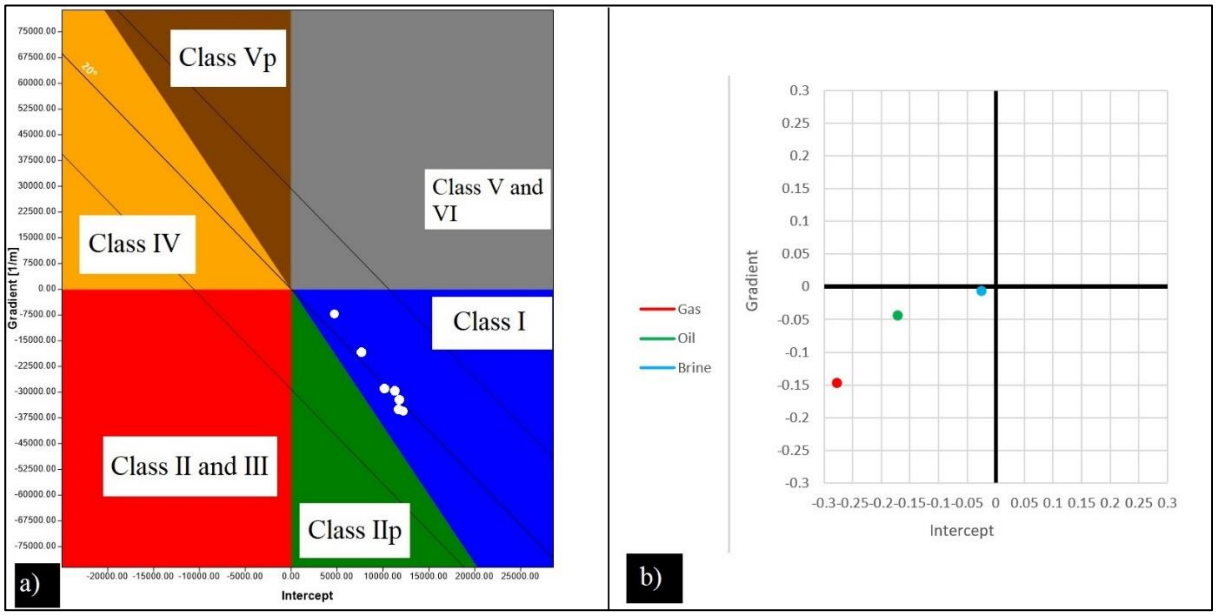

Figure 75: Gradient-Intercept plots for the same interval (uncemented sand unit 3): a) The Gradient-Intercept plot derived from seismic data with its data points in white. The shale line is depicted in black at 20°. b) The Gradient-Intercept plot derived from seismic data, data points are displayed in white. The shale line is depicted in black at 20°. b) The Gradient-Intercept plot derived from well data with its data points. The plots reveal a significant discrepancy in the intercept values of the data points.

There are a few potential explanations for this anomaly:

1. An intercept value close to zero implies that minor deviations caused by dispersion could result in a switch in amplitude—from a slightly negative Class II to a positive Class I response. Such shifts could stem from the data dispersion attributable to the difference between the high-frequency sonic well data (in the thousands of Hz) and the seismic data's comparably lower frequencies (in the tens of Hz).
2. The anisotropy within the sand injectites remains an area for discussion, underscored by a pronounced lack of existing research on this matter. Remobilized sands comprise highly angled structures that also impact the host shales. Such angle changes could profoundly influence variations in physical parameters throughout different locations of the sand injectites, introducing substantial uncertainty in parameter distribution and potentially even affecting seismic measurements.

Despite these inconsistencies between well log-based and seismic-based models, the results continue to robustly differentiate sands from shales. AVO modelling offers an advantage over spectral decomposition and reflectivity seismic data as it delineates uncemented top sands (with a small value in AVO class: class strength), even if accompanied by some level of uncertainty. Consequently, these findings still contribute valuable insights into the potential pore fluid content and help delineate the ranges of uncertainty surrounding the geometry of sand injectites.

8.5. EEI Volume Analysis

As discussed in section 7.4, since shear waves do not propagate through fluids, they are sensitive to changes in the lithology rather than the pore-fluid content. The remarkable alignment between sand identification from well logs and the lithology (shear impedance) volume (Figure 73) suggests that the Extended Elastic Impedance (EEI) technique may be the most effective approach among those tested. This method also adeptly differentiates uncemented top sands from the cemented base of the remobilized sand formations. In comparison with geobody extractions from Full Waveform Inversion (FWI) velocity models, it is evident that EEI, particularly at a χ angle of -45º, delineates the intricate geometries of remobilized sands with superior resolution. This enables the visualization of small-scale sand injectites which are not discernible within the velocity model (Figure 76a).

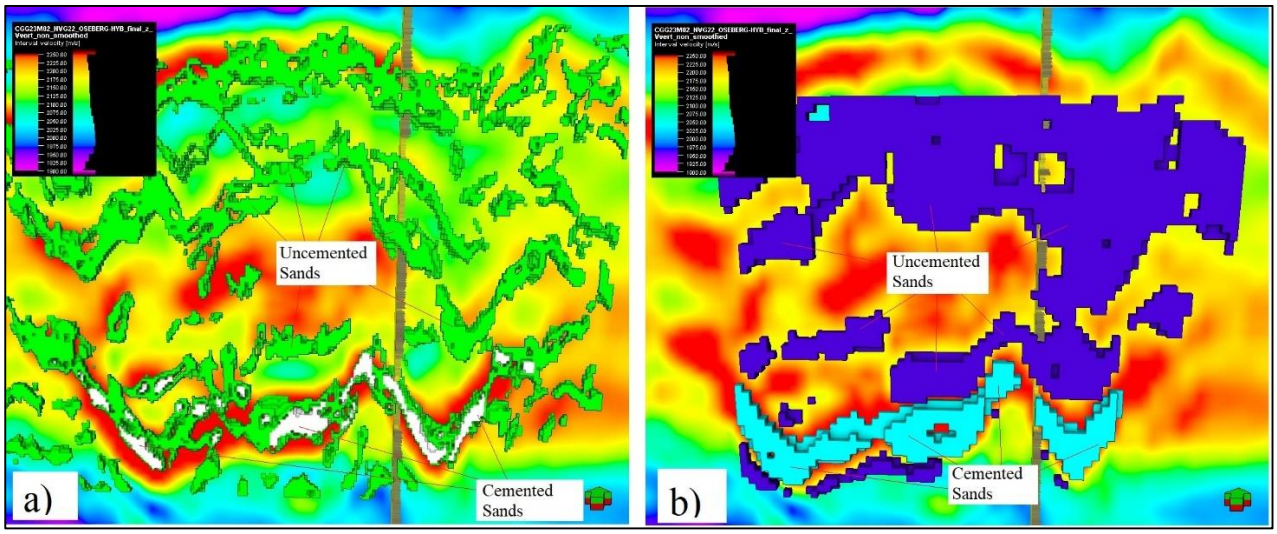

Figure 76: a) Remobilized sands extracted as geobodies from shear impedance volume. FWI velocity is displayed in the background. b) Remobilized sands extracted as geobodies from the FWI velocity model.

In contrast to the FWI velocity model, the EEI technique shows smaller precision when attempting to delineate cemented sands from their uncemented counterparts. Despite this, as demonstrated in Figure 76b, the shear impedance volume captured by EEI provides an impressively detailed mapping of the remobilized sands, including the uncemented tops that were not clear in the reflectivity seismic data. These levels of detail are missing from the velocity model and are not as clearly defined by the spectral decomposition or AVO class strength volume.

9. Conclusion

Drawing on the theoretical framework, methodologies, and findings of this Master thesis, the following conclusions can be drawn:

- Spectral decomposition slightly improves the visualization of cemented, wing-shaped sand bodies; however, it has difficulty in identifying thin sand injectites within the examined area.
- Theoretical modelling (based on well log data) suggests sand injectites should display AVO Class II or III characteristics, yet AVO modelling from seismic data indicates Class I with some level of uncertainty. Despite this inconsistency, AVO volumes remain effective in differentiating shales from sandstones, which are characterized as Class I/II.
- EEI angle analysis indicates that a χ angle of approximately -45º (corresponding to shear impedance) markedly distinguishes shales from sands and effectively highlights uncemented top sands that were not readily apparent in the reflectivity seismic and AVO class volumes.
- Among the techniques employed, EEI at a χ angle of -45º emerges as the most optimal approach for delineating the contours of sand injectites. When used in combination with drill cuttings photo calibrations and analysis of AVO class volumes, EEI proves to be highly effective.

This Master thesis highlights the potential advantages and challenges associated with leveraging Spectral Decomposition, AVO, FWI velocity model, and EEI volumes for mapping sand injectites. Spectral Decomposition effectively emphasizes thicker sands and the cemented bases of remobilized sands, while the FWI velocity model outlines the geometries of sand injectites, though with low accuracy. AVO provides insights into variations in pore fluid content, although it carries a degree of uncertainty. Considering these findings, shear impedance volumes generated through EEI methodologies are a valuable tool, offering significant precision in the mapping of remobilized sands.

9.1. Recommendations for future work

Based on the findings of this Master thesis, the following recommendations are suggested for future research:

Spectral Decomposition:

- Apply generalized spectral decomposition to geologically diverse areas, focusing specifically on horizontally oriented (sills) remobilized sands with variable thicknesses.

AVO:

- Implement the established AVO workflow on an alternative dataset, one where the effects of data dispersion are negligible.

EEI:

- Use the existing EEI workflow in areas characterized by hydrocarbon-charged sand injectites to investigate differential responses at various chi angle projections.

- Explore the potential application of automated Artificial Intelligence (AI) algorithms for the identification and extraction of sand injectites, utilizing labels derived from shear impedance volume data.

References

Aarre, V. (2016, May 10). *EAGE E-Lecture: Understanding Spectral Decomposition*. [Video]. Youtube. https://youtu.be/1nDyMHs8zuw?si=wZ9berS2_cZ1A7vq

Abbey, C. P., Okpogo, E. U., & Atueyi, I. O. (2018). Application of rock physics parameters for lithology and fluid prediction of "TN" field of Niger Delta basin, Nigeria. *Egyptian Journal of Petroleum*, *27*(4), 853–866. https://doi.org/10.1016/j.ejpe.2018.01.001

Anell, I., Thybo, H., & Rasmussen, E. (2011). A synthesis of Cenozoic sedimentation in the North Sea. *Basin Research*, *24*(2), 154–179. https://doi.org/10.1111/j.1365-2117.2011.00517.x

Badley, M. E., Price, J. D., Rambech Dahl, C., & Agdestein, T. (1988). The structural evolution of the northern Viking Graben and its bearing upon extensional modes of basin formation. *Journal of the Geological Society*, *145*(3), 455–472. https://doi.org/10.1144/gsjgs.145.3.0455

Ball, V., Tenorio, L., J.P. Blangy, Thomas, M., & C. Schiott. (2014). Uncertainty Quantification of Two-term Relative Elastic Inversion. *Proceedings*. https://doi.org/10.3997/2214-4609.20147465

Barclay, F., Bruun, A., Rasmussen, K. B., Alfaro, J. C., Cooke, A., Cooke, D., Salter, D., Godfrey, R., Lowden, D., McHugo, S., Ozdemir, H., Pickering, S., Pineda, F. G., Herwanger, J., Volterrani, S., Murineddu, A., Rasmussen, A., & Roberts, R. (2008). Seismic inversion: Reading between the lines. *Oilfield Review*, *20*, 42–63.

Bashir, Y., Numair Ahmed Siddiqui, Daniel Loro Morib, Amir Abbas Babasafari, Syed Haroon Ali, Qazi Sohail Imran, & Karaman, A. (2024). Cohesive approach for determining porosity and P-impedance in carbonate rocks using seismic attributes and inversion analysis. *Journal of Petroleum Exploration and Production Technology*. https://doi.org/10.1007/s13202-024-01767-x

Braccini, E., De Boer, W., Hurst, A., Huuse, M., Vigorito, M., & Templeton, G. (2008). *Sand injectites*. Oilfield Review, 20(2), 34-49.

Bradaric, A. D. (2020, August 25). *Seismic signature and detectability of small-scale sand injectites: insights from 2D Point-Spread Function based convolution modelling*. Bora.uib.no. https://hdl.handle.net/11250/2723787

Cartwright J., James D., Huuse M., Vétel, W., & Hurst, A. (2008). The geometry and emplacement of conical sandstone intrusions. *Journal of Structural Geology*, *30*(7), 854–867. https://doi.org/10.1016/j.jsg.2008.03.012

Cartwright, J. (2010). Regionally extensive emplacement of sandstone intrusions: a brief review. *Basin Research*, *22*(4), 502–516. https://doi.org/10.1111/j.1365-2117.2009.00455.x

Cartwright, J. A. (1994). Episodic basin-wide fluid expulsion from geopressured shale sequences in the North Sea basin. *Geology*, *22*(5), 447. https://doi.org/10.1130/0091-7613(1994)022%3C0447:ebwfef%3E2.3.co;2

Castagna, J. P., Swan, H. W., & Foster, D. J. (1998). Framework for AVO gradient and intercept interpretation. *GEOPHYSICS*, *63*(3), 948–956. https://doi.org/10.1190/1.1444406

Chopra, S., & Marfurt, K. J. (2016). Spectral decomposition and spectral balancing of seismic data. *The Leading Edge*, *35*(2), 176–179. https://doi.org/10.1190/tle35020176.1

Cobain, S., Hodgson, D. M., Peakall, J., & Shiers, M. N. (2017). An integrated model of clastic injectites and basin floor lobe complexes: implications for stratigraphic trap plays. *Basin Research*, *29*(6), 816–835. https://doi.org/10.1111/bre.12229

Connolly, P. (1999). Elastic impedance. *The Leading Edge*, *18*(4), 438–452. https://doi.org/10.1190/1.1438307

Connolly, P. A. (2017). Chi. *Proceedings*. https://doi.org/10.3997/2214-4609.201700825

Davies, R. J., Huuse, M., Hirst, P., Cartwright, J., & Yang, Y. (2006). Giant clastic intrusions primed by silica diagenesis. *Geology*, *34*(11), 917. https://doi.org/10.1130/g22937a.1

Di Felice, R. (2010). Liquid-solid suspension theory with reference to possible applications in geology. *Basin Research*, *22*(4), 591–602. https://doi.org/10.1111/j.1365-2117.2010.00460.x

Dowdell, B. L. (2020). *PySeisTuned2.0*. https://www.pyseistuned.com/

Duranti, D., & Hurst, A. (2004). Fluidization and injection in the deep-water sandstones of the Eocene Alba Formation (UK North Sea). *Sedimentology, 51*(3), 503–529. https://doi.org/10.1111/j.1365-3091.2004.00634.x

Equinor. (2023). *Greater Martin Linge area – Regional overview* . [PowerPoint slides]

Faerseth, R. B., & Ravnås, R. (1998). Evolution of the Oseberg fault-block in context of the northern north sea structural framework. *Marine and Petroleum Geology*, *15*(5), 467–490. https://doi.org/10.1016/s0264-8172(97)00046-9

Frette, L. U. (2018, June 1). *Quantitative seismic interpretation using converted PS waves: A case study from the Oseberg South Field, North Sea*. Uis.brage.unit.no. http://hdl.handle.net/11250/2563011

Gelderblom, P., & Leguijt, J. (2010, October 17). *Geological Constraints In Model-based Seismic Inversion*. OnePetro; OnePetro. https://onepetro.org/SEGAM/proceedings/SEG10/All-SEG10/SEG-2010-2825/96630

Glennie, K. W., & Underhill, J. R. (2009). *Origin, Development and Evolution of Structural Styles*. 42–84. https://doi.org/10.1002/9781444313413.ch2

Goodway, B., Chen, T., & Downton, J. (1997). *Improved AVO fluid detection and lithology discrimination using Lamé petrophysical parameters; "λρ","μρ",&"λ/μ fluid stack", from P and S inversions*. https://doi.org/10.1190/1.1885795

Han, C. (2018). Understanding frequency decomposition colour blends using forward modelling — examples from the Scarborough gas field. *First Break*, *36*(5), 53–60. https://doi.org/10.3997/1365-2397.n0092

Haq, B. U., Hardenbol, J., & Vail, P. R. (1987). Chronology of Fluctuating Sea Levels Since the Triassic. *Science*, *235*(4793), 1156–1167. https://doi.org/10.1126/science.235.4793.1156

Hermanrud C., Christensen, E., M. Haugvaldstad, Røynestad, L. M., Tjensvold, I. T., & L. Watsend. (2019). Triggers of sand remobilization in deep marine deposits. *Special Publication - Geological Society of London/Geological Society, London, Special Publications*, *493*(1), 69–94. https://doi.org/10.1144/sp493-2018-35

Hilterman, F. J. (1989). *Is AVO the seismic signature of rock properties?* https://doi.org/10.1190/1.1889652

Hurst, A., Joseph Albert Cartwright, Mads Huuse, R. Jonk, Schwab, A. M., Davide Duranti, & Cronin, B. T. (2003). *Significance of large-scale sand injectites as long-term fluid conduits: evidence from seismic data*. *3*(4), 263–274. https://doi.org/10.1046/j.1468-8123.2003.00066.x

Hurst, A., Scott, A., & Vigorito, M. (2011). Physical characteristics of sand injectites. *Earth-Science Reviews*, *106*(3-4), 215–246. https://doi.org/10.1016/j.earscirev.2011.02.004

Huuse M., Cartwright, J. A., Gras, R., & Hurst, A. (2005). Kilometre-scale sandstone intrusions in the Eocene of the Outer Moray Firth (UK North Sea): migration paths, reservoirs and potential drilling hazards. *Petroleum Geology Conference Series*, *6*(1), 1577–1594. https://doi.org/10.1144/0061577

Huuse M., Jackson, C., Cartwright, J., & Hurst, A. (2009). *Large-Scale Sand Injectites in the North Sea: Seismic and Event Stratigraphy and Implications for Hydrocarbon Exploration**.

Huuse, M., Cartwright, J., Hurst, A., & Steinsland, N. (2007). Seismic Characterization of Large-scale Sandstone Intrusions. *Archives.datapages.com*, 21–35. https://doi.org/10.1306/1209847M873253

Huuse, M., Jackson, C. A.-L. ., Van Rensbergen, P., Davies, R. J., Flemings, P. B., & Dixon, R. J. (2010). Subsurface sediment remobilization and fluid flow in sedimentary basins: an overview. *Basin Research*, *22*(4), 342–360. https://doi.org/10.1111/j.1365-2117.2010.00488.x

Isaksen, D., & Tonstad, K. (1989). *A revised Cretaceous and Tertiary lithostratigraphic nomenclature for the Norwegian North Sea*. NPD-Bulletin No. 5, 59 Pp.

Jackson, C. A.-L. . (2007). The Geometry, Distribution, and Development of Clastic Injections in Slope Systems: Seismic Examples from the Upper Cretaceous Kyrre Formation, Mly Slope, Norwegian Margin. *Archives.datapages.com*, 37–48. https://doi.org/10.1306/1209848M873254

Jan Inge Faleide, Rune Kyrkjebø, Kjennerud, T., Gabrielsen, R. H., Jordt, H., Stein Fanavoll, & Bjerke, M. D. (2002). Tectonic impact on sedimentary processes during Cenozoic evolution of the northern North Sea and surrounding areas. *Geological Society, London, Special Publications*, *196*(1), 235–269. https://doi.org/10.1144/gsl.sp.2002.196.01.14

Jolly, R. J. H., & Lonergan, L. (2002). Mechanisms and controls on the formation of sand intrusions. *Journal of the Geological Society*, *159*(5), 605–617. https://doi.org/10.1144/0016-764902-025

Jonk, R., Hurst, A., Duranti, D., Parnell, J., Mazzini, A., & Fallick, A. E. (2005). Origin and timing of sand injection, petroleum migration, and diagenesis in Tertiary reservoirs, south Viking Graben, North Sea. *AAPG Bulletin*, *89*(3), 329–357. https://doi.org/10.1306/10260404020

Kausar, T. (2018, June 1). *Simultaneous AVO inversion and seismic lithology cube estimation by using PP and PS angle stack seismic data of the Oseberg Field, North Sea*. Uis.brage.unit.no. http://hdl.handle.net/11250/2563015

Kenneth Samuel, O., & Righteous, O. (2019). Application of Spectral Decomposition and Seismic Attributes For Channel Geometry and Infill Lithology Determination: A Case Study from The Southern North Sea Basin. *International Journal of Earth Science and Geophysics*, *5*(1). https://doi.org/10.35840/2631-5033/1823

Kouidri, H., Aurelien, G., Benaissa, Z., & Berndt, C. (2017). *SUB-SEIMIC SCALE SAND INJECTITES IDENTIFICATION USING 3D SEISMIC FREQUENCY ATTRIBUTES.*

Lee, M. J., & Hwang, Y. J. (1993). Tectonic evolution and structural styles of the East Shetland Basin. *Geological Society, London, Petroleum Geology Conference Series*, *4*(1), 1137–1149. https://doi.org/10.1144/0041137

Lepercq, J.-Y. ., & Gaulier, J.-M. . (1996). Two-stage rifting in the North Viking Graben area (North Sea): inferences from a new three-dimensional subsidence analysis. *Marine and Petroleum Geology*, *13*(2), 129–148. https://doi.org/10.1016/0264-8172(95)00031-3

Li, F., Qi, J., & Marfurt, K. (2015). Attribute mapping of variable-thickness incised valley-fill systems. *The Leading Edge*, *34*(1), 48–52. https://doi.org/10.1190/tle34010048.1

Løseth H, Wensaas L, Arntsen, B., & Hovland, M. (2003). Gas and fluid injection triggering shallow mud mobilization in the Hordaland Group, North Sea. *Special Publication - Geological Society of London/Geological Society, London, Special Publications*, *216*(1), 139–157. https://doi.org/10.1144/gsl.sp.2003.216.01.10

Løseth, H., Raulline, B., & Nygård, A. (2013). Late Cenozoic geological evolution of the northern North Sea: development of a Miocene unconformity reshaped by large-scale Pleistocene sand intrusion. *Journal of the Geological Society*, *170*(1), 133–145. https://doi.org/10.1144/jgs2011-165

Mads Huuse, & Mickelson, M. (2004). *Eocene sandstone intrusions in the Tampen Spur area (Norwegian North Sea Quad 34) imaged by 3D seismic data*. *21*(2), 141–155. https://doi.org/10.1016/j.marpetgeo.2003.11.018

Marfurt, K. J., & Kirlin, R. L. (2001). Narrow-band spectral analysis and thin-bed tuning. *Geophysics*, *66*(4), 1274–1283. https://doi.org/10.1190/1.1487075

Maurya, S. P., Singh, N. P., & Singh, K. H. (2020). Post-stack Seismic Inversion. *Springer Geophysics*, 39–80. https://doi.org/10.1007/978-3-030-45662-7_3

Mondol, N. H., Bjørlykke, K., & Jahren, J. (2008). Experimental compaction of clays: relationship between permeability and petrophysical properties in mudstones. *Petroleum Geoscience*, *14*(4), 319–337. https://doi.org/10.1144/1354-079308-773

Monnier, D., Imbert, P., Régis Mourgues, & Lopez, M. (2014). Pliocene sand injectites from a submarine lobe fringe during hydrocarbon migration and salt diapirism: a seismic example from the Lower Congo Basin. *Geofluids*, *14*(1), 1–19. https://doi.org/10.1111/gfl.12057

Munadi, S., & Purba, H. (2009). Spectral Decomposition Made Simple. *Scientific Contributions Oil and Gas*, *32*(2), 94–102. https://doi.org/10.29017/scog.32.2.92

Norwegian Offshore Directorate. (2024). *Field: MARTIN LINGE - Factpages - Norwegian Offshore Directorate*. Sodir.no. https://factpages.sodir.no/en/field/PageView/All/21675447

Øygarden, B., Løseth, H., & Njerve, S. (2015). Rock properties of smectite- and ooze-rich claystones. *GEOPHYSICS*, *80*(1), D89–D98. https://doi.org/10.1190/geo2013-0363.1

Parize, O., Beaudoin, B., Champanhet, J.-M., Fris, G., Imbert, P., Labourdette, R., Paternoster, B., Rubino, J.-L., & Schneider, F. (2007). A Methodological Approach to Clastic Injectites: From Field Analysis to Seismic Modeling—Examples of the Vocontian Aptian and Albian Injectites (Southeast France). *Archives.datapages.com*, 173–183. https://doi.org/10.1306/1209861M873262

Partyka, G., Gridley, J., & Lopez, J. (1999). Interpretational applications of spectral decomposition in reservoir characterization. *The Leading Edge*, *18*(3), 353–360. https://doi.org/10.1190/1.1438295

Pernin N, Feuilleaubois L, Bird, T., & Reiser, C. (2019). Identifying and de-risking near-field opportunities through reliable pre-stack broadband attributes: examples from the Paleocene North Sea (UK–Norway) injectites play. *Special Publication - Geological Society of London/Geological Society, London, Special Publications*, *494*(1), 445–459. https://doi.org/10.1144/sp494-2019-11

Pranata, G. D., Rosid, M. S., & Martian, D. (2017). Optimization of distribution and characterization of sand reservoir by using extended elastic impedance method in “G” old field. *AIP Conference Proceedings*. https://doi.org/10.1063/1.4991294

Ravnås, R., Nøttvedt, A., Steel, R. J., & Windelstad, J. (2000). Syn-rift sedimentary architectures in the Northern North Sea. *Geological Society, London, Special Publications*, *167*(1), 133–177. https://doi.org/10.1144/gsl.sp.2000.167.01.07

Resnick, J. R., Lerche, I., & Shuey, R. T. (1986). *Reflection, transmission, and the generalized primary wave*. *87*(2), 349–377. https://doi.org/10.1111/j.1365-246x.1986.tb06628.x

Rutherford, S. T., & Williams, R. W. (1989). *Amplitude-versus-offset variations in gas sands*. *54*(6), 680–688. https://doi.org/10.1190/1.1442696

Schroeder, F. (2017, September 28). *Amplitude vs Offset* . [Video]. Youtube. https://www.youtube.com/watch?v=4UcNdF5LWoU&t=406s

Sheriff, R. E., & Geldart, L. P. (1995). *Exploration Seismology*. Cambridge University Press.

Shevchenko, S. (2023). *Monitoring Pressure and Saturation Changes in a Clastic Reservoir from Time-lapse Seismic Data Using the Extended Elastic Impedance Method*. Espace.curtin.edu.au. https://espace.curtin.edu.au/handle/20.500.11937/93573

Shuey, R. T. (1985). A simplification of the Zoeppritz equations. *GEOPHYSICS*, *50*(4), 609–614. https://doi.org/10.1190/1.1441936

Slawinski, M. A., Slawinski, R. A., Brown, R. J., & Parkin, J. M. (2000). A generalized form of Snell’s law in anisotropic media. *GEOPHYSICS*, *65*(2), 632–637. https://doi.org/10.1190/1.1444759

Śliwińska, K. K., Thomsen, E., Schouten, S., Schoon, P. L., & Heilmann-Clausen, C. (2019). Climate- and gateway-driven cooling of Late Eocene to earliest Oligocene sea surface temperatures in the North Sea Basin. *Scientific Reports*, *9*(1). https://doi.org/10.1038/s41598-019-41013-7

Smith, G. C., & Gidlow, P. M. (1987). Weighted stacking for rock property estimation and detection of gas*. *Geophysical Prospecting*, *35*(9), 993–1014. https://doi.org/10.1111/j.1365-2478.1987.tb00856.x

Stewart, R. R., Gaiser, J. E., Brown, R. J., & Lawton, D. C. (2003). Converted-wave seismic exploration: Applications. *GEOPHYSICS*, *68*(1), 40–57. https://doi.org/10.1190/1.1543193

Swarbrick, R. E., & Osborne, M. J. (1998). Memoir 70, Chapter 2: Mechanisms that Generate Abnormal Pressures: an Overview. *Archives.datapages.com*, 13–34. https://archives.datapages.com/data/specpubs/memoir70/m70ch02/m70ch02.htm

Trede, C. (2019, June 15). *3D seismic analysis of the Basement to Early Cretaceous in the Selje High, Sløre*botn Sub-basin and Måløy Slope, southern Norwegian Sea.* Uis.brage.unit.no. http://hdl.handle.net/11250/2619661

Whitcombe, D. N., Connolly, P. A., Reagan, R. L., & Redshaw, T. C. (2002). Extended elastic impedance for fluid and lithology prediction. *GEOPHYSICS*, *67*(1), 63–67. https://doi.org/10.1190/1.1451337

Widess, M. B. (1973). *HOW THIN IS A THIN BED? 38*(6), 1176–1180. https://doi.org/10.1190/1.1440403

Wild, J., & Briedis, N. (2010). Structural and stratigraphic relationships of the Palaeocene mounds of the Utsira High. *Basin Research*, *22*(4), 533–547. https://doi.org/10.1111/j.1365-2117.2010.00479.x

Ziegler, P. A. (1990). *Geological atlas of Western and Central Europe*. Shell Internationale Petroleum Maatschappij B.V. ; Bath, Eng.

Zoeppritz, K. (1919). VII b. Über Reflexion und Durchgang seismischer Wellen durch Unstetigkeitsflächen. *Nachrichten von Der Gesellschaft Der Wissenschaften Zu Göttingen, Mathematisch-Physikalische Klasse*, *1919*, 66–84. http://dml.mathdoc.fr/item/GDZPPN002505290/